NC-AFM studies on CeO_2 film and CeO_2 crystal surfaces

Dissertation

zur Erlangung des Doktorgrades (Dr. rer. nat.)
am Fachbereich Physik
der Universität Osnabrück
vorgelegt von

Reinhard Olbrich

Osnabrück, Oktober 2017

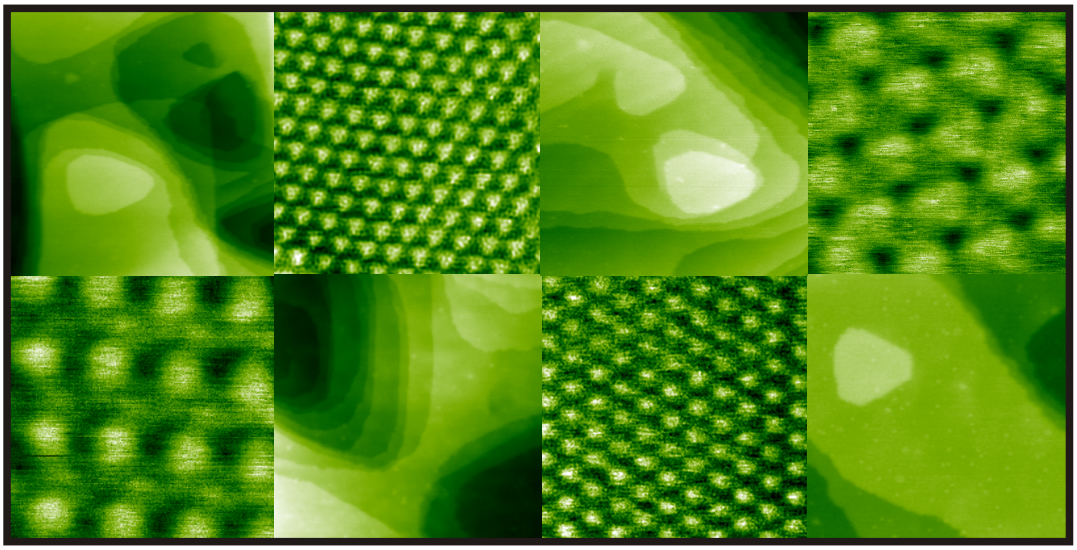

Gutachter der Dissertation:
Prof. Dr. M. Reichling
Dr. C. Barth

Contents

1 Introduction

Cerium dioxide (ceria, CeO_2) has become one of the most important materials in catalytic applications over the last three decades and is used in several technologies and devices [1–3]. Ceria is used as both as a catalytic support and as an active catalytic material [4, 5]. Cerium oxide is well known for its large oxygen storage (OSC) [6] and release capacity which is a result of the reduction and oxidation of cerium ions which lead to a transformation of ceria from CeO_2 to Ce_2O_3 and vice versa. Ceria is of substantial importance for the conversion of acid gases in catalytic processes and is used in the water-gas shift reaction and hydrocarbon oxidation [7–10]. The most prominent examples are three way catalytic converters for CO oxidation and NO_x reduction developed for the automotive industry [11]. While in the beginning pure ceria was used in catalytic converters nowadays mixed oxides based on CeO_2/ZrO_2 are preferred due to an even higher OSC [8, 12]. Additionally, ceria based materials are used for fuel oxide cells [13], in storage devices based on resistive switching [14] and in biological applications [15].

In this wide field of applications, thermodynamic and chemical processes are influenced by the structure of the ceria surface [3]. For example oxygen vacancies are involved in the conversion of acid gases in catalytic processes [16] and it is assumed that the formation of oxygen vacancies is crucial for catalytic capabilities [17]. Therefore, obtaining a detailed knowledge of the surface structure is a key element for understanding and controlling fundamental processes.

In this work, different ceria samples namely in form of a thin film or single crystal are studied with surface sensitive methods. Therefore, we observe the ceria samples with atomic force microscopy (AFM) operated in the non-contact mode (NC-AFM) to obtain topographic information of the surface morphology and atomic structure as well as all kind of defects like oxygen vacancies and Kelvin probe force microscopy (KPFM) to gain information on the electric surface potential. With cooperative partners also X-ray photoelectron spectroscopy (XPS) measurements, Low-energy electron diffraction (LEED) measurements and density functional theory calculations (DFT) are conducted. LEED measurements are carried out by the Group of Prof. J. Wollschläger (University of Osnabrück, Germany) to proof observed phase transition in the morphology of the ceria film [18]. XPS and some AFM measurements are carried out by groups of Dr. Ph. Parent and Dr. C. Laffon (XPS) and Dr. C. Barth (AFM) in Marseille (CINaM, Aix-Marseille University/CNRS, France). In particular the influence of reducing conditions to the ceria surface due to annealing under ultra-high vacuum conditions (UHV) is observed and compared to annealing in ambient and oxygen atmosphere conditions [19]. Intensive density functional theory calculations (DFT) and statistical thermodynamics are performed by groups of Dr. Ganduglia-Pirovano (Instituto de Catálisis y Petroleoquímica, Spain) and

Dr. Gustavo E. Murgida (Departamento de Física de la Materia Condensada, Argentina) to explain surface reconstructions imaged with NC-AFM [20].

The background of the experimental methods are discussed in chapter 2. Here the basic principles of NC-AFM and KPFM are explained. In chapter 3, a brief description of the used NC-AFM system is given and some modifications and optimizations of the set-up that emerged from this work are presented with a detailed measurement and discussion of the noise floor in the NC-AFM system. In chapter 4 basic surface properties of cerium oxide are described and the ceria samples used in this work a presented in detail.

In chapter 5.2 results are presented in form of per reviewed papers that were previously published, other results are original and not yet published. In section 5.2.1, the surface morphology of the ceria films is discussed depending on the annealing temperature under reducing UHV conditions. These results are compared to results for annealing under ambient conditions and annealing in a controlled oxygen atmosphere in 5.2.2. In section 5.2.3, common line defects typically found on ceria film and crystal surfaces are presented and discussed. One of the most interesting findings in this work are surface reconstructions arising from reduction due to UHV annealing and represent special ceria phases. Some previously never reported phases are observed by direct imaging in section 5.2.4 accompanied with results of DFT studies providing to a full picture of the ceria surface phase diagram.

Further measurements showing an unusualy high coverage of the ceria film surface with water/hydroxyl species under UHV conditions are discussed on the basis of atomic resolution NC-AFM images in section 5.2.5. The evaluation of the results is concluded with a comparative analysis of the differences in the morphology of the films and two different crystals in section 5.2.6.

2 Atomic Force Microscopy

In this chapter a brief description of the historical and technical background of the non-contact atomic force microscopy (NC-AFM) is given.

2.1 Historical background

In modern surface science, the direct imaging of atomic interactions in form of a visible image with topographic contrast is one of the most impressive possibilities. The most prominent pioneers in the field are Binnig and Rohrer who invented the scanning tunneling microscopy (STM) technique in the early 1980s [21–25] and who got awarded with the Nobel Price in physics in 1986 [26]. The invention of the STM was the breakthrough for the emerging field of Nanoscience.
The STM is based on the effect of quantum tunnelling whereby a small tunneling current between a tip and a conductive surface can be measured for tip surface distances in the atomic range. Already during the first measurements with the STM, an additional interaction between a very near approached probe and a surface was recognized which were interpreted as a effect of acting atomic forces. This observation consequently lead to the invention of atomic force microscopy (AFM) and the first experimental set up of an AFM by Binning, Quate and Gerber in 1986 [27, 28]. The AFM technique is based on different inter-atomic forces and, in contrast to the STM, it allows studying of insulating surfaces where a tunneling current normally cannot be measured, because of the band gap of insulators. The NC-AFM technique was subsequently improved and the first true atomic resolution was obtained on a Si(111) (7×7) surface in 1995 [29]. The first time defects were observed on insulating surfaces was in 1997 on NaCl [30]. In the following years, several further brake throughs in the direct imaging of insulating surfaces on atomic scale were achieved [28, 31–34]. New sensors like the quartz tuning fork force sensor operating with very small tip oscillation amplitudes where invented [35, 36] and new fields like the imaging of complete force maps and the deliberate functionalization of scanning probes were established allowing the observation of the chemical structure of molecules [37–40]. To further optimise the technique noise sources in NC-AFM experiments were thoroughly studied and result in greatly enhanced performance of modern NC-AFM systems [41]. The noise reduction in NC-AFM systems also opened the door for the nowadays well established field of NC-AFM in liquids [42].

2.2 Basics of Non- Contact Atomic Force Microscopy

The following description is based on fundamental literature that deals with the basic principles of AFM and NC-AFM [28, 32, 43–46].
The concept of NC-AFM relies on the measurement of forces between a surface and a probe that is approached to the surface at a distance where the probe can measurably interact with the surface. In a NC-AFM setup, the probe is usually attached to a cantilever excited at its resonance frequency f_{res} that is close to the eigenfrequency $f_0 = w_0 \cdot 2\pi$. An approximative model for the description of the cantilever oscillation far away from a surface is a damped harmonic oscillator driven by an external source. In this case the tip sample interaction resulting in a force F_{ts} can be neglected. The equation of motion for such an oscillator is given by:

$$\ddot{x} + \gamma\dot{x} + w_0^2 x = w_0^2 x_d \tag{2.1}$$

where γ is the damping constant, x_d an external driving movement of the form $x_d = A_d cos(wt)$ and $w_o = \sqrt{k/m}$ with k being the spring constant (cantilever stiffness) and m the mass (for a real cantilever the effective mass m*). The solution of this second order differential equation is given by:

$$x(t) = A\cos(wt + \phi) \tag{2.2}$$

where A is the amplitude and ϕ a phase shift between the oscillation and excitation amplitude. The amplitude A is given by:

$$A = \sqrt{\frac{A_d^2}{\left(1 - \frac{w^2}{w_0^2}\right)^2 + \frac{w^2}{Q^2 w_0^2}}} \tag{2.3}$$

where $Q = w_o/\gamma$ is the quality factor and w/w_0 is the normalized frequency. The phase ϕ can be expressed as:

$$\phi = \arctan\left(\frac{-\frac{w}{w_0}}{Q\left(1 - \left(\frac{w}{w_0}\right)^2\right)}\right) \tag{2.4}$$

In figure 2.1 amplitude and phase are shown as a function of the normalized driving frequency w/w_0 for three different quality factors. The plot reveals that the resonance curve for the amplitude gets narrower for higher quality factors. At resonance, the phase is at -90° and reaches 0° for frequencies below the resonance frequency and -180° for frequency higher than the resonance frequency. For higher Q values the phase shift is more located at the resonance frequency. From equation 2.3 it can be derived that in case of an excitation at the resonance frequency the amplitude is $A(f_0) = QA_d$ and therefore the amplitude is always Q times higher than the excitation amplitude. Cantilevers which are used in this work have a resonance frequency in the range of 300 kHz and quality factors of 15000-45000 under ultra-high vacuum conditions. A careful look at equation 2.3

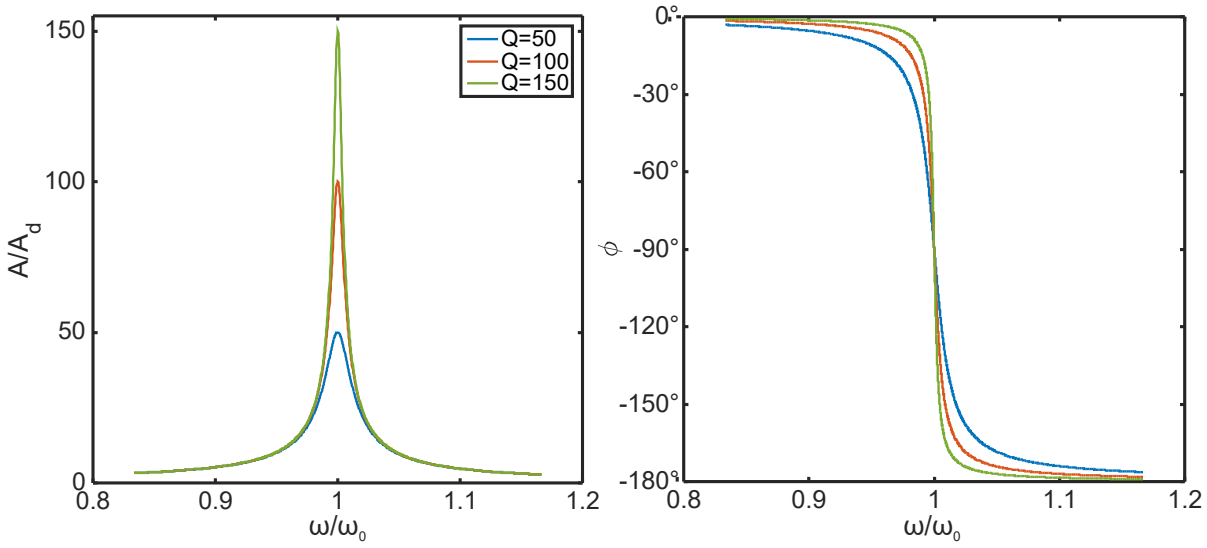

Fig. 2.1: Amplitude and phase response of the damped harmonic oscillator as function of the normalized frequency.

reveals that the maximum amplitude is achieved when the denominator has its minimum. This is derived in equation 2.5 where the shift from the resonance frequency is calculated. The maximum amplitude is achieved for an excitation frequency slightly lower than the resonance frequency. In practice this shift is not relevant as for a real cantilever(Q=27000, f_0=330 kHz) the shift is only $\delta w = 0.113\,\mathrm{mHz}$.

$$\begin{aligned}
\frac{d}{dw}\left(\left(1-\frac{w^2}{w_0^2}\right)^2+\frac{w^2}{Q^2w_0^2}\right)&=0\\
2\left(1-\frac{w^2}{w_0^2}\right)\left(\frac{-2w}{w_0^2}\right)+\frac{2w}{Q^2w_0^2}&=0\\
-4w\left(\frac{1}{w_0^2}-\frac{w^2}{w_0^4}-\frac{1}{2Q^2w_0^2}\right)&=0\\
w_0\sqrt{1-\frac{1}{2Q^2}}&=w\\
\Rightarrow \delta w = w_0 - w &= w_0\left(1-\sqrt{1-\frac{1}{2Q^2}}\right)
\end{aligned} \tag{2.5}$$

The solution of the driven harmonic oscillator with damping is only valid in the limit of a long time elapsed since the start of driving the cantilever.

Without the external driving movement the damping of the cantilever results in a decrease of the amplitude. The damping of a real cantilever in UHV is relative low, only the solution for the underdamped case has to be considered which is given by:

$$x(t) = A_0 \cdot e^{\frac{-\gamma}{2}t}\cos(wt-\phi) = A_0 \cdot e^{-\frac{w_0}{2Q}t}\cos(wt-\phi) \tag{2.6}$$

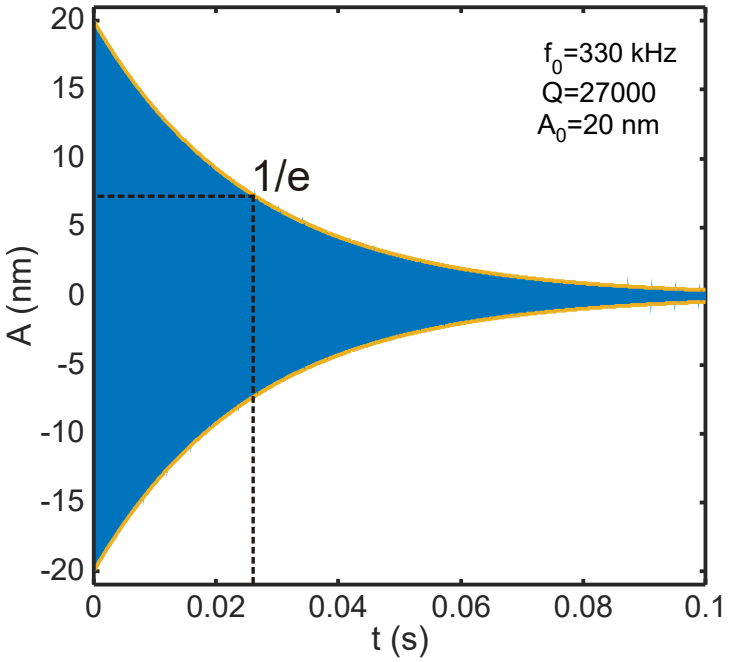

Fig. 2.2: Oscillation amplitude as function of time for the damped oscillator after switching of the driving force at t=0s. The plot shows a fast decrease of the amplitude, so that for a larger time only equation 2.2 must be considered. The characteristic point where the amplitude is decreased to $1/e$ is marked in the figure.

The transient oscillation can be described as a superposition of equation 2.2 and 2.6.

In figure 2.2 the amplitude decay according to equation 2.6 is shown as function of the elapsed time t using parameters of a real cantilever in UHV. The amplitude decreases very fast and the oscillation is decayed already for a time > 0.1s.
A characteristic point is the time τ in which the amplitude A decreases to the value $A \cdot 1/e$, where the parameters τ and Q are related by:

$$Q = \pi f_0 \tau \tag{2.7}$$

The time τ is called the ring down time. In practice the oscillation amplitude is measured with an oscilloscope and the excitation of the cantilever is suddenly interrupted. This leads to a measured oscillation like the one shown in figure 2.2.

An alternative definition of the quality factor Q is:

$$Q = 2\pi \cdot \frac{\text{Energy stored in oscillation}}{\text{Energy dissipated per cycle}} = 2\pi \cdot \frac{\frac{1}{2} m w_0^2 A^2}{\pi \gamma m w_0 A^2} = \frac{w_0}{\gamma} \tag{2.8}$$

Practically, the quality factor can also be determined from the amplitude response when driving the oscillator at its eigenfrequency:

$$Q \approx \frac{f_0}{\Delta f_{\mathrm{FWHM}}} \tag{2.9}$$

where Δf_{FWHM} is the full width at half maximum that can be determined from resonance curves like the one shown in figure 2.1. The definitions 2.8 and 2.9 lead to equivalent results only for a low damping resulting in high quality factors [47] which is the case for our used sensors in UHV.

2.3 Frequency shift and fundamental forces in NC-AFM

In the previous section, the cantilever was approximated as a driven damped harmonic oscillator and some fundamental definitions were introduced.
Here we look at the NC-AFM operation in the frequency modulated (FM) mode. When the cantilever is approached close to a surface the interaction between the probe and surface lead to an external force subjected to the cantilever resulting in a measurable shift of the resonance frequency f_{res}. This frequency shift $\Delta f = f_{res} - f_0$ is the main signal used in NC-AFM. In the FM-mode the oscillation amplitude is always kept at a constant value and an independent PI-feedback loop controls the position z between probe and surface in such manner that Δf is kept at a pre-defined set-point. The position z corresponds to the cantilever piezo element position and is recorded as the topography signal.
To find an expression for the frequency shift it has to be considered that the acting force on the cantilever is depending of the tip sample distance and therefore from the cantilever oscillation. The work average over one oscillation period $T = 1/f$ is [46]:

$$\langle F(t) \cdot z(t) \rangle = -\frac{1}{T} \int_0^T F(z_0 + z(t)) \cdot z(t) \, \mathrm{d}t \tag{2.10}$$

where $z(t) = Acos(wt + \phi)$ and $z_0 + z$ is the tip surface distance.

From this expression the frequency shift is derived as [46]

$$\Delta f = \frac{-f_0}{\pi k A^2} \int_{-A}^{A} F(z_0 + z) \cdot \frac{z}{\sqrt{A^2 - z^2}} \, \mathrm{d}z \tag{2.11}$$

This expression for the frequency shift can be understood as the force between the tip and the sample integrated over the oscillation weighted with a larger interaction at the turnaround points.

As a useful expression for comparing results for different force distance curves the normalized frequency shift γ which is independence of cantilever parameters was introduced [32]:

$$\gamma = \frac{\Delta f k A^{3/2}}{f_0} \tag{2.12}$$

A schematic drawing of an implementation of a NC-AFM set-up operated in the FM mode is presented in figure 2.3. First, only the part with the yellow box is described where only a constant bias voltage V_{DC} is applied to the sample for equalizing electrostatic interactions. The sample and the cantilever are on supports with a piezo elements. The piezo element of the sample support allows the approach and precise sample movement in (x,y,z) direction. The piezo element from the cantilever support allows the excitation of the cantilever at its resonance frequency f_{res} by a PLL system (phase-lock-loop) (Lock-in amplifier + PLL-controller + PI-controller). The oscillation of the cantilever is detected with the beam deflection method where a laser beam is directed on the cantilever backside and reflected to a position sensitive photo diode (PSD). The diode drives an electric current

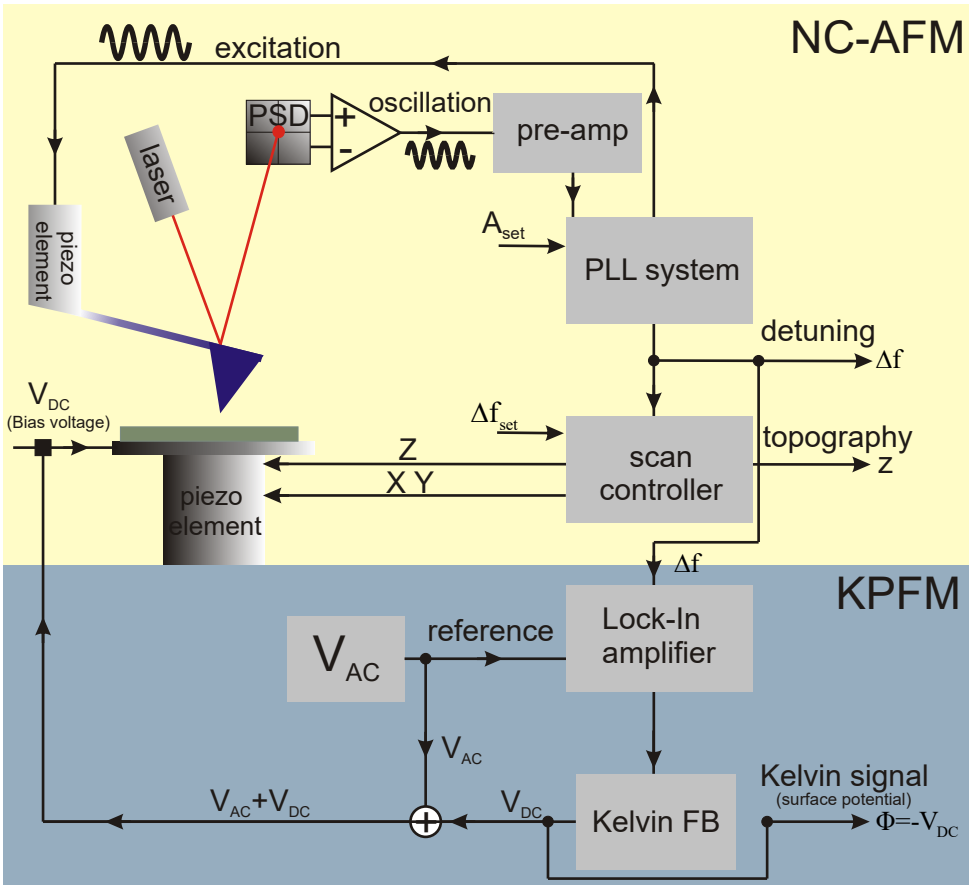

Fig. 2.3: Schematic drawing of the set-up of an AFM system operated in the non-contact mode with oscillation detection by the beam deflection method. The blue highlighted box shows the additional feedback for Kelvin Probe imaging. In modern systems the PLL system is often integrated in the scan controller system.

proportional to the incident light power. In case of a tip sample interaction the detuning of the cantilever leads to detectable changes of the laser spot on the photo diode which outputs a signal with sinusoidal modulation. This signal corresponds to the resonance frequency and is put through a preamplifier which converts the photo diode signal into a voltage signal. The signal is then forwarded into a Lock-in amplifier (LIA). The LIA detects the oscillation amplitude A and the phase (ϕ) of the input signal. The measured oscillation amplitude is compared to a given set point amplitude A_{set} and with a amplitude feedback-loop the excitation is adjusted in a way that the amplitude is kept constant. The phase is forwarded into a PLL-controller and adjusted to match a given set point. The PLL forwards the frequency shift Δf into the LIA with a feedback loop and hence, the phase is kept at a constant value. This is the locked state of the PLL. The output signal of the PLL is then used for the excitation of the cantilever [48].
The PLL systems outputs the amplitude A, phase ϕ, frequency shift Δf and the dissipation Γ which is the energy dissipated from the system to keep the amplitude constant.

The frequency shift is forwarded into a scan controller. The scan controller compares with a topography feedback loop the frequency shift with a pre-defined frequency shift

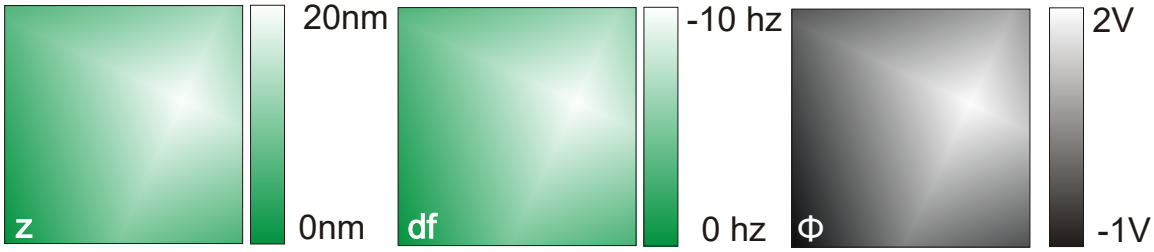

Fig. 2.4: Color code of topography (z) frequency shift (Δf) and KPFM (Φ) images. The color map is chosen in such way that higher feature appear brighter. As higher features usually lead to a stronger frequency decrease in Δf images, a brighter contrast is chosen for lower Δf values. For KPFM images, lower voltages are represented with a brighter contrast as they correspond to local higher potentials on the surface.

set point Δf_{set} and adjusts the z position of the cantilever in such a way that Δf matches Δf_{set}. The z adjustment is translated into the topography signal that is put out by the scan controller. This scanning mode is the *topography* mode where the recoded AFM image represents a topographic map where the x and y coordinates are the ordinates and the z position is represented by a color map. The color code is usually chosen in such way that higher z values are represented by a brighter color and lower z values with a darker color (see figure 2.4). A different scanning mode is the *constant height* mode [32]. Here, the topography feedback in the scan controller is disabled and a z-position close to the surface is kept constant. This results to a lower Δf at positions where the probe is near surface features and a higher Δf at positions where the probe is far away from surface features.

Due to the negative nature of the frequency shift the recorded Δf images is presented with inverted contrast in such way that topographic features are shown with corresponding color contrast as in the topography images (see figure 2.4).

The *constant height* mode is used for images with atomic resolution on flat scan areas as the fixed z position would lead to a tip crash when approaching higher surface features.
The third scanning mode is the *quasi constant height* mode [49,50]. Here, the topography feedback is not disabled but parameters (P,I gains) are set to values where the topography feedback reacts very slow. In this mode, a small inclination between the scanning plane and the surface can be compensated and, therefore, this mode is also safe. The samples used in this work show many irregularities and therefore we use the *quasi constant height* mode is predominantly.
Details on the electronic devices and scan controller for the NC-AFM implementation used in this work are listed in section 3.5. Note that quantities like the amplitude or the z positioning are not given in form of real physical quantities, instead all of these parameters have to be calibrated for an accurate conversation between a measured voltage and the corresponding physical quantity. Details on the amplitude calibration can be found in section 3.4 and in [51–54].

Fundamental Forces in NC-AFM

The frequency shift depends on all forces acting between the tip and surface. These forces are usually separated into long and short range forces acting attractive or repulsive [55, 56].

A force that is always present if a macroscopic object like a force microscopy tip is approached to the surface is the van der Waals force [57]. It results from fluctuations in the electromagnetic interaction between dipoles in the atoms of surface and tip. The van der Waals force can be separated in three components. The London dispersions force [58] describing the interaction between instantaneously induced dipoles in neutral atoms; this is the dominating part of the van der Waals force. The Debye force [59] describes the interaction of dipols induced by permanent dipoles in polar molecules. The interaction between permanent dipols depends on their orientation and is described by the Keesom force [60]. For a measurement in vacuum the van der Waals force is an attractive force and dominates for tip surface distances larger 1 nm. Assuming a spherical tip with radius R, the van der Waals force is expressed by :

$$F_{vdW} = -\frac{HR}{6z^2} \tag{2.13}$$

where z the distance of the tip from sample approximated by an infinite plane and H the material depend Hamaker constant [61].
Another force results from electrostatic interactions that have long and short range contributions and consist of image and capacitance forces [43]. This force results from on the polarization of conducting electrodes represented by tip and surface having different potentials. The electrostatic forces can be expressed by:

$$F_{el} = -\frac{1}{2}\frac{\partial C}{\partial z}V^2 - \frac{qQ}{4\pi\epsilon_0 z^2} \text{ with } \frac{\partial C}{\partial z} = -2\pi\epsilon_0\frac{R^2}{z^2 + Rz} \tag{2.14}$$

where the tip- sample system is described as a capacitor with capacitance C and V is the voltage. The second expression in the formula represents the coulomb interaction. The expression for $\partial C/\partial z$ is derived for a model of a metallic sphere with radius R that is located in front of an infinite metal surface [62].
Short range forces arise from chemical interactions and Pauli repulsion which preponderate at inter atomic distances. The Pauli exclusions principle forbids that identical fermions (e.g. electrons) occupy the same quantum state. When two atoms are approached at very small distances their electron orbitals overlap but for occupied orbitals electrons are not allowed to occupy the same states resulting in a strong repulsive force.

All of these forces can be principally calculated by solving the Schrödinger equation for the tip sample system. In practice, a solution of this equation is hard to handle for realistic conditions and a model potential is used to express the interactions between tip and surface.

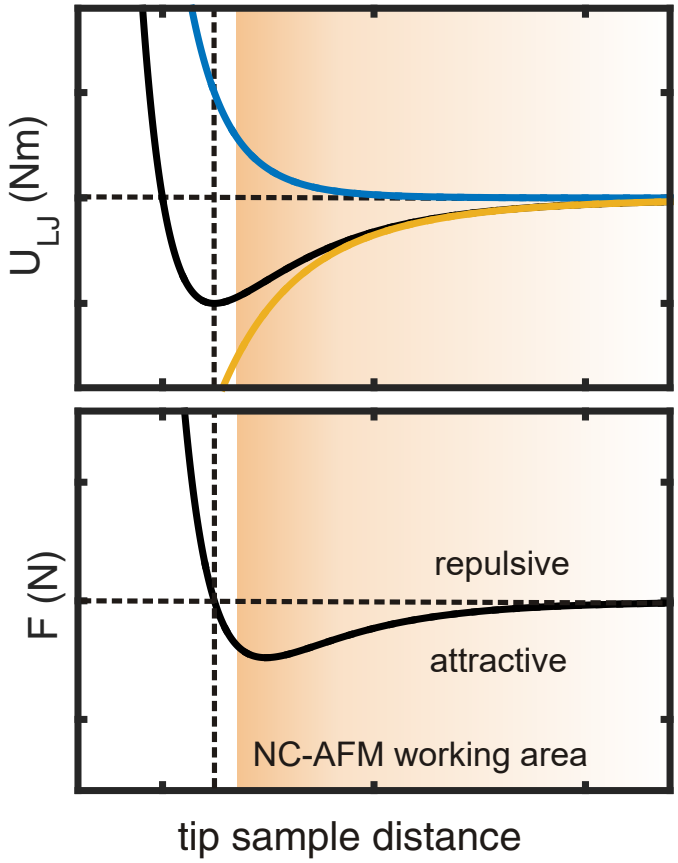

Fig. 2.5: Lennard-Jones potential and derived force with highlighted NC-AFM working area. The Lennard-Jones potential is separated into two terms which is shown by the blue and yellow curves representing repulsive and attractive contributions with the 12 and the 6 potency. As long the tip approaches the minimum of the force curve, the frequency shift will increase. If the minimum is passed, the frequency shift will decrease again and at F=0 change its sign. The usual NC-working range sweeps over a wide range depending on the amplitude of the oscillation and goes down to the local minimum of the force curve where the tip sample interaction is strongest.

A simple model potential is the Lennard-Jones potential which is represented by:

$$\begin{aligned} U_{LJ} &= 4 \cdot \epsilon * \left[\left(\frac{\sigma}{z} \right)^{12} - \left(\frac{\sigma}{z} \right)^{6} \right] \\ \rightarrow F_{LJ} &= -4 \cdot \epsilon * \left[\left(-12 \cdot \frac{\sigma^{12}}{z^{13}} \right) + \left(6 \cdot \frac{\sigma^{6}}{z^{7}} \right) \right] \end{aligned} \tag{2.15}$$

where z is the distance, σ the distance where the potential is zero and ϵ is the depth of the potential. The Lennard-Jones potential and the derived force are shown in figure 2.5. The potential is a superposition of an attractive force like van der Waals forces represented by the z^6 term and a repulsive force due to Pauli repulsion represented by the z^{12} term.

The usual NC-AFM working range is highlighted in the figure and goes down to or a bit further than the minimum of the force curve. This position is the lower turning point of the tip and critically determines the contrast in large amplitude NC-AFM imaging. For amplitudes of 10 to 20 nm, the upper turning point of the oscillation would be where the force curve nearly reaches zero and does only contribute insignificant to the contrast in NC-AFM images.

2.4 Kelvin Probe Force Microscopy

The Kelvin Probe Force Microscopy (KPFM) technique allows the measurement of the local work function Φ of conductive surfaces and electrostatic potentials on insulating surfaces with very high spatial resolution. KPFM measurements are performed during NC-AFM measurements. The technique was first implemented by Nonnenmacher et al. in 1991 [63], and is in fact the implication of the classical Kelvin Probe into NC-AFM.
Historically, the Kelvin probe technique is based on observations from Lord Kelvin [64]. He found in 1898 that a voltage builds up between different metals that are separated from each other just after they have been in contact. The phenomenon stems from Fermi levels for different metals that lead to a contact potential difference (CPD). The metal with the lower work function transfers electrons to the metal with the higher work function. Due to the different charges an electrostatic force builds up. With an externally applied bias voltage V_{DC} that is adjusted in such a way that it matches V_{CPD}, the Fermi Levels of the metals shift to their natural position and the CPD is measured.
The system of a metallic tip and metallic sample is considered as a capacitor where the contact potential difference is given by:

$$V_{CPD} = \frac{\Delta\Phi}{e} = \frac{\Phi_s - \Phi_t}{e} \tag{2.16}$$

with Φ_s and Φ_t being the work functions of the tip and sample, respectively and e as elementary charge. Note that because the bias voltage is applied to the sample, we measure $\Phi_s - \Phi_t$. A schematic drawing of this procedure is shown in figure 2.6. When tip and sample are separated their Fermi levels are on different values. After a electrical connection is established the Fermi levels compensate and an electrostatic force field $\mathbf{F}_{el}$ builds up. A bias voltage V_{DC} is applied and adjusted so that the electrostatic force is compensated.

Without a modulation in KPFM the bias voltage V_{DC} is obtained by $\Delta f - U$ curves where the frequency shift Δf is measured as function of the applied voltage V_{DC}. One measured $\Delta f - U$ curve is presented in figure 2.7. According to equation 2.14 it can be derived that

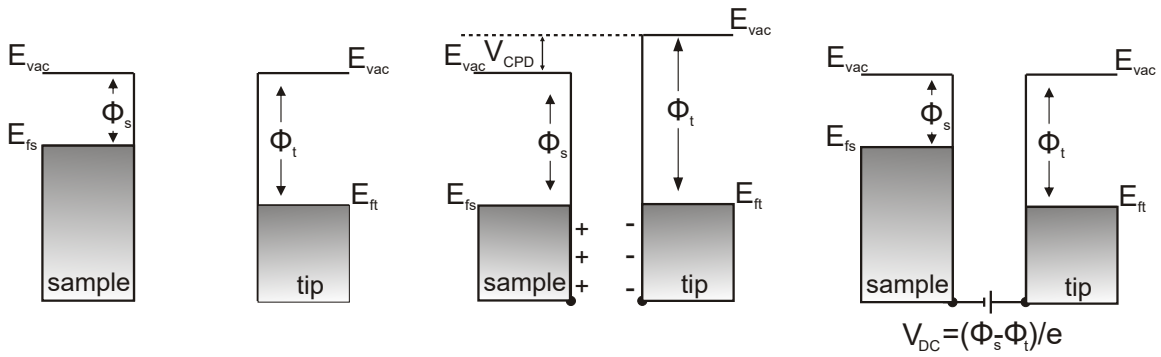

Fig. 2.6: Schematically presentation of the Kelvin compensation of the contact potential difference (CPD) between a conductive tip and conductive surface.

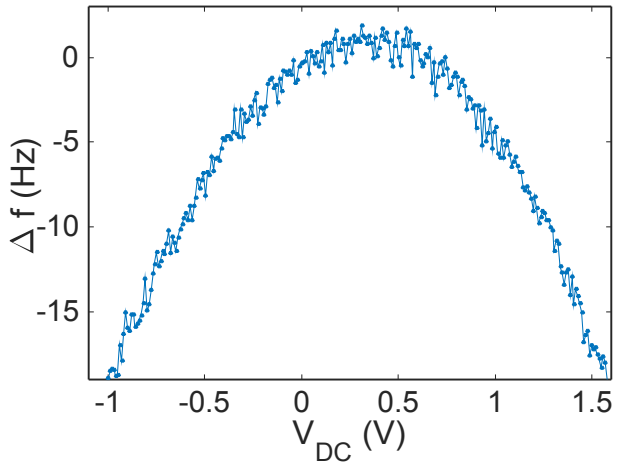

Fig. 2.7: Selected $\Delta f - U$ curve for an insulating ceria film surface. The frequency shift depends parabolic on the applied voltage V_{DC} and has its minimum for $V_{DC} = V_{CPD}$. Already small changes in the voltage lead to a strong Δf shift. This allows the use of relative small amplitudes for V_{AC}.

the frequency shift depends parabolic on the applied voltage V_{DC}. Δf is minimized for $V_{DC} = V_{CPD}$ (here approx. 480 mV).
In conventional KPFM, in addition to the bias voltage V_{DC}, an ac-voltage $V_{ac}\sin(w_{ac}t)$ oscillating with frequency w_{ac} is applied in series resulting into an oscillating electrostatic force, which in turn results into cantilever oscillation at w_{ac} and satellite peaks around the resonance frequency (see next section 2.4.1 in figure 2.8) [62, 65].
According to equation 2.14 the electrostatic force is given by :

$$F_{el} = -\frac{1}{2}\frac{\partial C}{\partial z}\left[V_{DC} - V_{CPD} + V_{ac}\sin(w_{ac}t)\right]^2 \tag{2.17}$$

With the separation of the electrostatic force into different contributions equation 2.17 can be written as:

$$\begin{aligned} F_{el} &= F_{dc} + F_{w_{ac}} + F_{2w_{ac}} \\ F_{dc} &= \frac{1}{2}\frac{\partial C}{\partial z}\left[(V_{dc} - V_{CPD})^2 + \frac{V_{ac}^2}{2}\right] \\ F_{ac} &= \frac{\partial C}{\partial z}(V_{dc} - V_{CPD}) \cdot V_{ac}\sin(w_{ac}t) \\ F_{2ac} &= \frac{\partial C}{\partial z}\frac{V_{ac}^2}{4}\cos(2w_{ac}t) \end{aligned} \tag{2.18}$$

The spectral component F_{ac} at the modulated frequency w_{ac} is hereby used to measure the CPD. This is accomplished by the KPFM feedback loop adjusting V_{DC} to V_{CPD} so that F_{ac}=0. The measured CPD is the combined work function from the sample-tip system. In order to deduce the absolute work function of a sample a calibrated tip with a known work function has to be used. . Otherwise, the calibration can be done if more than two materials are present on the surface with the work function of one of the materials being known.
However the equations 2.17 and 2.18 are not helpful for analysing non-conductive surfaces like those investigated in this work where the influence of the local surface charges and dipoles are of importance. This can be done by considering an additional Coulomb

interaction as discussed in [66].

$$F_{el} = \frac{\partial C}{\partial z} V^2 - \frac{q}{4\pi\epsilon_0 z^2}(Q_s) \tag{2.19}$$

whereby $Q_s = -(C \cdot V + q)$ is the charge of a tip approximated as a sphere over an infinite surface approximated as plate forming a capacitor with the Charge $C \cdot V$. The quantity q is a point charge on the surface which introduces an image charge in the tip. With this model F_{ac} changes to [65]:

$$\begin{aligned} F_{ac} &= \left(\frac{\partial C}{\partial z}(V_{dc} - V_{CPD}) - \frac{C \cdot q}{4\pi\epsilon_0 z^2} \right) \cdot V_{ac} \sin(w_{ac} t) \\ \rightarrow 0 &= \frac{\partial C}{\partial z}(V_{dc} - V_{CPD}) - \frac{C \cdot q}{4\pi\epsilon_0 z^2} \end{aligned} \tag{2.20}$$

Although, this equation is more suitable to express a local surface charge on insulators it has to be stressed that determining the amount and distribution of charges is in general very complicated and needs the assistance of theory. Therefore, in this work all KPFM images are explained only on a phenomenological basis.

2.4.1 Implementation of the KPFM

The KPFM technique can be implemented in the amplitude modulation (AM) or in the frequency modulation (FM) mode. In the AM mode a ac-voltage is applied to the bias voltage and with a LIA the amplitude of that frequency in the cantilever oscillation is detected. As the resonance frequency is already used for the topography measurement usually higher harmonics are chosen as the oscillation frequency w_{ac} (see figure 2.8) for best signal-to-noise ratio (SNR) [67]. The AM-mode is susceptible for cross talk with the topographic signal and usually requires a slow scanning speed and often preamplifiers with an extended bandwidth [67].

In FM-KPFM the ac modulation with the oscillation frequency w_{ac} results in satellite peaks around the resonance frequency (see figure 2.8). The peaks are referred to as the Kelvin sidebands and the frequency modulation is measured. In FM-KPFM two different options allow the measuring of the frequency modulation. The first option is the classic FM KPFM (sequential FM Kelvin) where the amplitude of the oscillation is measured in the Δf channel. The second option is the sideband KPFM where the amplitude is

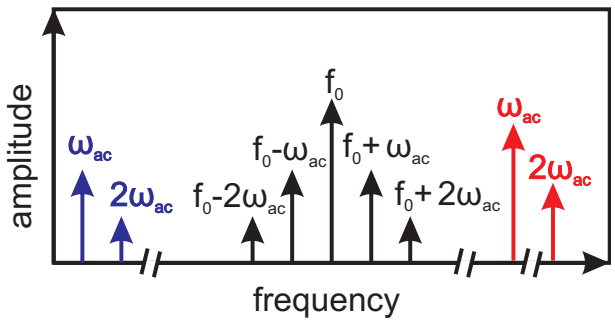

Fig. 2.8: Illustration of a FFT plot of a frequency modulated signal at w_{ac} showing the Kelvin sidebands for AM and FM KPFM.

measured at $f_0 + w_{ac}$ [67].
The implementation of the classic KPFM technique in the FM mode is shown in the shaded part in figure 2.3. The frequency shift Δf and the ac-voltage V_{ac} as a reference signal are forwarded into a Lock-In amplifier. The Bias voltage V_{ac} is modulated at f_{ac}=1234 Hz, which is much smaller than the cantilever frequency. Therefore, this modulation frequency prohibits crosstalk with the frequency shift and the topography feedback response. The amplitude is adjusted at $V_{ac} = 0.5 - 1V$ (RMS) which leads to a sufficient signal of f_{ac} of the detuning signal. The Kelvin feedback detected by a Lock-In amplifier adjusts continuously V_{DC} to minimize F_{ac} and thus yields V_{DC} which is the Kelvin imaging signal corresponding to the surface potential. The advantage of the FM method compared to the AM method is a higher scanning speed and a higher lateral resolution in KPFM images [67].

The color coding of KPFM images is shown in figure 2.4. Instead of the applied bias voltage V_{DC}, the images reveal the surface potential Φ. The surface potential has the converse sign as the applied Bias voltage (e.g. for a surface potential of -2 V a Bias voltage of 2 V has to be applied to equalize this potential).

A lower surface potential corresponds to a higher V_{DC} and is represented with a dark contrast on a gray scale while a higher surface potential corresponds to a lower V_{DC} and is represented with a bright contrast.

2.5 Presentation of images

The image analysis and image processing is performed with the software Gwyddion [68] and WSXM [69] whereby the former is mainly used. In the previous section the color maps for different images (z, Δf, Φ) were already discussed. Here image post processing is explained. In figure 2.9 the result of different post processing filters is shown for a typical

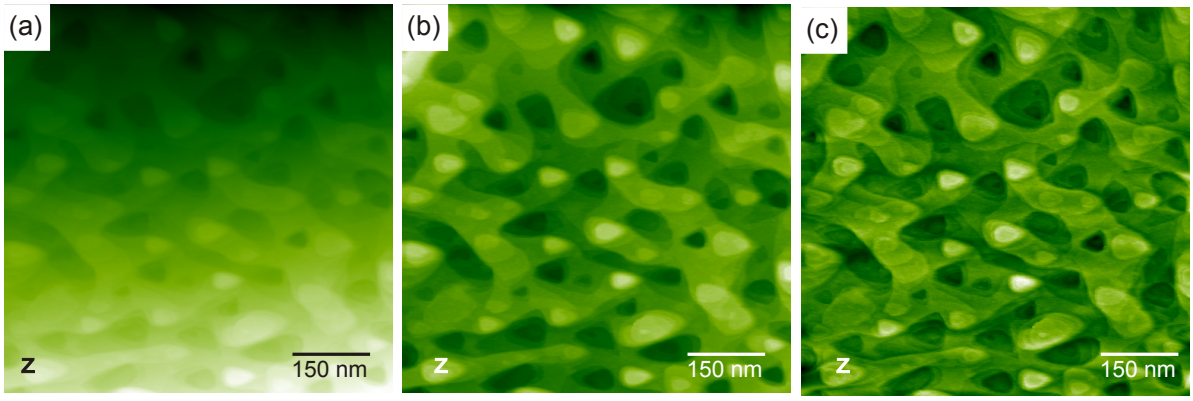

Fig. 2.9: (a) NC-AFM topographic image without any post processing. (b) The same image after post processing with a plane filter. (c) Additional filters applied (polynom 3dg, sharpen 5 px).

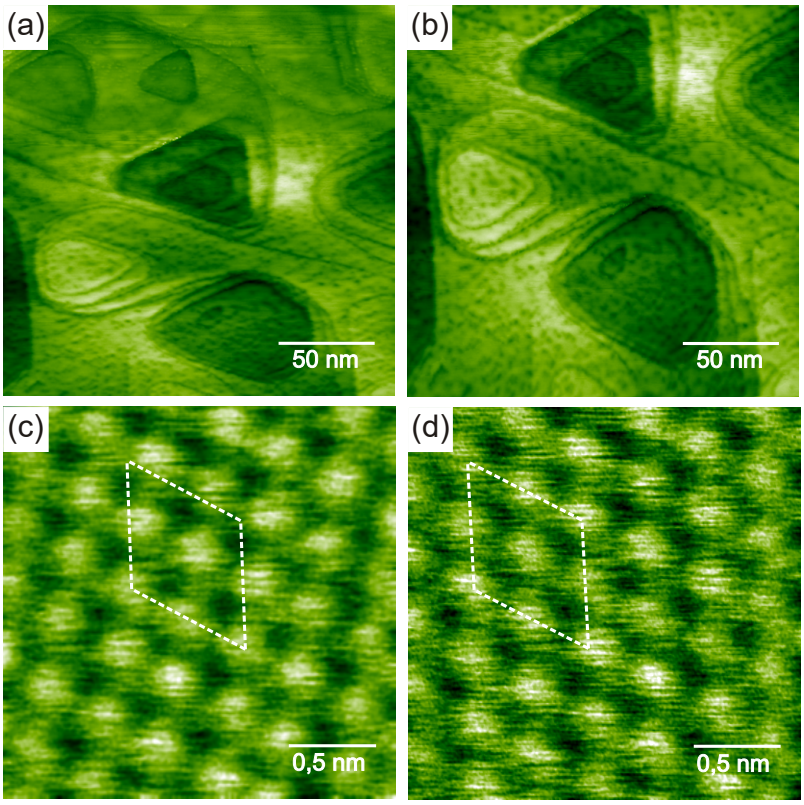

Fig. 2.10: (a,b) NC-AFM topographic images showing the effect of piezo creep. (c,d) NC-AFM topographic images showing the effect of thermal drift. (c) Uncorrected image. (d) The same image using the Gwyddion 'Affine Distortion' filter to reveal the impact of the drift.

NC-AFM topographic image. The slope is usually corrected manually during measurements but it may happen that the correction is unsatisfactory especially when the scan area is enlarged. This lead to a result as presented by the image (a) which is recorded with the NC-AFM system and presented without post-processing. The slope leads to a contrast extending from dark to bright in y direction. As this contrast extend is clearly not affiliated to the surface structure a plane filter is applied that flattens the measured surface topography in the image. The result of flattening is shown in frame (b). The surface structure can be seen much better after the plane filter is applied as the height differences of step edges are not suppressed by the additional slope anymore.
The plane filter is applied on most of the topography images presented in this work. For presentation reasons, in some cases additional filters are applied to the images. In (c) a polynom fitting filter (3dg) and a sharpen filter (5px) is used during post processing of the image. This leads to a better visual appearance of surface features like pits, protrusions, terraces and step edges. However, a polynom filter can possibly flatten nearly every surface and this can lead to a adulteration of the contrast and misrepresentation. Therefore, in this work this filter type is only used for visualization purposes and not for quantitative data analysis. Another problem for image presentation is strong drift in images. Usually at the beginning of a measurement there is a strong drift in images due to piezo creep effects as shown in figure 2.10 (a,b). As the used NC-AFM system has a relative huge possible piezo expansion the creep can cause that the first recorded images look compressed or expanded. This problem is eliminated by waiting up 30-60 min till the creep is not relevant anymore. A drift factor that can not be eliminated at room temperature is the thermal drift. The thermal drift is much lower than the piezo creep but is clearly

visible in images with very high resolution. Figures 2.10 (c,d) show an atomic resolution example measurement. Due to the thermal drift, the expected hexagonal structure is distorted. This can be correct with the function 'Affine Distortion' from the free SPM software Gwyddion [70]. This filter is problematic as it requires the knowledge over the observed atomic lattice.
Furthermore averaging filters, FFT filtering, error line removal and background subtraction, local contrast enhancement and drift correction filters are used for image presentation in this work in a manner that the visual presentation of images is optimized but the quantitative data interpretation is not affected.

3 Description of the NC-AFM system

In this chapter, first the vacuum chamber and the NC-AFM system is presented. Then modifications of the set-up that are a result of this work are described. Furthermore, the preparation of samples for high resolution NC-AFM measurements is described.

3.1 Vacuum chamber

Under normal ambient conditions (T=273 K; p=1013 mbar) gas molecules from the air absorb on surfaces instantaneously and a surface characterization with NC-AFM and KPFM would be very limited. To prepare and maintain surfaces free of contaminations a preparation and measurement at a pressure in the low 10^{-10} mbar range is mandatory. Under such ultra-high vacuum conditions sample surfaces will get covered with a contamination layer only after many hours or a few days depending on the reactivity of the surface.

An illustration and photo of the UHV chamber used in this work is presented in figure 3.1. The UHV system was originally set up by R. Bennewitz and thereafter improved by C. Barth (1996-2001), S. Gritschneder(2001-2005), S. Torbrügge (2005-2009) and H. Pieper (2009-2012) [65, 71–73]. To ensure optimal conditions, the UHV-chamber is evacuated with different pumps. As main vacuum pumps a rotary vane pump connected to a turbo-molecular pump , an ion getter pump and a sorption pump are used. Additionally a titanium sublimation-pump is frequently switched on. With these pumps and after a slight modification (see chapter 3.3) a base pressure in mid to low 10^{-11} mbar range is reached after a bake-out. The system is separated in three parts: the load lock chamber (A), the preparation chamber (B) and the microscope chamber (C). The load-lock chamber can be separated from the preparation chamber by a valve shown in figure 3.1 and is then evacuated separately by the rotary vane and turbo-molecular pump only. The design of the load lock allows the transfer of up to four probes or samples and is described in detail in [65]. The preparation and microscope chamber are directly connected to each other by design and cannot be separated by a valve. In the preparation chamber tips and samples can be sputtered and samples can be annealed [74] (see section 3.6), a mass spectrometer and a metal evaporator (EFM3, Omicron,Taunusstein, Germany). The measurement chamber is equipped with the microscope, a wobble- stick for sample and tip exchange and a camera for the optical tip sample approach.

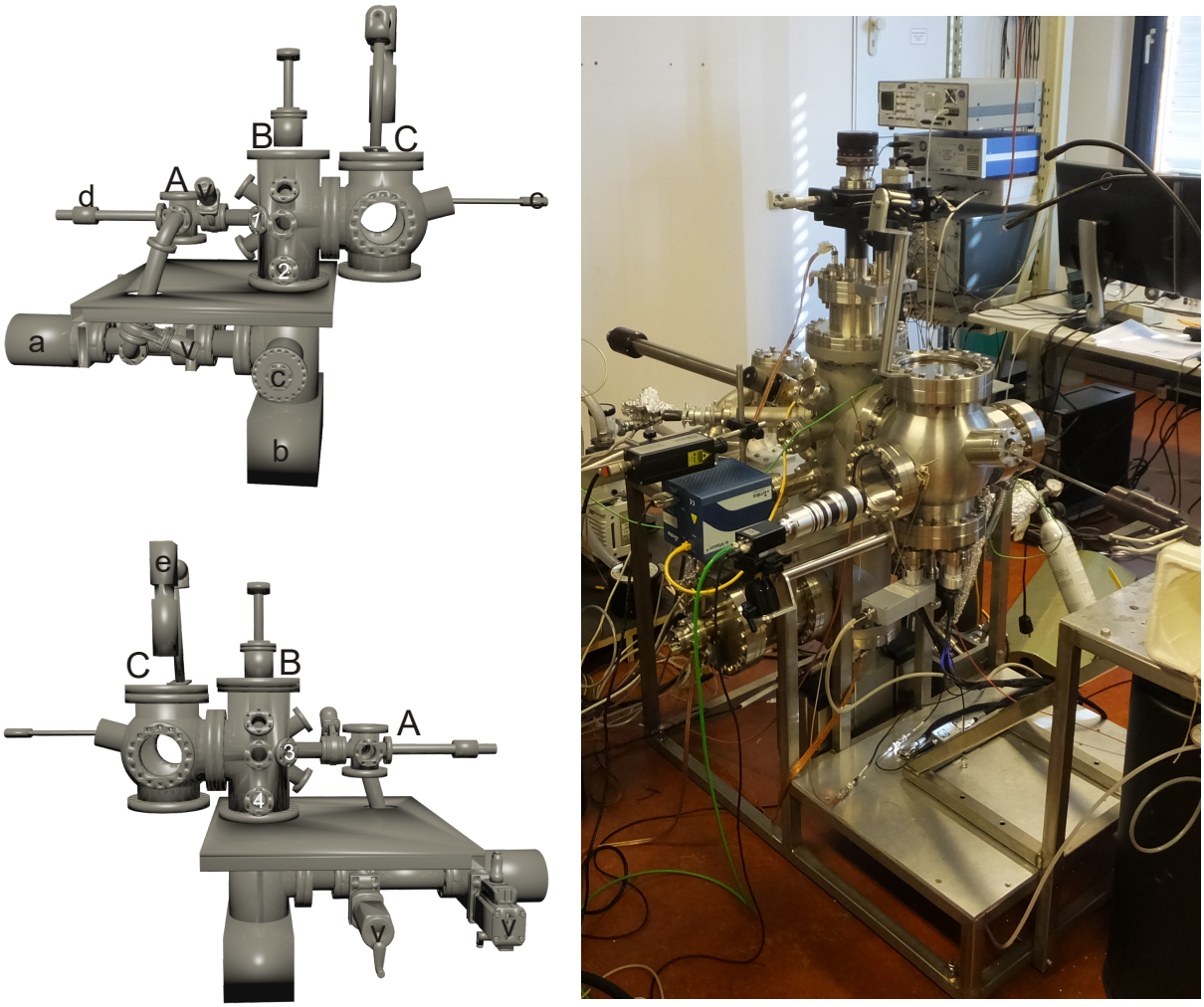

Fig. 3.1: Photo and 3D illustration of the UHV chamber set-up. The set-up can be separated into three main parts: (A) load-lock chamber, (B) preparation chamber, (C) AFM-microscope chamber. The system can be pumped by a turbo-molecular- pump (a), a ion getter- pump (b), a titanium sublimation-pump (c) and a sorption pump (not shown). (d) Magnetic manipulation arm for sample transfer. (e) Camera with magnification lens. (f) Wobble stick . The rotary vane pumps are not shown. Additional at the flanges are attached a ion-sputter gun (1) a mass spectrometer (2) a evaporator (3) and a argon gas support (4).

3.2 NC-AFM system

The microscope is a commercial room temperature atomic force microscope (AFM/STM, Omicron, Taunusstein, Germany) which is based on the design introduced by Howald et al. [75]. The AFM stage is separated into two parts, namely the mirror housing and the sample housing which is shown in the photograph in figure 3.2 (a). Both contain piezo elements for the tip sample approach, scanning slider and cantilever excitation. The approached state of the NC-AFM is shown in figure 3.2 (b) where the piezo element in the sample housing is extended so that the sample surface is nearly in contact with the tip of the cantilever. For positioning of the samples only a movement in horizontal directions is

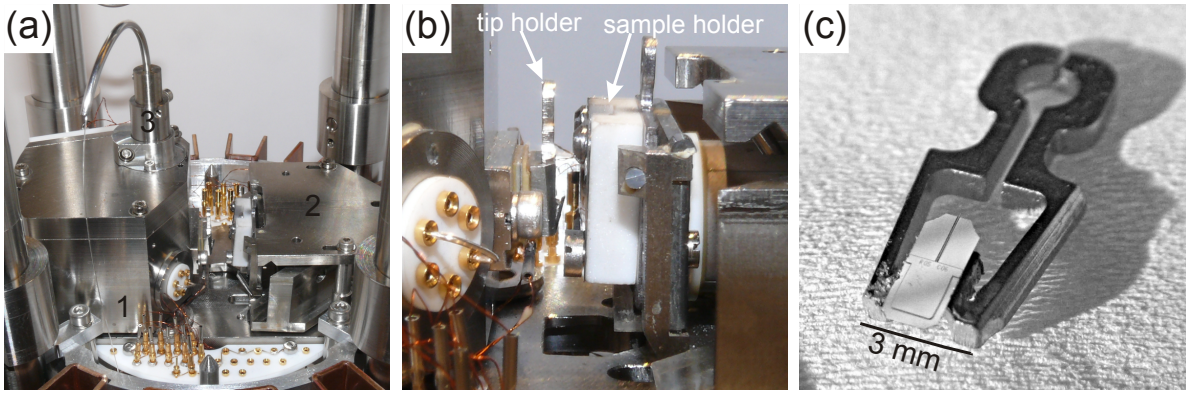

Fig. 3.2: (a) Photo of the AFM-microscope. The main parts of the AFM stage are the mirror housing (1) with the cantilever holder and the light source (3) and the sample housing (2). Both housings contain piezo elements for tip- sample approach, scanner movement and probe oscillation. (b) AFM in approached state where the sample is approached to the fixed tip. (c) Foto of a cantilever attached to probe holder.

possible as the sample slider allows no height corrections outside the scanning movement range with has a maximum area of 6 μm × 6 μm.
For the probes commercial silicon cantilevers (PPP-NCH; NANOWORLD®, Switzerland) are used which have a resonance frequency in the range of 270 to 350 kHz and a stiffness of typically 42 N/m. The higher stiffness compared to similar 70 kHz probes allows the use of smaller amplitudes in NC-AFM experiments which is an advantage for achieving atomic resolution in many cases. The probes have a tip radius of <10 nm, a tip height of 10 to 15 μm, a mean width of 30 μm and the cantilever has a length of 125 μm and no reflective coating. The cantilevers are carefully glued on special tip holders. For this purpose, a camera with a high magnification objective is used and the cantilever position is determined with a template on a monitor. The glue is a vacuum resistant conductive epoxy (EPO-TEK® EE129-4; Epoxy Technology, Inc. Billerica, MA 01821, USA). Because the attachment of the cantilever on the tip holder is done by hand with tweezers, some experience is necessary to glue several cantilevers nearly identical. A cantilever attached on a tip holder is shown in the photograph in 3.2 (c).
To detect the cantilever oscillation, the well-known and easy to implement optical beam deflection method (OBD) is used. The OBD method is completely implemented in the mirror housing. A 3D illustration of the interior set up of the mirror housing is presented in figure 3.3. The beam deflection method is realized over a system of lenses and mirrors. The light beam is focused first through a lens system onto a mirror that can be rotated in very fine steps over a piezo element. The light beam is directed from the mirror onto the oscillating cantilever from where the light beam is reflected to a second rotatable mirror. This mirror is adjusted in a way that the light beam is redirected onto the photodiode converting the light power into a measurable current signal.

In the original setup of the mirror housing, the light source for the beam deflection method was a LED. One significant change in the OBD was the exchange of this LED with an external laser light source by Torbruegge et al. [76] in 2008. The temperature

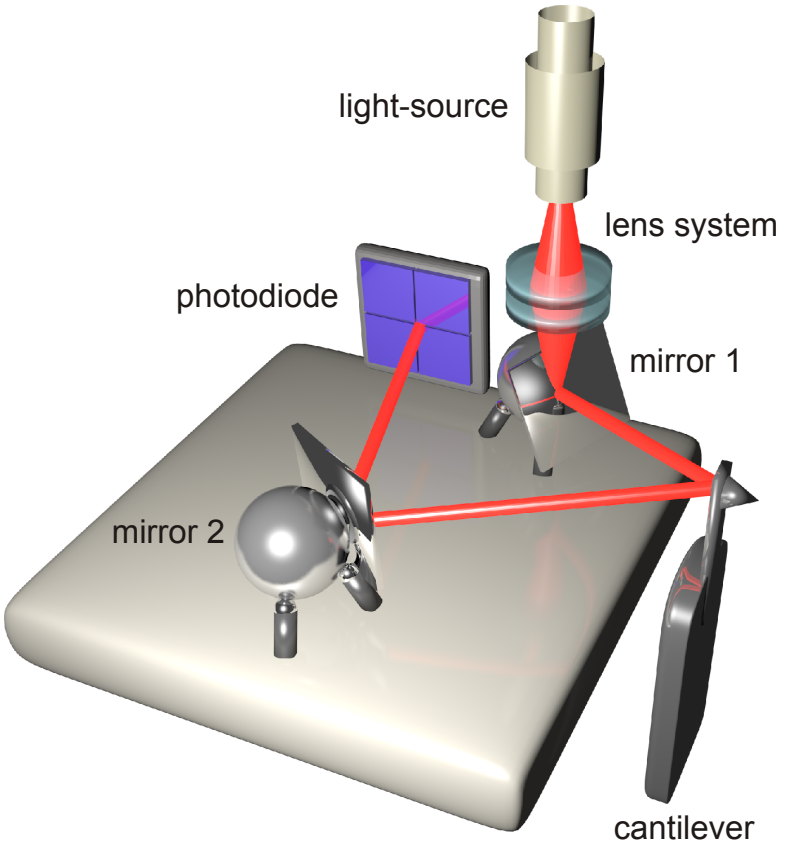

Fig. 3.3: 3D illustration of the interior set up of the mirror housing. The beam deflection method used for the cantilever oscillation detection is realized over a light source that is focused over a lens system on a mirror (mirror 1). The reflection of the free moveable mirror is adjusted so that the light beam hits the cantilever. The deflection of the cantilever is directed on a second free moveable mirror (mirror 2)which reflects the light to the photodiode. The photodiode then converts the light power into a measurable current.

controlled laser diode (48TE-SOT, Schäfter und Kirchhoff, D-22525 Hamburg, Germany) has a wavelength of 685 nm and a adjustable output power of up to 12.9 mW which is much more than the power which could be achieved with the original LED. Also the divergence of the laser beam is much smaller compared to the light beam of a LED. The laser source cannot be operated in the UHV-chamber and, therefore, a special UHV feedthrough for the optical fiber guiding has to be installed. Details of this feedthrough can be found in [76]. The UHV feedthrough was based on a fitting (Swagelok, Solon Ohio,USA) welded onto a 16 CF flange and a conically shaped Teflon ferrule. (see figure 3.4 (a)). The Teflon ferrule has a center drilled hole with a diameter just slightly larger than the fiber. With a nut the diameter can be reduced so that the fiber is pinched in the drilled hole and the UHV-feedthrough is sealed. The fiber is protected against breaking with a strain relief secured at the flange. Beneath the AFM stage, the fiber is laid in circles around the push pull motion (PPM) and held in place with spacers 3.4 (b). This is necessary as the AFM stage can be lifted up and down and the fiber must be able to accommodate for this. The connection to the mirror housing is realized via a U-tube and a metal cylinder. The fiber is directed through the U-tube and the end of the fiber is glued with Torr Seal®(Agilent Technologies, 10040 Leini, Italia) in the metal cylinder in such a way that only 1-2 mm stick out of the cylinder. This is necessary as a longer loose fiber end would be prone to oscillations. Before the fiber is attached the sheathing is removed and the end is cleaved with a fiber cleaver (PK Technology FK 11 Fiber Optic Cleaver). For the removal of the sheathing the fiber is soaked in acetone for 30 minutes and after that the sheathing can

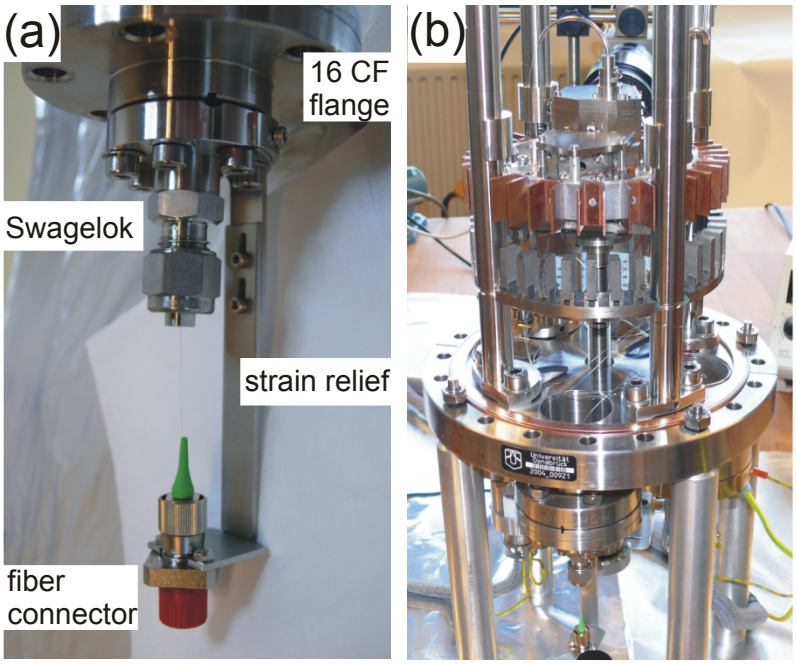

Fig. 3.4: (a) Photo of the UHV Swagelok feedthrough for the glass fiber. (b) NC-AFM scan head after the exchange of the LED with the Laser diode. The optical fiber is coiled several times around the push pull motion beneath the AFM stage. At the end the fiber is directed through an U-tube and glued in a cylinder which is placed at the position of the original position of the LED. The connection at the mirror housing can also be seen in figure 3.2 (a). Photos by Lübbe.

be stripped from the fiber by hand. The fine adjustment of the cylinder position on the mirror housing is realized with the optical study of the divergence of the laser beam after it has past the lens system on a paper strip fixed on a cantilever holder. The cylinder is fixed at the position where the spot has its smallest diameter on the sheet of paper that mimics the back of the cantilever.
Also the original pre-amplifier was replaced with an optimized home-built one. Details can also be found in [76]. The modifications lead to a decrease of the deflection spectral noise density of the NC-AFM setup. The original spectral deflection noise density was 2757 fm/$\sqrt{\text{Hz}}$ which could be reduced by to 272 fm/$\sqrt{\text{Hz}}$ for a $\sum$-signal of 6 V after the modifications (see section 3.4).

3.3 Modification of the NC-AFM setup

During the course of this work, some changes at the setup were done. These include the modification of the fiber feedthrough and the exchange of the photodiode. Further, the preamplifier was exchanged again and new SPM electronics was set up. These modifications and their impact on the deflection noise spectral density are described here.

3.3.1 UHV feedthrough

The Swageleok UHV feedthrough for the fiber had been used over 4 years successfully but in practice it turned out that clamping the fiber has a huge disadvantage. With every bake out of the chamber which is performed about two times every year, the clamping of the feedthrough expands due to the higher bake out temperature. This results in a leak after every bake out. To seal this leak the nut on the Swageleok UHV feedthrough

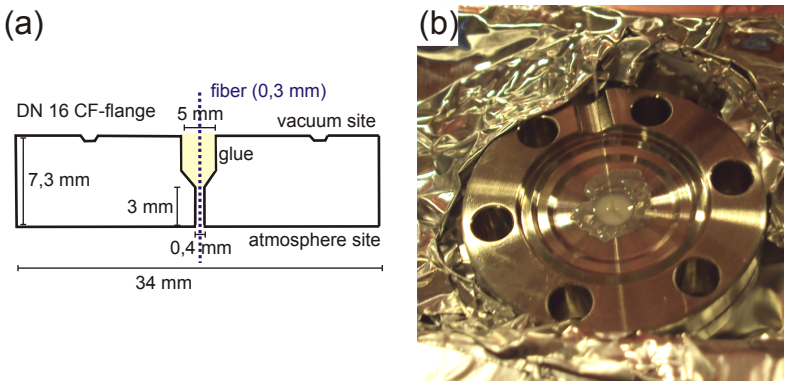

Fig. 3.5: (a) Schematic drawing of the 16 CF flange for the new optical fiber UHV-feedthrough. (b) Photo of the vacuum site of the flange with the glued fiber.

has to be tightened after every bake out which results in a stronger pinched fiber. After approx. 10 bake out cycles the pinching of the fiber is so strong that the fiber itself get crushed.

This was the case at the beginning of this work. With the maximum laser power of 12.9 mW at the fiber connector only 0.126 mW at the fiber end could be achieved. To get a useful light intensity from the cantilever reflection on the photodiode a minimum power of approx. 0.5 mW is needed. Therefore, the exchange of the optical fiber was unavoidable.
To prevent crushing of the fiber again the UHV-feedthrough was rebuilt and the pinched fiber exchanged with a glued fiber. As the Swagelok UHV feedthrough is attached to a 16 CF flange, it is the easiest way to use a modificated 16 CF flange for the new attachment of the fiber. A schematically drawing and a photo of this modification is shown in figure 3.5. In the 16 CF flange, a 0.4 mm diameter hole is drilled with which is only 0.1 mm more than the diameter of the fiber. At the vacuum site of the flange the hole is widened to a diameter of 5 mm. This has two advantages. First, it is technically difficult to drill a hole with 0.4 mm diameter through the complete 7.3 mm thick flange and, second, the bigger opening allows a much better attachment of the fiber with glue and a better sealing of the opening. For the sealing Torr Seal® is used. The other part of the fiber set up is rebuilt or reused as in the described previous modification by Torbruegge et. al. [76]. For the reuse of the cylinder we removed the glued old fiber from the metal cylinder by annealing the cylinder at 450 °C which lead to a breakup of the Tor Seal® in the cylinder. After several additional clean ups in an ultrasonic bath with isopropanol, the cylinder drilling was completely free of any glue remains.
To test the new fiber optics the input power is compared to the measured power at the fiber end. For a input power of 12.9 mW a power of 12.2 mW could be measured at the fiber end which is a loss of only 5%. In practice, the glued fiber was baked out without any problem several times and no leak after a bake out occurred so far. The glued fiber also improves the vacuum conditions. With the clamping feedthrough, the best pressure that could be achieved after a bake out was $1.0 \cdot 10^{-10}$ mbar. With the glued fiber the pressure after a bake out is $3 \cdot 10^{-11}$ mbar.

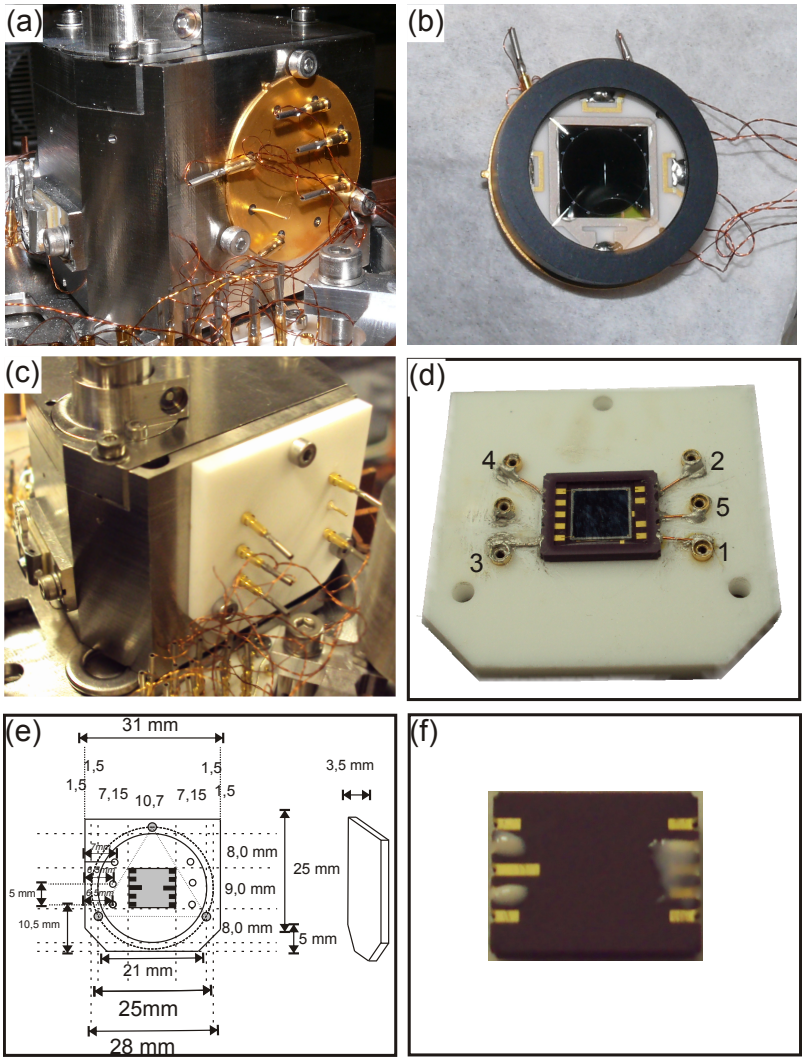

Fig. 3.6: (a) Photo of the original photodiode mounted on the back side of the mirror housing. (b) Front view of the original photodiode. (c) The new build replacement mounting for the new photodiode. (d) Front view of the new smaller photodiode (Hamamatsu Si PIN photodiode S5980) attached to the new mounting with connected pins. (e) Schematic drawing of the dimensions of the replacement mounting. (f) Back side view of the photodiode with isolated pins.

3.3.2 Exchange of the original photodiode

One reason for noise in the optical beam deflection systems is noise caused by the photodiode. The original photodiode used in the NC-AFM set up is shown in figure 3.6 (b). The active photodiode area is relatively large (approx. $80\,\mathrm{mm}^2$) which is not optimal for a low noise floor. An easy way to decrease the noise level is to use a photodiode with a smaller active area. For this reason we choose the Hamamatsu Si PIN photodiode (Hamamatsu Photonics, Hamamatsu, Japan) of the type S5980 which has an active area of $5 \times 5\,\mathrm{mm}^2$ [77]. The original position and mounting of the omicron photodiode is shown in figure 3.6 (a). The photodiode is placed in the middle of a circular port which is hold in place with three screws in a rounded recess on the back side of the mirror-housing. The pins on the back side of the circular port are connected to pluggable cables in the AFM. To keep the new photodiode mounting as simple as possible we reuse the connectors and the three boltings of the original photodiode mounting. For this the new photodiode holding uses the same connector type. The attached Hamamatsu photodiode is shown in 3.6 (d). The basis of the holder is a Marcor® (Corning, Inc. ; Corning , USA) plate. The edges at the downside of the basis plate are beveled to fit into the AFM-stage. Detailed

Tab. 3.1: Diode contacts at flow direction should have 0.6 V while the resistance should be approx. 3-4 MΩ. Also if the photodiode is not connected the resistance between pin 1-2, 1-3, 1-4, 2-3, 2-4, 3-4 is R=4-10 kΩ

pin 5 (common) connected to	U (V)	R (Ω)
1	0.59	>3 M
2	0.59	>3 M
3	0.59	>3 M
4	0.59	>3 M

dimensions of the basis plate are listed in 3.6 (e). For the connectors, six small holes are drilled into the base plate and three holes for the boltings. The connectors and the photodiode are glued with Torr Seal®. Small pieces of copper wire are connected with a conductive epoxy glue (EPO-TEK®EE 129-4) to the appropriate pins on the photodiode. To minimize the risk of connecting accidentally false pins on the photodiode some pins are isolated with Tor Seal® which is shown in figure 3.6 (f). Instead of using the epoxy glue one could also solder without flux the connections but this is more difficult and one has to concern that the photodiode cannot withstand temperatures above 125°C. The used epoxy hardens at room temperature in a short time and then the connections are checked with a multimeter. If the connections are correct the listed values in table 3.1 should be measured. In figure 3.6 (c) the finished new photodiode holder is shown mounted at backside of the mirror housing.

3.3.3 Replacement of the pre-amplifier

Also the preamplifier is exchanged. The new pre-amplifier is home-built and optimized for low noise operation covering the frequency range of 25 to 350 khz that is suitable for standard cantilevers having resonance frequencies in the range of 70 kHz or 300 kHz. A photo of the new preamplifier is shown in figure 3.7. Beside the optimized low noise operation, the pre-amplifier consists of a digital display that shows the position of the laser spot on the four quadrant photodiode and the total amount of the laser power ($\sum -signal$) what is most helpful for the correct positioning of the second mirror.

Fig. 3.7: Photo of the new home build pre-amplifier with display for the positioning of the laser spot on the photodiode.

3.4 Determination of the noise floor of the modified Omicron NC-AFM system

The modifications on the set-up yielded a significant improvement of the noise floor of the NC-AFM system. For obtaining best results, it is mandatory to regulary determine the noise floor of the system.

A cantilever excited with an usual external source exhibits a very high amplitude at its resonance frequency as shown in figure 3.8. But even without an external excitation a cantilever oscillates in its eigenmodes due to thermal excitation. The measurement of the thermal excitation allows a precise determination of the noise spectral density. Based on the work of Hutter et al. [78], this method also allows the determination of the cantilever stiffness.
A detailed explanation how to measure the thermal peak for a beam deflection NC-AFM system and how to derive the noise floor and cantilever stiffness is given in [52] and [79]. With a spectrum analyzer the total displacement noise spectral density $d^z_{\mathrm{tot},0}(f)$ for the fundamental cantilever oscillation mode is measured for the tip being retracted from the surface. The total displacement noise spectral density is given by:

$$d^z_{\mathrm{tot},0}(f) = \sqrt{\frac{2k_BT/(\pi k_0 f_0 Q_0)}{(f^2/f_0^2-1)^2+(f/(f_0Q_0))^2} + (d^z_{\mathrm{ds},0})^2}\,. \tag{3.1}$$

with the cantilever properties k_0 ,f_0, Q_0 and the system noise floor $d^z_{\mathrm{ds},0}$ that is white noise in the vicinity of the cantilever resonance. The noise floor is determined by averaging the spectral density in a suitable region around the resonance and fitting equation 3.1 to the measured spectrum with the cantilever properties as fitting parameters [79]. These measurements are performed for the Omicron NC-AFM system for different $\sum$-signals and different positions of the laser spot on the cantilever. In a first measurement series the noise floor was determined for $\sum$-signals of 2 V, 4 V, 6 V, 8 V and 10 V. For that, the laser spot is first positioned at the position on the cantilever where the maximum $\sum$-signal is

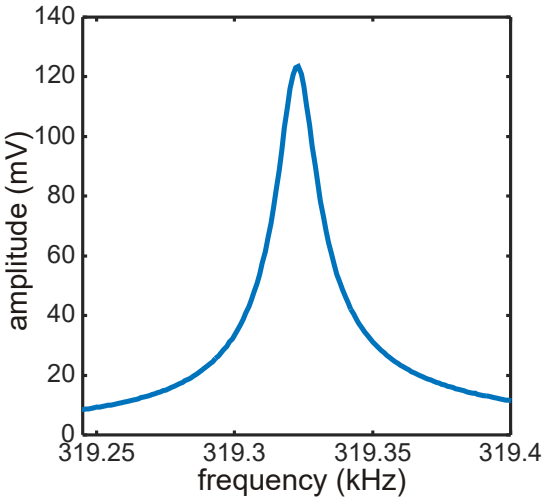

Fig. 3.8: Amplitude response as a function of the frequency for a cantilever exited at its resonance frequency with a Q-factor of 21800.

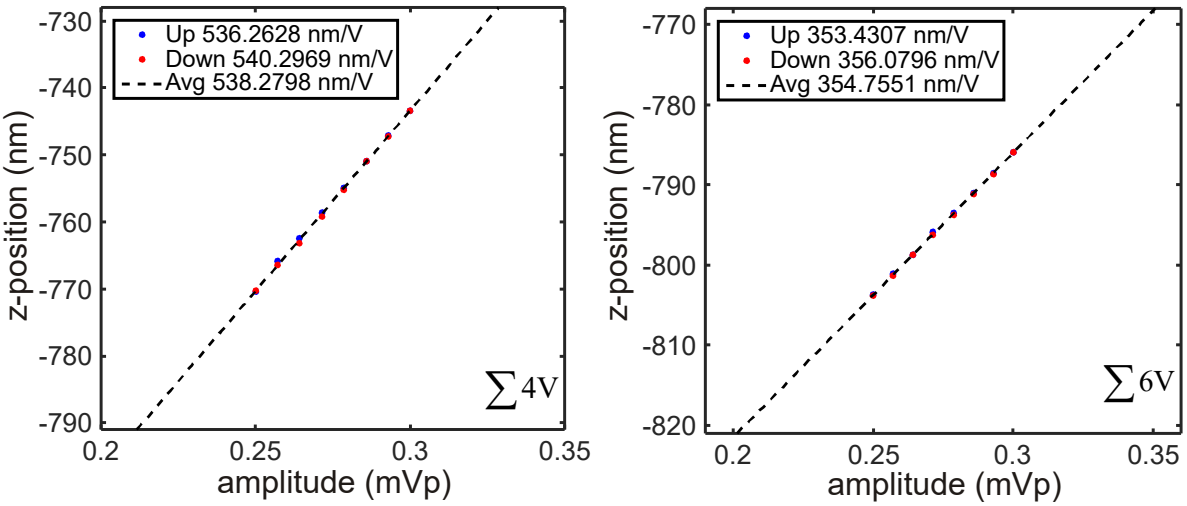

Fig. 3.9: Amplitude calibration for two different sum signals (4 V and 6 V). The amplitude is anti-proportional to the $\sum$-signal.

achieved, which is by experience the middle of the cantilever as observed with a camera. Then, the laser spot is moved towards the free cantilever end until the $\sum$-signal is decreased to approximately half of the maximum value. The different $\sum$-signals then are achieved by increasing the laser power input to appropriate values. The thermal excited eigenmode of the cantilever is recorded with a spectrum analyzer (HF2LI Lock-in Amplifier Zurich Instruments, Switzerland) with adjusted filter bandwidth for noise (200 Hz) and cantilever stiffness (20 Hz) determination (see figure 3.10).

For the analysis of the measured spectrum, the sensitivity factor relating the amplitude of the mechanical cantilever oscillation to the measured oscillation voltage has to be determined for different $\sum$-signals. The calibration of the amplitude is automatically done with a Matlab script written by M. Temmen where details can be found in ref. [54]. The result of the amplitude calibration performed with this script for $\sum$- signals of 4 V and 6 V is presented in figure 3.9. Before the amplitude is calibrated 15-20 minutes are waited to minimize piezo creep. From the plots it can be revealed that the amplitude calibration is very accurate as the fitting for up and downward directions differs by less than 1%. However, the amplitude calibration is repeated several times and the average value is determined. The amplitude calibration is proportional to the $\sum$- signal for equal laser spot positions on the cantilever.

An example for the determination of the noise floor is shown in figure 3.10. The left plot shows the thermal peak for a $\sum$ of 6 V and bandwidth a of 200 Hz where the averaged spectral noise density is shown as function of the frequency. This measurement is used to fit the noise floor. The right plot shows the detailed thermal peak for a $\sum$ of 6 V and a smaller bandwidth of 20 Hz and is used for fitting the parameters Q_0 , k_0 and f_0.

The results for the complete series are listed in table 3.2 . The averaged noise spectral density decreases with increasing $\sum$. For a low $\sum$ of 2 V the noise floor is at 188 fm/$\sqrt{\text{Hz}}$

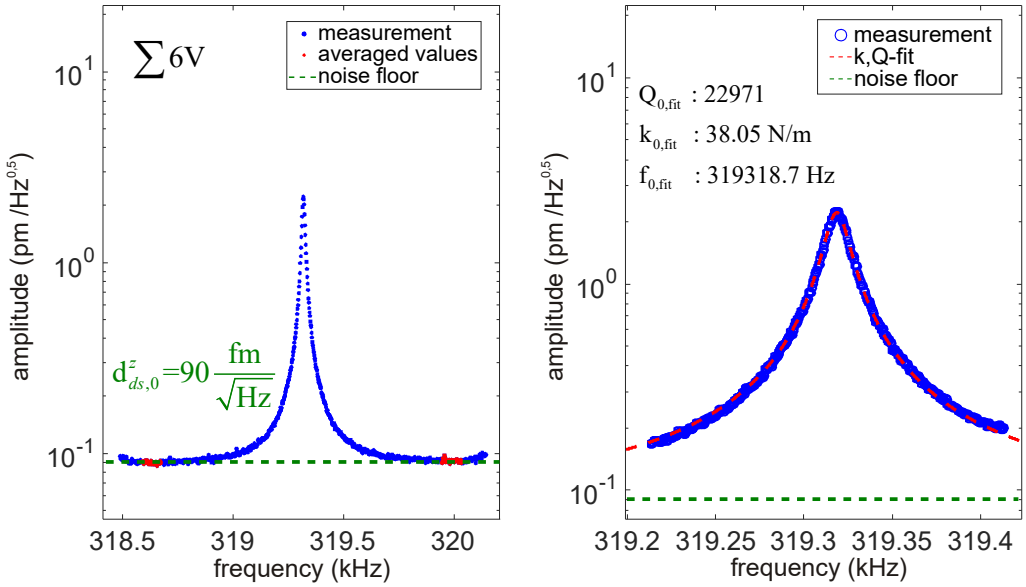

Fig. 3.10: Determination of the deflection noise density and the cantilever stiffness (k) with the thermal excitation method [52, 79].

and decreases to 79 fm/$\sqrt{\text{Hz}}$ and 69 fm/$\sqrt{\text{Hz}}$ at a $\sum$ of 8 V and 10 V. The predominant noise in the OBD detection scheme is shot noise of the photodetector [76] which is proportional to the factor $\sqrt{1/\text{P}}$ with P being the light power which is proportional to $\sum$. The overall deflection noise density $d^z_{ds,0}$ can be expressed by:

$$d^z_{ds,0} = m \cdot \sqrt{\frac{1}{P}} \tag{3.2}$$

where m is a constant including different properties of the cantilever and the photodetector [76]. In figure 3.11 the deflection noise density is shown as a function of $\sum$ with a fit of equation 3.2 to the measured data. From the fit, it can be revealed that the noise floor strongly increases for low light powers and one should at least have a $\sum$ of 4 V to obtain a low noise floor. For $\sum$ higher than 10 V the fit predicts only small improvements in the noise floor.

$\sum$ (V)	$d^z_{ds,0}$ $\left(\frac{\text{fm}}{\sqrt{\text{Hz}}}\right)$	f_0 (Hz)	Q_0	k_0 $\left(\frac{\text{N}}{\text{m}}\right)$
2	188	319325	22905	35.87
4	120	319322	22878	36.09
6	90	319319	22971	38.05
8	79	319315	22569	36.06
10	69	319314	23166	38.76
8*	117	319321	22559	26.71
4**	121	319323	23192	37.67

Tab. 3.2: Spectral noise density of the modified set up for different $\sum$-signals and fitted cantilever properties for a laser spot position close to the free cantilever end. *laser spot positioned in the middle of the cantilever, ** laser spot positioned as far as possible at the free cantilever end.

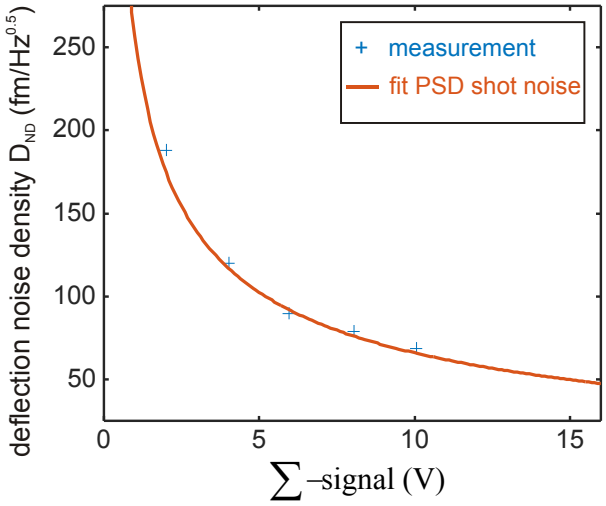

Fig. 3.11: Deflection noise density as a function of the ∑-signal (laser power).

A comparison of the spectral noise density of the original set up, after the first modification and after the new changes in the set up is given in table 3.3.

With the original LED only a lower ∑ of 3.2 V could be achieved why the noise floor after the first and the second improvement is compared at ∑ = 6 V. The exchange of the photodiode and the new pre-amplifier have decreased the noise floor about 3 times compared to the first improvement and more than 30 times compared to the original set up. Higher ∑ values yield an excellent noise floor below 100 fm/$\sqrt{\text{Hz}}$.
The fitted cantilever properties are also shown in table 3.2 which show all calculated values in the same range which is a verification of a correct fit. The measured cantilever has a quality factor of approx. Q_0=22800±300 at its resonance frequency of the fundamental mode of f_0=319320 kHz and a stiffness of k_0=37±1,5 N/m. The stiffness is in the range expected for this type of cantilever (manufacturer specifications 42 N/m).
However in table 3.2 two additional measurements of the noise floor at different laser spot positions on the cantilever are listed. For one measurement (4**) the laser spot position from the previous measurement is changed in a way that ∑ decreases to half the value (here from 8 V to 4 V). This is the case when the spot is at the absolute free end of the cantilever and already not completely on the cantilever anymore. The noise floor increases from 79 fm/$\sqrt{\text{Hz}}$ to 121 fm/$\sqrt{\text{Hz}}$ whereby it can be concluded that this laser spot position is less suitable for measurements. The data for (8*) is recorded for a laser spot position starting at a ∑ of 4 V from the position of the previous measurement and going to the fixed cantilever end until the ∑ increase to 8 V which is usually in the middle of the cantilever as observed by camera. Interestingly this procedure has only minor impact on the noise floor that is at 117 fm/$\sqrt{\text{Hz}}$ just as at the starting position with 4 V (120 fm/$\sqrt{\text{Hz}}$) but the calculated stiffness of the cantilever is much lower. The

Tab. 3.3: Spectral noise density of the original setup and after the two modifications. Measured at ∑=3,2 V (original) and 6 V. Values taken from [76]

setup	$d^z_{ds,0}$ $\left(\frac{\text{fm}}{\sqrt{\text{Hz}}}\right)$
original	2757
first improvement	272
second improvement	90

stiffness is fitted as 26.71 N/m which is 25-31 % lower than the stiffness fitted at the front positions. To exclude an error in the data the measurement is repeated with the same result. As we have no explanation for the change in the measured cantilever stiffness we decided to prefer laser spot positions near the free cantilever end.

In conclusion the best position for the laser spot is already used in the measurement shown in figure 3.10.

3.5 Scan controller system

The heart of every NC-AFM system is the SPM electronics which is responsible for the control of the complete AFM system and the image recording. During this work different scan controller systems have been used.
When starting the work demodulation of the NC-AFM signal was first realized with a Nanosurf easyPLL Digital FM Detector and Sensor Controller (Nanosurf, Switzerland) used together with a Dulcinea Scan Controller unit (Nanotec Electronica S.l., Spain). The easyPLL was meanwhile replaced with the integrated PLL in the HF2 Lock-In spectrum analyzer (Zuerich Instruments, Switzerland). Inasmuch the Dulcinea control system did not work satisfactory it was replaced by the RHK SPM 1000 Control system (RHK Technology, Inc., USA). This system comes with its own excellently working PLL (RHK PLLPro2) and the RHK PMC 100 piezo controller for the scan head coarse motion. With this configuration, most of the AFM images shown in this work were measured.

Fig. 3.12: The photograph shows the two RHK scan controller systems, namely the SPM 1000 with the PllPro2 and the R9. The most obvious difference between the two systems is that the R9 does not have analog potentiometers for adjusting scan parameters. One example is the z-feedback which in the SPM 1000 consist of two potentiometer (gain and time constant) and is now integrated in the software, allowing a more precise adjustment.

Finally the successor RHK system R9 replaced the SPM 1000 and also the PLLPro2. In figure 3.12, photos of the RHK PLL Pro 2, SPM 1000 and the R9 scan controller are shown. While the SPM 1000 still had several analog knobs for scan parameter adjusting all of these features are digitally integrated in the R9 and can be adjusted by the scan control software. This minimizes noise sources and due to several additional features the R9 is a superior system.
For the connection of the RHK scan controllers with the Omicron AFM system, some cable connections had to be reconfigured and were built by in the in-house electronics workshop.

3.6 Preparation of samples

The ceria samples (see section 4.3) studied in this work were always stored under clean and dry ambient conditions. However the extended storage of the samples leads to a non-negligible contamination of the sample surfaces with particles and residual gas from the atmosphere. Already the presence of only one monolayer of contaminants on a sample surface is enough to prohibit atomic resolution in a NC-AFM measurement. Hence, a careful sample preparation is necessary after the samples are transferred into the UHV chamber. For that a special versatile system for the sample preparation was integrated into the chamber by Pieper et al. [74]. This system uses the sample holder design schematically shown in figure 3.13. On a base plate a sample and thermocouple are fixed on an embeded recess on a Marcor® block. Two tantalum braces attached on the Marcor plate hold the sample which is wrapped up in a tantalum foil. The tantalum braces are fixed with four molybdenum screws and a connection to the base plate is established. The sample holder is placed in a specially designed preparation adaptor where the tantalum brace is used as an electrical sliding contact and the tantalum foil as a conductor for resistive heating. The temperature of the sample surface is estimated from a measurement of the temperature from the embed thermocouple with an accuracy of ±20 K for high temperatures. The thermocouple is placed under a thin ceramic plate that is placed under the sample. A description of the calibration procedure and more details can be found in ref. [74]. One advantage of this sample holder design is the very local distribution of heat while the sample is heated to temperatures up to 1200 K, the base plate is nearly at ambient temperature during annealing cycles. In this way high annealing temperatures above 1000 K are achieved for an electrical power in the range of 8 to 9 W.

Controlling the sample annealing is realized with a power supply, complemented with a temperature controller (Omron E5CN, Omron Electronics GmbH, 40764 Langenfeld, Germany). With a homemade Matlab script, the temperature controller is operated over a simple graphical user interface [54] which allows to choose a set point for the maximum

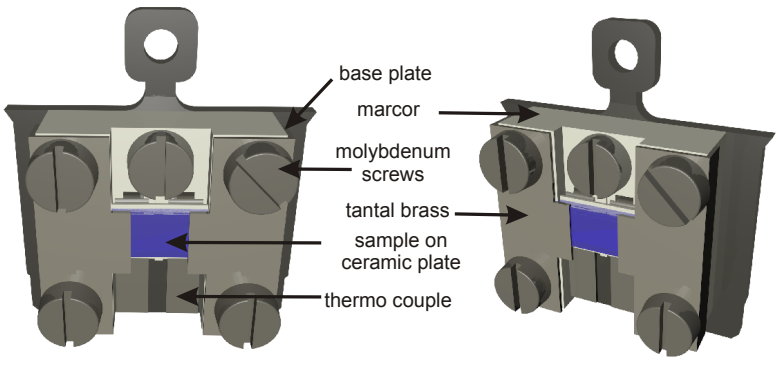

Fig. 3.13: 3D model of the sample holder. The sample holder consists of a ceramic plate (Marcor®) fixed on the base plate with a embeded recess for a thermocouple and the sample. The sample is wraped in tantalum foil and held in place by two tantalum braces fixed with four molybdenum screws.

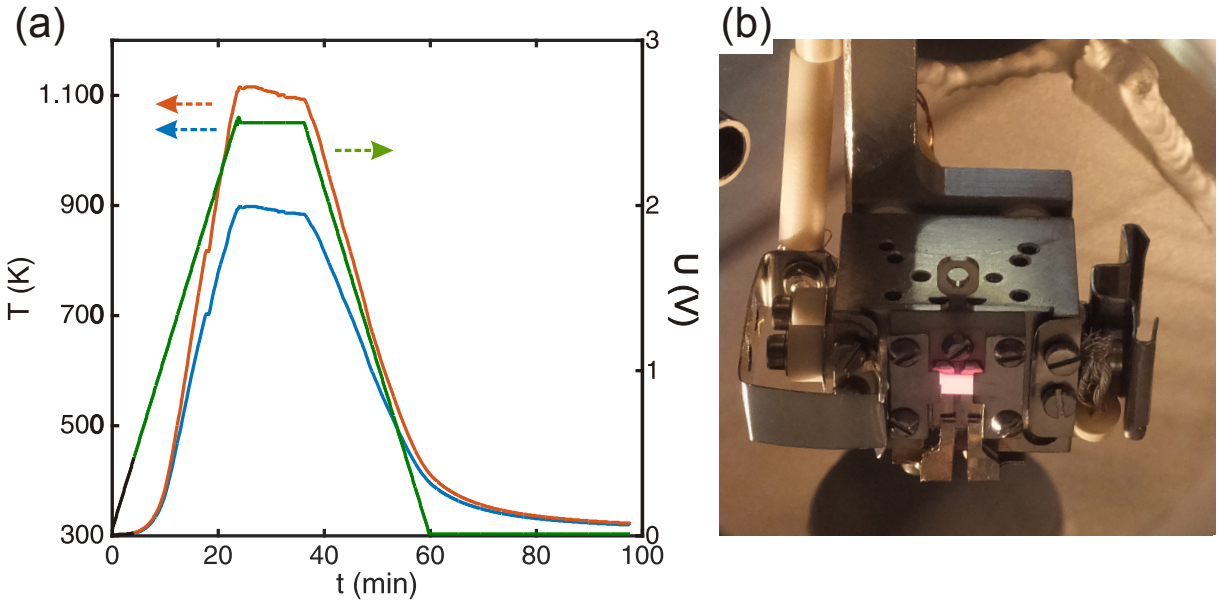

Fig. 3.14: (a) The plot shows a typical annealing cycle with the temperature ramped by the Omron controller. The green curve shows the voltage increase from 0 V to a set point of 2,6 V which is held on for 20 min. The blue curve shows the measured temperature at the embed thermocouple and the orange curve shows the estimated temperature on the sample surface. From the plot it can be seen that the temperature follows changes in the voltage closely. The cool down cycle takes much longer as the sample surface temperature decreases very slowly. (b) Photograph showing a ceria film sample during annealing at high temperature.

voltage, the initial voltage in- and decrease rate, the set point for the temperature and the time for holding the specified values. During the annealing cycle, voltage and temperature are recorded automatically.

A usual annealing cycle is shown in figure 3.14 (a). The voltage is increased at a rate of 0.1 V/min leading to a temperature increase rate of approx. 30 K/min. The set point temperature is held for a specified time (typically 20 to 40 min) and then the sample is cooled in the same manner. Room temperature is usually reached 1.5 hours after starting the cool down. A photo of the sample during annealing at high temperature is presented in figure 3.14 (b). The glowing surface is a ceria film sample at approx. 1060 K.
Some sample holders used for single crystal samples are not equipped with a thermocouple. In this cases, the temperature is measured by a pyrometer. While the pyrometer obtains a good accuracy for our crystal samples it fails on our ceria film samples as the Si support of the films leads to adulterated thermal radiation.

The sample is prepared in repetitive cycles of annealing and sputtering the sample surface with argon ions. For that, argon is let in the chamber until a pressure of $5 \cdot 10^{-5}$ mbar is reached. In the sputter gun, argon atoms are ionized and accelerated onto the sample surface by applying a voltage of 1.5 kV. The sputter time is 5 minutes. The surface sputtering is always done as the first preparation step as it is very effective against persistent contaminants and can also remove carbon, fluorine and silicon impurities.

Not only the sample surface but also the probes are sputtered before they are used in the NC-AFM. This is done as the cantilevers are stored under ambient conditions where oxide layers contaminate the probes which is removed by sputtering. For the sputtering of probes we use the same parameters as for the samples but the voltage is decreased to 0.5 kV to prevent excessive tip damage.

Most of the samples were prepared under UHV conditions. For one measurement series, ceria film samples were prepared under ambient conditions and in UHV in a controlled oxygen atmosphere. These measurements have been performed by Dr. C. Barth in Marseille (CINAM institute, CNRS, Aix-Marseille University, France). A description of the corresponding sample preparation is given in section 5.2.2.

4 Properties of cerium oxide

This chapter is divided in two sections. In the first section, basics of cerium oxide (111) surfaces are summed up. In the second section, the different samples namely the ceria crystals and the thick ceria film used for the measurements are described.

4.1 Basic topology of CeO_2 (111)

Cerium (Ce) is found in the periodic table at the first position in the period of the rare earth elements with element number 58. Combined with oxygen, ceria (CeO_2) is formed crystalizing in the fluorite type structure (face-centered cubic, f.c.c.). Ceria is memento of the space group $Fm\bar{3}m$ where the sublattice of oxygen (O^{2-}) anions is cubic primitive and the Ce^{4+} cations form a close packed lattice [12]. The Ce^{4+}-ions are surrounded by 8 cubical arranged O^{2-}-ions, while the O^{2-}-ions are surrounded in a tetrahedral manner by 4 Ce^{4+}-ions. The ionic structure of ceria is shown in figure 4.1 (a). The lattice constant a of ceria is approximately 541±5 pm as measured by experiments

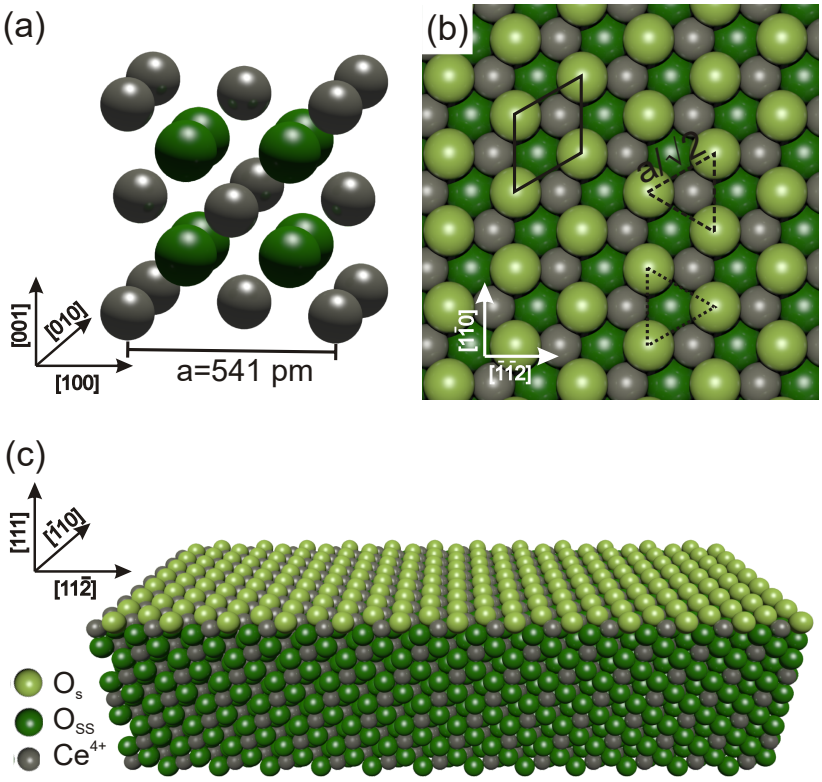

Fig. 4.1: Models of CeO_2. (a) Cubic lattice of CeO_2 consisting of O^{2-} anions and Ce^{4+} cations. The lattice constant a is 541 pm. (b) Top view on the CeO_2 (111). The surface unit cell is marked with the solid black rhombus. Triangular oxygen anion hollow sites and triangular cerium cation hollow sites are highlighted with the dotted and dashed triangles pointing in opposite directions. (c) Perspective view on the ceria surface revealing the (111) and ($\bar{1}$10) surface.

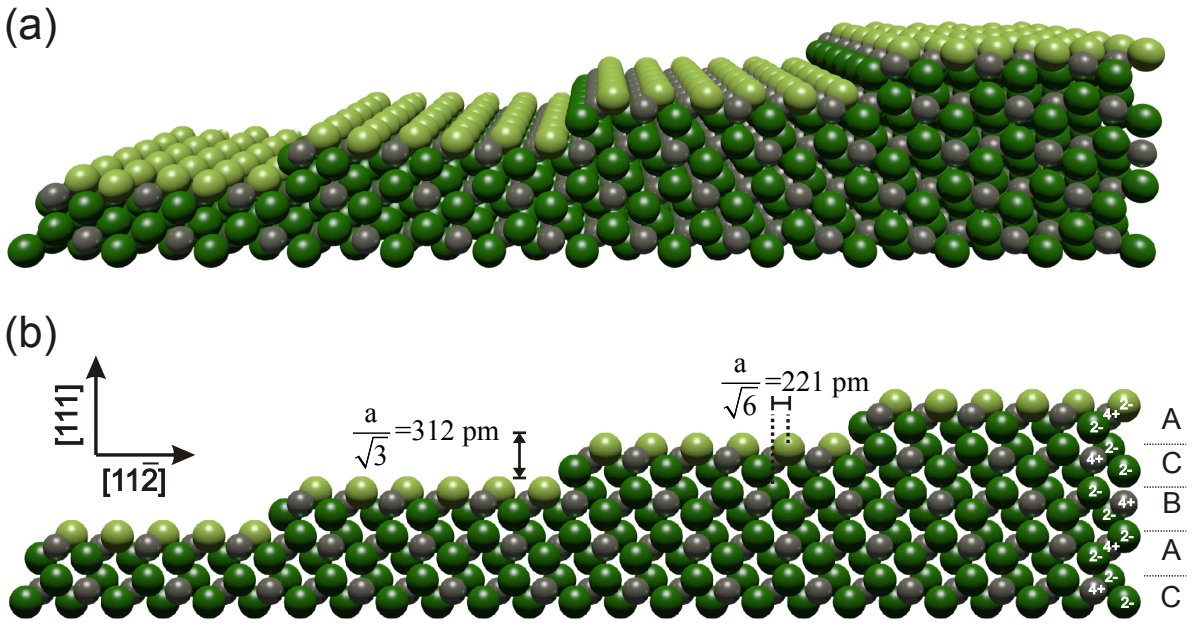

Fig. 4.2: (a) Perspective view of CeO_2 (111). (b) side view of CeO_2 (111). Ceria is built of triple-layers (TL) consisting of O-Ce-O atoms along the [111] direction. Highlighted are one TL height step edges, the type 2 classification according to the Tasker classification [81] (- ++ -) and the A-B-C stacking along the [111] direction. The step edges with $\langle\overline{1}\overline{1}2\rangle$ normal vectors expose a (110) nano-facet [82].

and calculated by theory [12,80]. The most stable surface of a fluorite crystal is the (111) plane which has the lowest surface energy. It is commonly assumed that the (111) top surface layer is formed by oxygen atoms. The top view of the (111) ceria surface is shown in 4.1 (b) and a perspective view is presented in (c). The crystallographic directions inserted in the model along the ordinates point at $[\overline{1}\overline{1}2]$ and $[1\overline{1}0]$ directions and are parallel to the edges of the used ceria film samples in this work. The top oxygen layer on the (111) surface is hexagonally arranged and forms a surface unit cell with a side length of $a/\sqrt{2} = 382\,\text{pm}$. From the model it is easy to reveal that the ceria (111) surface has a threefold symmetry. This symmetry leads to two different triangular hollow sites with a cerium cation or an oxygen anion in the first cerium layer or the subsurface oxygen layer which are rotated by 180° with respect to each other as highlighted in figure 4.1 (b). These triangular hollow sites are important for understanding absorption for instance, of water or hydroxyls on the ceria surface as discussed in subsection 5.2.5. Due to the lattice configuration along the $[\overline{1}\overline{1}2]$ direction, when walking over the surface, first a top oxygen is passed, then the cerium and the subsurface oxygen atom.

Along the [111] direction, ceria is built of anion-cation-anion triple-layers (TL) consisting of O-Ce-O atoms. The sublayers of the TL are charged (O^{2-} and Ce^{4+}) but the complete triple layer is electrically neutral. According to the Tasker classification [81], the (111) plane is a nonpolar type 2 surface which has no dipole moment perpendicular to the surface. This is illustrated in figure 4.2 where (a) shows a perspective view of the ceria surface with some one Tl height step edges and (b) shows the corresponding side view. The TLs have a height of $a/\sqrt{3}$ which is approximately 312 pm, however on a ceria surface,

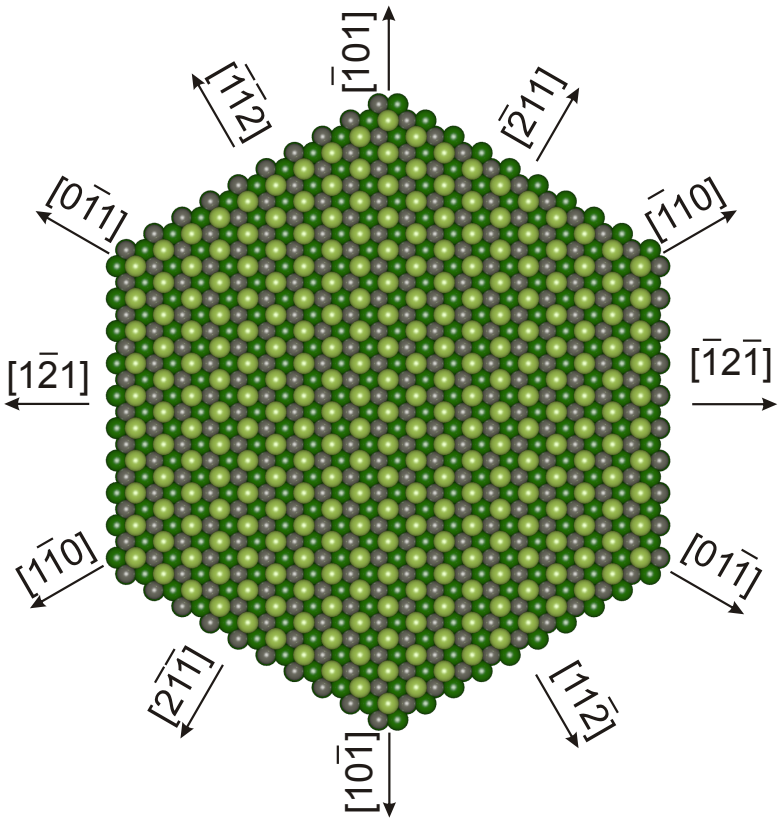

Fig. 4.3: The hexagon shows the ceria (111) surface with all basic crystallographic directions. The arrangement O_s-Ce-O_{ss}. repeats for [$\bar{1}$2$\bar{1}$], [$\bar{1}\bar{1}$2] [2$\bar{1}\bar{1}$] directions while the arragement for [1$\bar{2}$1], [11$\bar{2}$] and [$\bar{2}$11] is O_s-O_{ss}-Ce.

also several TL height step edges are not uncommon. The cations exhibit a stacking of the form A-B-C along the [111] direction as highlighted in figure 4.2 (b). In the [$\bar{1}\bar{1}$2] direction, each TL is shifted $a/\sqrt{6}$ compared to the underlying TLs.

In figure 4.3, the ceria (111) surface is shown with a hexagonal shape in order to identify all basic crystallographic directions on the (111) surface. From the figure it is easy to reveal that equivalent crystallographic directions repeat every 120°. The precise knowledge of the crystallographic directions is important for the interpretation of contrast in NC-AFM images. Hence, knowing if the atomic order along one surface direction (e.g., along [1$\bar{2}$1]) is $O_{surface}$-$O_{subsurface}$-Ce (O_s-O_{ss}-Ce) or O_s-Ce-O_{ss} can be crucial.

For the step edges, two orientations are commonly observed on the ceria (111) surface [83]. A step edge with a (110) nano-facet and a step edge with a (001) nano-facet. While (110) nano-facets can be found along $\langle 1\bar{2}1\rangle$ directions, (001) nano-facets are observed along $\langle 1\bar{1}\bar{1}\rangle$ directions. (110) step consists of an atomic order (O_s-Ce-O_{ss}) at the step edge as visible in the side view shown in figure 4.4 (b). A (001) step edge is shown in fig. 4.4 (a). In contrast to (110) step edges the composition of (001) step edges is not so distinct. The step edge in figure 4.4 (a) consists of an atomic order (O_s-Ce) at the step edge and the following O_{ss} is missing but a (001) step edge with an additional O_{ss} or even with a missing Ce is conceivable too. These different step edges are well known from observation on CaF_2 with NC-AFM [84] where a classification of these step edges in type I (110) and type II (001) is done and theses step edges can clearly be distinguished in KPFM images due to their different local surface potential [84]. Although, the surface

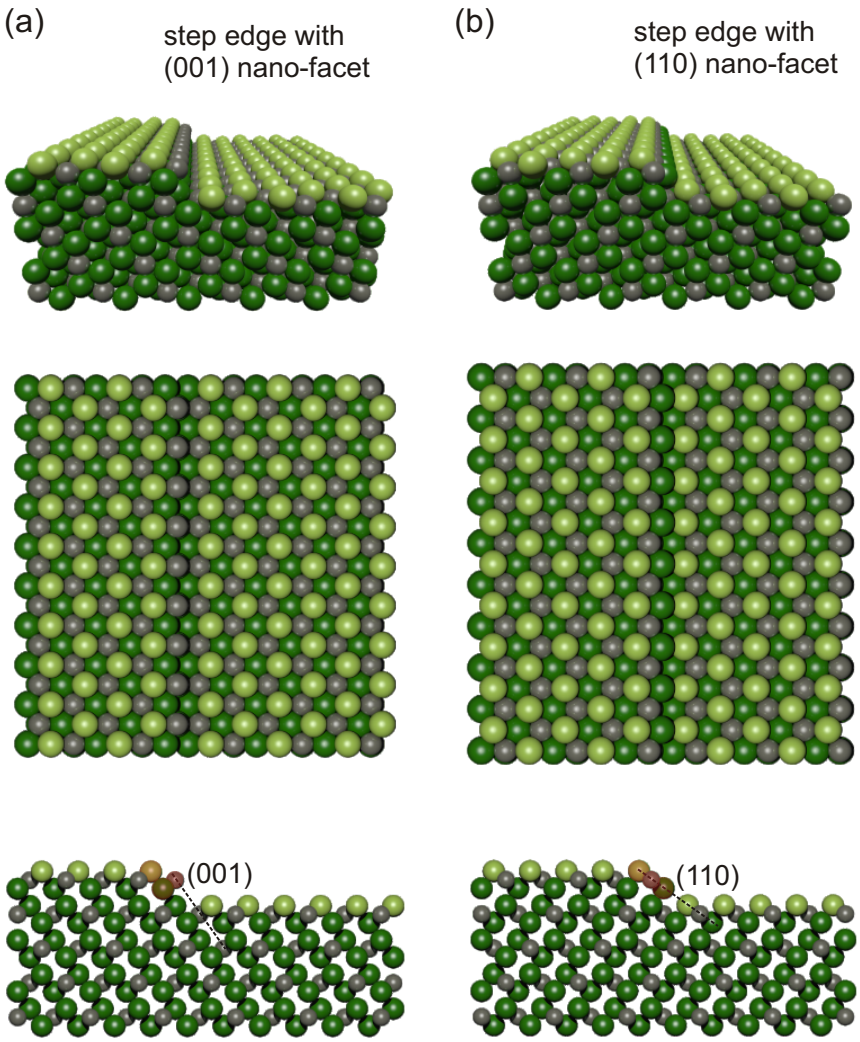

Fig. 4.4: (a) Step edge with a (001) nano-facet. The atomic sequence at the step edge is O_s-Ce with a missing O_{ss} (shaded red). This type of step is suggested in [83]. However for the (001) nano-facet also a step with an additional O_{ss} or without the cerium cation is conceivable. (b) Step edge with (110) nano-facet This kind of step is equivalent to the one shown in figure 4.2.

potential differences for step edges on ceria are not so pronounced we assume that the basic principle is similar [18,84]. Details on theoretical calculations on different step edge types on ceria nano-islands can be found in [85].

4.2 Reduction of CeO_2

So far, only the structure of CeO_2 has been described but one of the key features of ceria is its reduction possibilities. Starting from fully oxidized CeO_2, ceria can be reduced by annealing in UHV at conditions of very low oxygen partial pressures or by reducing agents like hydrogen or CO [86,87] to the fully reduced state of Ce_2O_3. During the reduction process, intermediated phases are passed through whereby some of them form unique stoichiometries and a stable structure where ordered oxygen vacancies play a crucial rule. The reduction reaction for forming CeO_{2-x} can be described in a formal

way by the Kröger Vink notation [3]:

$$2\mathrm{Ce}_{\mathrm{Ce}} + \mathrm{O}_{\mathrm{O}} \rightarrow \mathrm{V}_{\mathrm{O}}^{\bullet\bullet} + 2\mathrm{Ce}_{\mathrm{Ce}}^{\prime} + \frac{1}{2}\mathrm{O}_2 \tag{4.1}$$

The subscripts describe lattice positions, the superscripts $\bullet$ and $'$ stand for a positive or negativ charge. For single crystalline materials, different phases of ceria were identified by neutron diffraction [88] and a detailed phase diagram was derived from results of by thermodynamic modelling [89]. For example, ceria stoichiometries of Ce_7O_{12}, Ce_9O_{16}, $Ce_{19}O_{34}$, $Ce_{40}O_{72}$, $Ce_{62}O_{112}$, $Ce_{11}O_{20}$ have been reported for molar fractions of oxygen ranging from 0.63 to 0.65 and a temperature in the range of 600 to 1000 K. Although, other theoretical and experimental studies [87,90–94] have revealed several stoichiometries and made suggestions for surface structures of reduced ceria phases, the direct imaging of the surface structure with scanning probe techniques is a challenging task. So far STM measurements at low temperatures on very thin ceria films on Cu(111), Ru(001) and Pt(111) supports provided insight in the surface structure of reduced ceria phases [86, 95–99]. STM measurements are always performed on films with only a few to less than one monolayer thickness. The interpretation of the contrast of STM images on ceria is difficult as the metallic substrate may influence the atomic and electronic structure of the thin ceria overlayer and influences the STM contrast.

However, for investigating the surface structure of ceria and other oxides NC-AFM is predestined as the surface is directly imaged and not a composition of interactions between the substrate and ceria film, as has been pointed out in the literature [100]. In this work, the possibilities of direct surface structure investigations by NC-AFM is discussed in section 5.2.4 where the focus is on reduced ceria phases.

Beside the ordered surface vacancies observed for the reduced ceria phases, more or less disordered surface vacancies are observed. Several surface studies on ceria crystals reveal that the surface shows different amount of oxygen vacancies when the samples are annealed under UHV conditions [101–105]. In a publication that gained great attention (Esch [106]) claimed that oxygen vacancies observed with STM are formed at the surface and build clusters of oxygen vacancy pairs, vacancy lines or vacancies forming triangular structures. Similar but less pronounced surface features interpreted in the same manner were also observed with STM on ultra-thin films [107]. This interpretation of vacancies has become a controversially discussion as it was shown that fluorine impurities are present in a non-negligible amount at the surface in ceria crystals from the same source [108]. Theoretical considerations suggest that these fluorine impurities could result in a false interpretation of the STM contrast as they would not be distinguishable from vacancies in STM measurements [109]. The bottom line of this argument is that the formation of fluorine surface clusters is energetically much more preferred than the formation of surface oxygen vacancy clusters. Furthermore, NC-AFM measurements on ceria did not reveal similar vacancy formations [83, 101–105, 108, 110]. Further considerations suggest a mechanism where water and hydrogen is decisively for the vacancy formation [111] and could explain special vacancy formation that otherwise would be unstable. Oxygen vacancies, water and hydroxyls influence the catalytic properties of ceria surfaces and have

been studied widely [112–117]. They also have to be considered for the conversion of acid gases in catalytic processes [16]. Vacancies can act for example as reactive sites for methanol [118]. Furthermore to a specific amount hydroxyls are always present on ceria surfaces and are involved as surface intermediate in catalytic processes.
Despite 20 years of intense research a complete understanding of ceria surface reduction has not been achieved.

In this work, the surface vacancies found on the thin ceria films are described in section 5.2.5. Measurements showing water/hydrogen adsorbates on the ceria surface are discussed and may provide insight in the process of oxygen vacancy formation.

4.3 Ceria samples

For the experiments presented in this work, three kinds of CeO_2 samples are used. While most of the measurements are performed on Si supported thin ceria films also some measurements are carried out on ceria crystals. Some of the crystals are old remainders that already were used in [65, 72, 119] and were delivered from a commercial source (Crystal Guru; Florida, USA) that does not exist anymore and some of the crystals are from a new alternative commercial source (Surfacenet GmbH; 48432 Rheine, Germany). The film samples used in this work are provided from two wafers and are all labeled as ceria "M1912" and "M1969", the old crystal sample is labeld as "ceria SCO" and the new crystals is labeled as "ceria SCN".

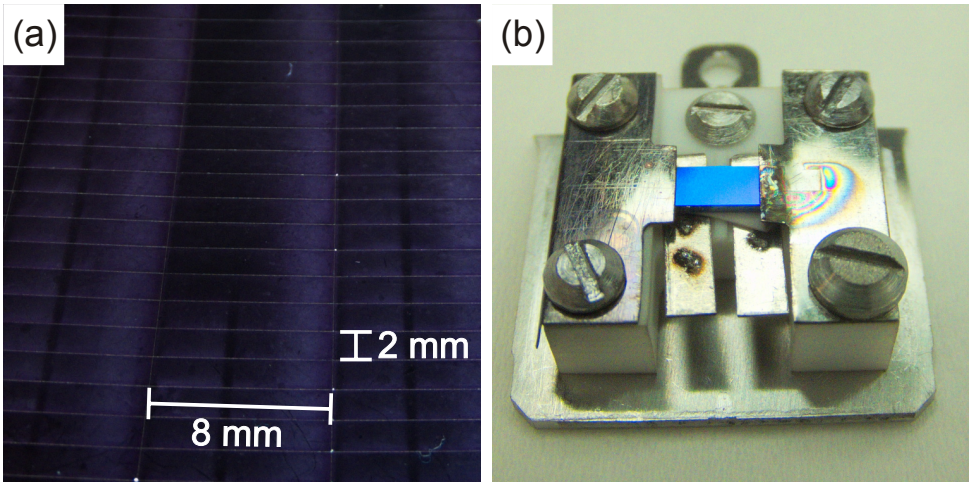

Fig. 4.5: (a) Photos of the ceria film M1969. The samples are cut out of a wafer into pieces of 8 mm in length and 2 mm in width. (b) Ceria film sample M1969 mounted in the sample holder. The effective measureable area is reduced by the molybdenum sheets to an area of $4 \times 2\,\mathrm{mm}^2$.

4.3.1 Ceria film samples

The films are produced by the IHP (Frankfurt Oder) in different thicknesses while the measurements shown in this work are all performed on films with a thickness of approximately 180 nm. The films are grown with molecular beam epitaxy (MBE) under an oxygen atmosphere (10^{-6} mbar) at a temperature of approximately 900 K. The Si(111) surface of a wafer is used as substrate for the films. For better film growth, an additional 3 nm thin praseodymium oxide layer is deposited on the Si(111) surface before the deposition of the ceria film as a buffer. Ceria films are grown with a cubic or hexagonal Pr_2O_3 buffer layer; in this work only films with a hexagonal buffer layer are used. A detailed description of the film growth and its characterization is given in [120]. A side view model of the ceria film is shown in figure 4.6 (a) revealing the cubic-hexagonal-cubic growth structure of the Si substrate - Pr_2O_3 buffer layer - ceria film.

From the growth of the ceria films only the surface orientation (111) is known and that the ceria film grows with type B stacking [120] and thereby with 180° rotation with respect to the Si substrate. For the interpretation of atomic contrast and different features in NC-AFM images, the precise knowledge of the crystallographic orientation is mandatory. For this purpose, a film sample is cleaved and the break edges are observed [65]. Si crystals are known for their good cleavage behavior along {111} planes. The break edges form surface angles with 109.47° and 70.53° with respect to the (111) surface corresponding to $(11\bar{1})$ and $(\bar{1}\bar{1}1)$ surfaces as shown in figure 4.6 (c). With the knowledge that the $\langle\bar{1}10\rangle$

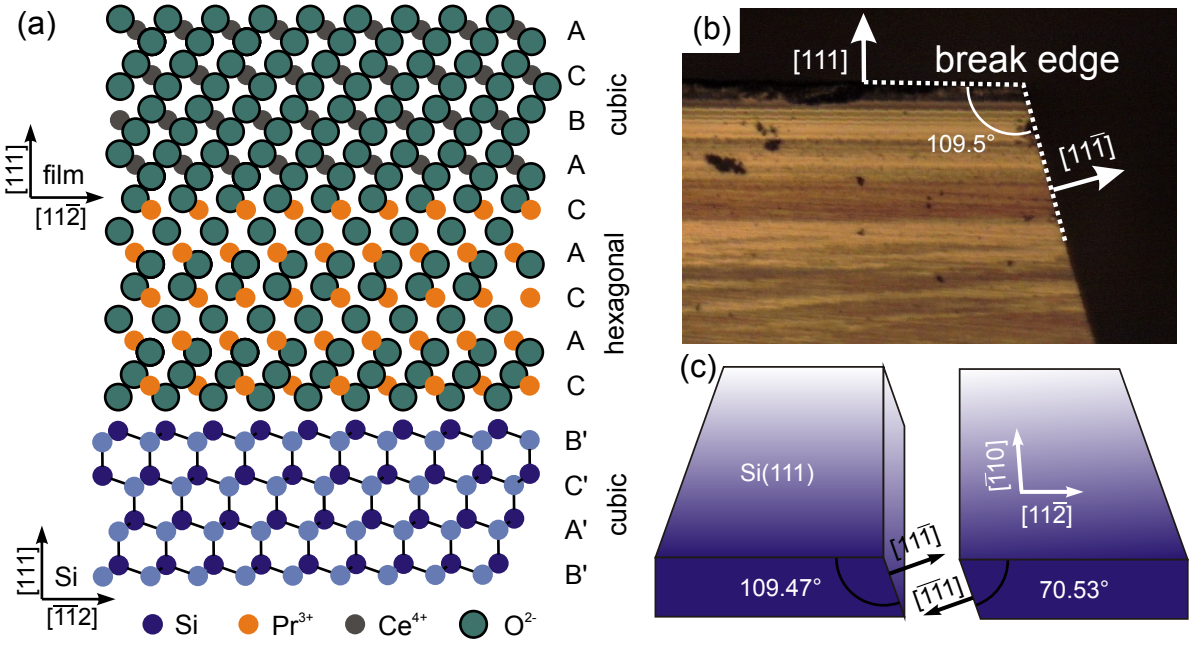

Fig. 4.6: (a) Cross-section of the cerium oxide film. The Si substrate and the ceria film have a cubic structure while the praseodymium buffer layer is hexagonal. The ceria film grows with type-B stacking on the Si substrate (rotated by 180°) which is not affected by the praseodymium buffer layer. (b) Microphotograph showing a cleaved ceria film sample. (c) Model for the determination of the crystallographic orientation from the cleavage of the film adapted from [65, 120].

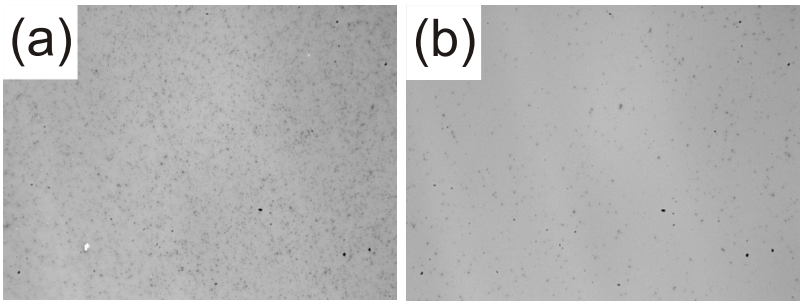

Fig. 4.7: (a) Microphotograph of the ceria film M1912 without preparation after three years storage. (b) Ceria film M1969 after two years storage. It clearly can be seen that the film surface M1969 is less contaminated with irregularities.

direction, lays on the (111) surface it is possible to determine the complete crystallographic orientation from the microphotograph shown in figure 4.6 (b). The viewing direction is along $[\bar{1}10]$ and the cleaved edge includes an angle of 109.5° to the surface whereby we identify it as $(\bar{1}11)$ surface. From this observation all other crystallographic directions can be revealed by simple vector analysis. This yields that the long side of our samples is parallel to $[11\bar{2}]$ and the short side to $[1\bar{1}0]$. To prevent the mix up of surface directions in AFM -images all samples are carefully attached with the same orientation to the sample holder.

A challenge for the use of wafer-size samples in SPM measurements is to obtain fragments in a size suitable for the holder. Simple procedures of cutting or cleaving the sample often result in a lot of fragments that are to small or odd shaped to be attached to the sample holder. To prevent this, the wafer with the ceria film is cut with a special saw at the IHP into plates of $2 \times 8\,\mathrm{mm}$ shown in figure 4.5 (a). The cut lines can clearly be seen in the photo. For attachment into the sample holder the cut samples are carefully taken with a clean tweezer out of the wafer. To remove small particles and dust that precipitated on the surface, clean nitrogen is blown over the samples before transferring them into the load lock.

However, most of the measurement on the films were performed on two wafers which were grown with one year difference. these samples have been used over a long time. Hence, it has to be checked if the long storage time has a negative impact on the film quality. In figure 4.7, microphotographs from the two ceria films are shown. Photo (a) shows the surface of the older ceria film M1912 and photo (b) of the newer film M1969 after three and two years storage time, respectively. A partially contamination with small particles on the surface of the film M1912 can clearly be seen . However, also the newer film M1969 shows a slight contamination.

With a confocal laser scanning microscope, a surface inspection with higher magnification is possible. In figure 4.8 (a) a photo of the microscope is presented and in (b) four images taken at different magnifications. It can clearly be seen that the contamination is only partially and most of the surface is rather clean. The largest particles on the surface have a size in the range of 2 to $3\,\mu$m. We speculate that such particles result from the cutting and pulling out of the samples from the wafer whereby a lot of crumbs are dispersed on the surface. From these observations we conclude that the contamination is not a result of film degradation and after the preparation in the UHV-chamber we have not found

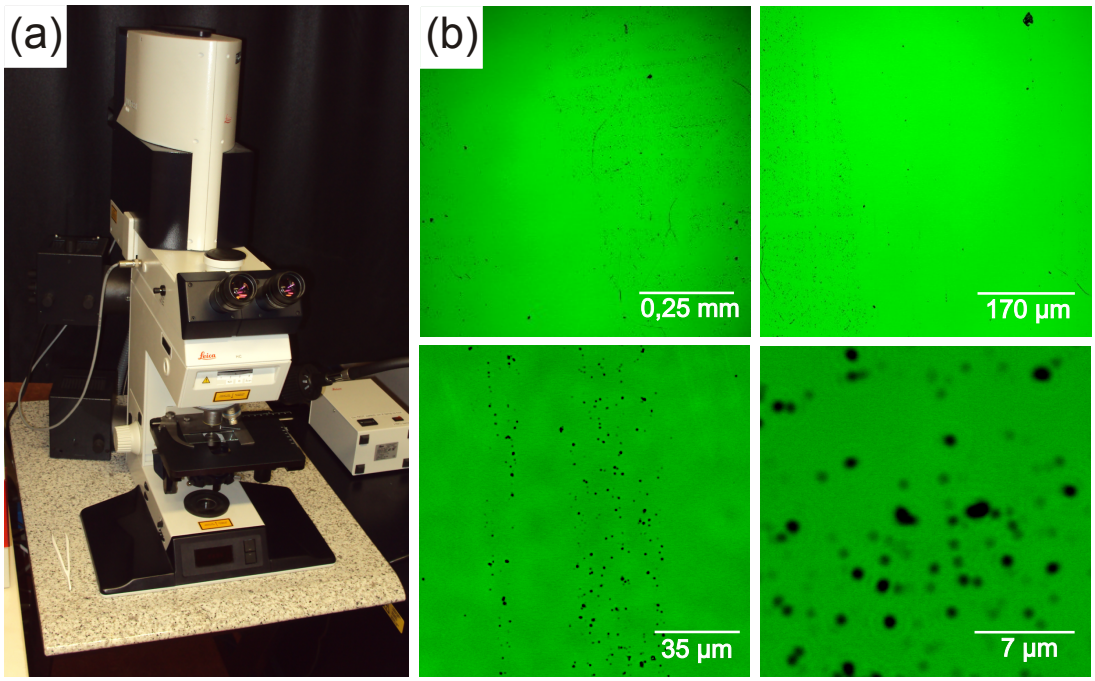

Fig. 4.8: (a) Confocal laser scanning microscope. (b) Images taken with the microscope show some contamination with very small particles on the unprepared ceria film M1969 surface after two years storage under ambient conditions.

any contaminants anymore. In conclusion, we can say that the ceria film can withstand a long storage time without significant loss in quality.

4.3.2 Ceria crystal samples

The production of large ceria single crystals is much more difficult and expensive than the relatively easy MBE film growth. Ceria crystals are produced with an induction skull melting process [121] which involves annealing temperatures in the range of 1500 to 2000 K and high temperature gradients in the melt of several hundred Kelvin over a distance of a few centimeters. The ceria powder is put in special buckets that are continuously water cooled from the outside and brought to its melting point for an extended time. After the melt is ready and cooled down the grown ceria crystals have to be broken out of the melt. This process is mostly done with a hammer whereby it is obvious that the whole procedure is much less clean than the UHV MBE grown films. The size of the grown crystals depends on the size of the special buckets used for the growing but due to the energy intensive melting procedure, the size is limited and the grown crystals have only a width in the range of 1 cm. For the use in NC-AFM, the pulled out crystals have to cleaned and polished causing additional expenses.

In this work, two older ceria crystals (Ceria SCO) have been used which were produced by a commercial source (Commercial Crystal Laboratories Naples, FL, USA), that is no longer active. A photo of this crystals attached to sample holders is shown in figure 4.9 (c). The crystals were attached to an older sample holder like the left one shown in

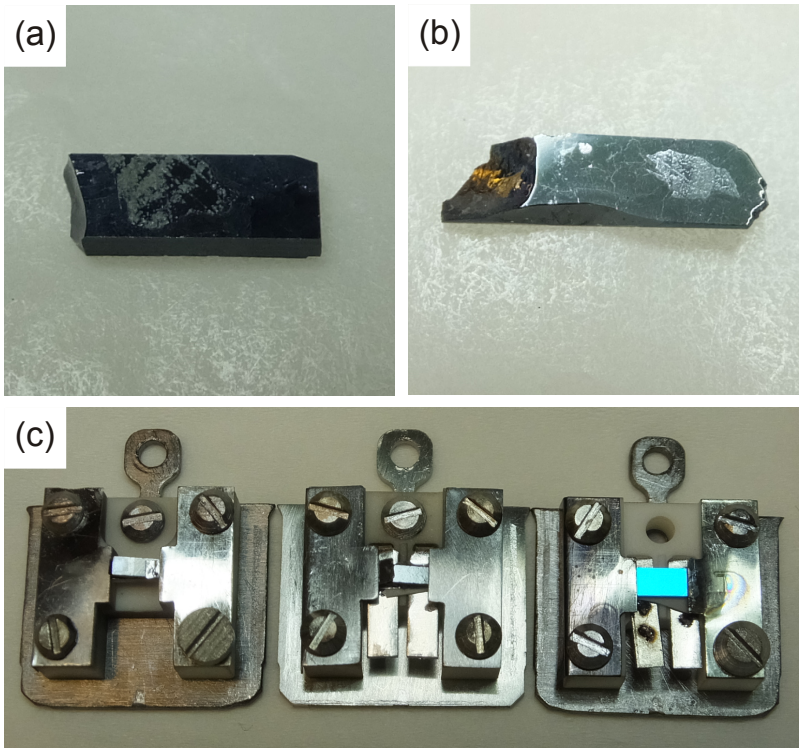

Fig. 4.9: (a) and (b) show two crystals from the commercial source (Surfacenet GmbH; Rheine, Germany).(c) The left and the middle attached samples are crystals from the commercial source (Crystal Guru, Florida, USA) compared with an attached ceria film sample. It can clearly be seen that the film sample is much larger in size. The left sample holder is an older version with no thermocouple and cannot be used anymore.

the photo. The position of the sample in this holder is too high and after an exchange of the push pull motion (PPM) in the AFM-stage, a sample approach was not possible anymore. Therefore old crystal samples were transferred to the new sample holder shown in the middle of the photo. Due to the extensive use of the old ceria crystals in the past, the samples have already gone through hundreds of preparation cycles consisting of annealing at high temperature and sputtering. As a result of this repetitive stress, only one of the remaining samples is still useable for measurements but also this sample is broken in the middle and the reattachment in the new sample holder is problematic. The photo in figure 4.9 (c) also reveals the different size of the old crystals compared to the ceria film samples which have a three times larger surface area compared to the crystals. In contrast to the film, only the (111) surface orientation of the crystal is known but not the crystallographic orientations of the edges.

The bad condition of the old crystals and the shutdown of the producing source led us look for an alternative source for ceria crystals. One commercial source is the Surfacenet GmbH (Rheine, Germany). Three ceria crystals from this source (ceria SCN) as a replacement for the old crystals were ordered for this work. Two of them are shown in figure 4.9 (a) and (b). From the optical appearance these crystals differ slightly from the old crystals. While the SCO crystals have a uniform black color, the SCN crystals are only partially equally colored but also have some inclusions with a brighter contrast. The size of the new crystals is approximately 6 to 8 $\times 2\,\mathrm{mm}^2$ and similar to the film samples but the crystals have about twice the thickness. However, a surface analysis is performed with an EasyScan 2 AFM in the contact mode. The topographic image is shown in figure 4.10 (b). The inclusions on the crystal surface have a very high roughness that already can be seen from the optical appearance, hence only the scan area highlighted in (a) with the dotted

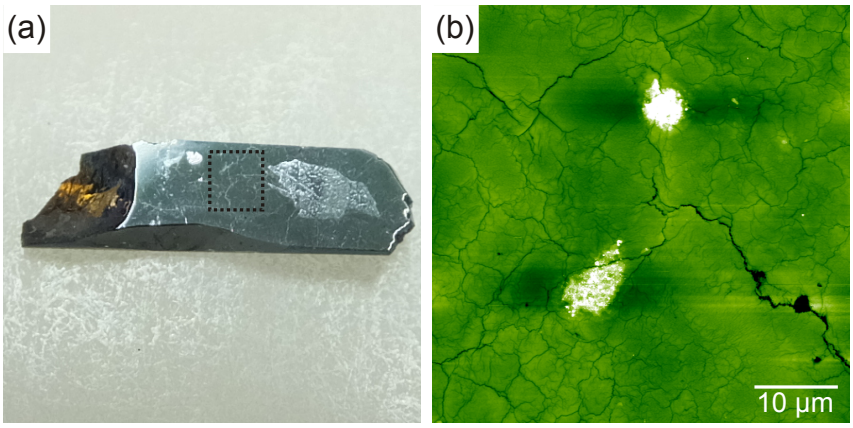

Fig. 4.10: (a) Photo of the new ceria crystal SCN. The area where the contact AFM measurements are performed is highlighted (b) Topographic AFM image revealing a plane surface but also a lot of small cracks. The AFM-image is recorded in the contact mode with an EasyScan 2 AFM.

lines is scanned. The AFM image reveals a relative plane surface with a RMS roughness of 9 nm whereby the particles that appear with the very bright contrast in the image are excluded from the RMS analysis as these particles are assigned to contaminations. Although, the surface roughness is very low, a careful look reveals that the surface is crossed by a lot of small cracks. Bigger cracks have a depth in the range of 80 to 200 nm but most of the cracks have a depth of 10 to 30 nm. Due to their small width, the cracks hardly influence the measured RMS roughness but can be critical for measurements with the NC-AFM as on small scanning ranges, strong height differences are most difficult to handle.
NC-AFM measurements performed on these crystals are described in chapter 5.2.6.

5 The morphology of Cerium oxide

In this chapter, the main results that were achieved during this thesis are presented and discussed.
First, the basic procedures and some typical difficulties for measuring on the ceria film are introduced. Than the morphology of the cerium oxide film is described and the surface changes related to annealing in ultra high vacuum. It is shown that the film reduces by annealing in UHV and can be fully oxidized by annealing in a controlled oxygen atmosphere. Also the preparation in ambient conditions is considered. Furthermore, common observed line defects found on the surface of film and bulk ceria with a short comparison to line defects found on CaF_2 crystals are discussed. As major result of this thesis, the reduction of the ceria surface exposed to UHV is analyzed in detail in a cooperative work. This is followed by a discussion about irregularities that we assign to water species.
The chapter is rounded up by a presentation of the surface morphology from the ceria bulk crystals. The differences of the surfaces and the experimental requirements of the bulk and film samples are compared.

5.1 Basic procedures for measuring on the ceria film samples

Our approach for achieving atomic resolution on the ceria film samples is based on a very careful increase of the frequency shift set point. Figure 5.1 shows a topographic image obtained on the ceria film surface representing the starting point of our

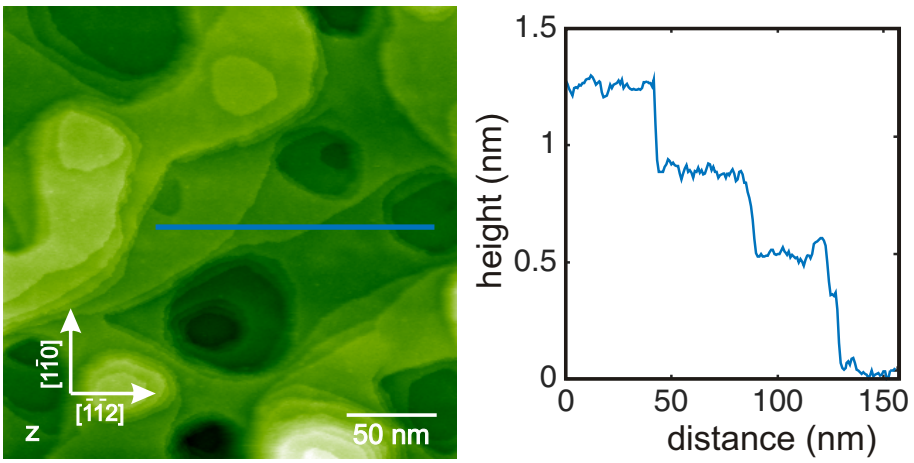

Fig. 5.1: Topographic image on the ceria film M1969 representing the starting point for high resolution measurements. The inserted profile shows the TL height of step edges.

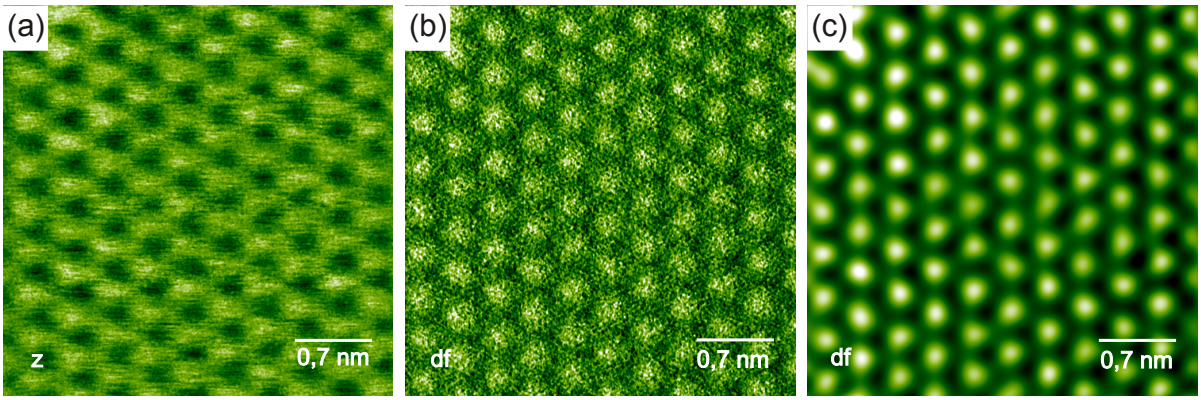

Fig. 5.2: (a) NC-AFM topographic image obtained on the ceria film M1969. (b) Corresponding frequency shift image. (c) The same image filtered with 2D-FFT to remove noise. The images represent the maximal scan area on the surface where no irregularities are observed.

higher resolution measurements. Usually, the measurement series starts with an image size of 250 nm × 250 nm whereas afterwards a flat terrace area on the recorded image is chosen for atomic resolution imaging. With the experience of a high amount of defects and water species observed on the surface and discussed in section 5.2.5, the scanning area should be very small. So far we could not achieve atomic resolution for scanning frames larger than 10 nm × 10 nm. For atomic resolution imaging the scan speed is set to 0,3 to 0,4 lines per second (one image with a resolution of 512 px × 512 px takes 5 to 7 minutes). In figure 5.2 one of the few images with atomic resolution revealing no defect is presented. The images show fully reduced Ce_2O_3 as discussed in subsection 5.2.4. Although, the positions of the atoms are resolved, the contrast in the topographic and frequency shift images is relative low due to a very moderate Δf set point. The FFT filtered image shows that the hexagonal lattice is very well visible and not distorted which is a result of low thermal drift during the measurement. Most of the images exhibiting atomic resolution on the film were recorded in the quasi constant height mode with a Δf set point of -7 Hz to -20 Hz depending on the tip quality. The set point is increased very slowly until atoms are faintly resolved. From this point, the Δf set point can only be increased in a very small range until the measurement becomes unstable and distorted

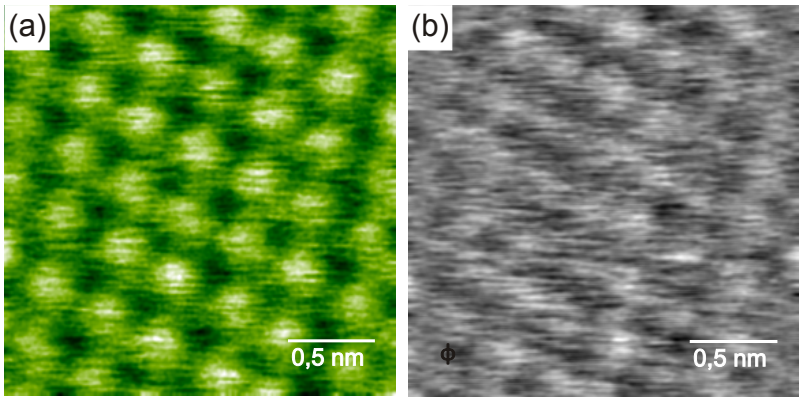

Fig. 5.3: (a) NC-AFM topographic image representing the so far best achieved atomic resolution on the ceria film M1969. The corresponding KPFM image reveals a weak atomic contrast.

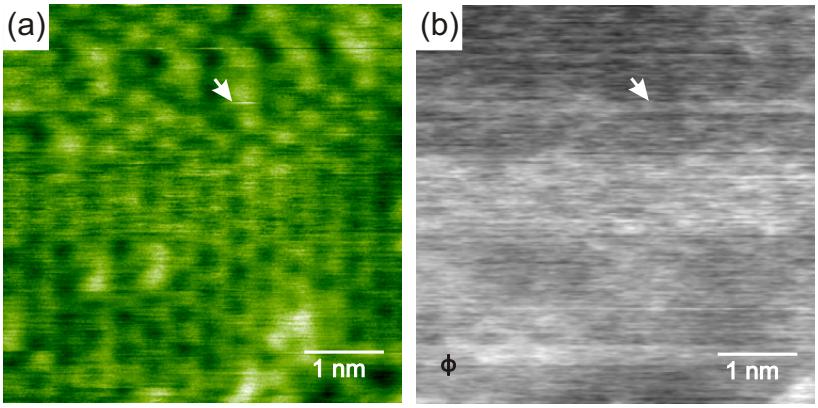

Fig. 5.4: (a) NC-AFM topographic image obtained on the ceria film M1969. (b) Corresponding KPFM image. Both images reveal significant changes in contrast during measuring probably due to a tip change (white arrow). The first lines of the image show the commonly observed contrast for the ceria lattice where the surface oxygen atoms appear as spots with a bright contrast. After the tip change the sub lattice is more present where spots with a dark contrast are dominant. The contrast change is accompanied by a local potential change of approx. 50 mV.

(see subsection 5.2.6). The adjustable range is often only -1 Hz to -2 Hz and the reason why the Δf set point is usually chosen moderate. Hence, the contrast is relatively weak in images exhibiting atomic resolution. From experiences on other samples like the ceria crystals SCO or cleaved CaF_2 normally the frequency shift set point can be increased to a level where the atomic resolution is more distinct while on the film, increasing Δf leads to a loss of contrast. The lower Δf set point corresponds to a larger tip surface distance and a lower interaction, hence, the contrast in the measured images is reduced. An image representing the best obtainable atomic resolution is shown in figure 5.3. The image shows a 2.3 nm×2.3 nm small area with very well separated atoms where even a weak secondary contrast feature can be observed that might correspond to the oxygen in the second layer. The small scanning area results in a noticeable deformation of the lattice due to thermal drift. The KPFM image (b) is a representative example for the atomic Kelvin contrast on the film surface. The lattice can be recognized in KPFM but the potential variations are small. Generally, the interpretation of the Kelvin contrast on the atomic scale is controversial [122] and sometimes interpreted as an artefact, and we leave it here as is without interpretation.
For comparable CaF_2 (111) surfaces, a tip and distance dependent contrast formation where either the top or the sub lattice is more dominant is well known [123]. On the ceria film a contrast change is presented in figure 5.4 (a) The corresponding KPFM (b) reveals that the contrast change is accompanied by a local potential change of approx. 50 mV which may result from a slightly changed charging of the tip [124]. Opposite to CaF_2 surfaces, on the ceria surfaces this contrast changes are hardly ever observed and hence have usually not to be considered during image interpretation.

5.2 Effects of surface reduction, oxidation and vacancy formation

5.2.1 The surface Morphology of Si supported ceria (111) films under condition of UHV-annealing

The details on the film have already been discussed in chapter 4.3.1. Although the film samples are grown with high quality and it is confirmed that the film is fully oxidized, the surface morphology is unknown.
With the NC-AFM technique combined with KPFM, we measured the surface structure of the as grown films and additionally investigated the influence of the temperature on the surface morphology by annealing from room temperature to 1200 K in UHV. We find a metastable surface with a pyramidal structure for the as grown film that is stable in the low temperature regime up to 930 K. This pyramidal structure is based on a wedding cake like growth mechanism. In the high temperature regime from 930 K upwards the samples expose a surface morphology with large atomically flat terraces which are rich of step structures. These observations are confirmed by SPA-LEED measurements.
For the LEED measurements and appropriate interpretation the support of Dr. H. Wilkens and Prof. J. Wollschläger (University of Osnabrück, 49076 Osnabrück, Germany) is gratefully acknowledged.

Results are published in [18] APPLIED PHYSICS LETTERS 104, 081910 (2014).

The publication shows that the ceria film is a ideal model system, as large flat terraces are predestined for high resolution NC-AFM imaging. However, in this work only the surface morphology is examined and in consequence of the results we also examined the surface details on a atomic scale basis. Those measurements, presented in sections 5.2.4 and 5.2.5, lead to the observation of reconstructed surfaces and to the observation of vacancies, hydroxyl species and water on the surface. Further, as this work was exclusively performed in UHV it opened the question how annealing the samples in UHV, air or in a oxygen environment effects the reduction state. That is discussed in the next section 5.2.2.

APPLIED PHYSICS LETTERS 104, 081910 (2014)

A well-structured metastable ceria surface

R. Olbrich, [1] H. H. Pieper, [1] R. Oelke, [1] H. Wilkens, [1] J. Wollschläger, [1] M. H. Zoellner, [2], T. Schroeder, [2] and M. Reichling [1],a)
[1] Fachbereich Physik, Universitat Osnabrück, Barbarastr. 7, 49076 Osnabrück, Germany
[2] IHP, Im Technologiepark 25, 15236 Frankfurt (Oder), Germany

(Received 10 January 2014; accepted 11 February 2014; published online 25 February 2014)

Abstract
By the growth of a 180 nm thick film on Si(111), we produce a metastable ceria surface with a morphology dominated by terraced pyramids with an oriented triangular base. Changes in the nanoscale surface morphology and local surface potential due to annealing at temperatures ranging from 300K to 1150K in the ultra-high vacuum are studied with non-contact atomic forcemicroscopy and Kelvin probe force microscopy. As the surface is stable in the temperature range of 300K to 850K, it is most interesting for applications requiring regular steps with a height of oneO-Ce-O triple layer. [http://dx.doi.org/10.1063/1.4866667]

5.2.2 The surface Morphology of Si supported ceria (111) films after annealing in air and in a controlled oxygen atmosphere

In the previous section, the basic morphology of the film samples is described whereby the experiments were carried out under *UHV* conditions. When an oxygen containing material is annealed in a low oxygen environment, which is the case for *UHV* conditions, it always has to be considered that oxygen can be released by the surface, as it is the case for ceria (see section 4.2). Furthermore, it is well known that apart from a reduction of ceria (from CeO_2 to Ce_2O_3) an oxidation is possible (from Ce_2O_3 to CeO_2) during an annealing in oxygen [82, 93, 94, 97]. To investigate the reduction and the oxidation of the film, a NC-AFM study is performed with annealing the film samples in UHV, ambient conditions and in a controlled oxygen atmosphere in a UHV chamber. The annealing procedure takes 10 hours but the gain temperature regime of 850 K to 1070 K is only hold for one hour. The maximum partial pressure p_{O_2} during annealing in oxygen is 1×10^{-5} mbar. After each preparation step, XPS measurements are carried out and a careful analysis of the Ce3d, O1s and C1s regions in the XPS spectrum is performed whereby a comparative analysis of the Ce^{4+} and Ce^{3+} amount allows a precise determination of the oxidation state [125].
The NC-AFM measurements show that the surface morphology is very similar for annealing in UHV, when annealing in air or in an oxygen atmosphere. All three preparation methods result in large flat terraces separated by step edges. The annealing in air leads to a contamination which cannot be completely removed by further UHV annealing but only by annealing in oxygen. Generally, the samples annealed in an oxygen atmosphere reveal the best surface quality free of visible contaminants on large areas. The XPS measurements confirm that the film reduces during annealing in UHV at higher temperatures as the Ce^{3+} increases drastically. XPS also confirms that the samples can be fully reoxidized by the oxygen treatment.
As our NC-AFM setup presented in chappter 3 is not sufficient for sample preparation in a high pressure (10^{-5} mbar) oxygen atmosphere, the measurements were carried out in Marseille (CINaM institute, CNRS, Aix-Marseille University, Marseille, France). The support by C. Barth, C. Laffon, A. Ranguis and Ph. Parent is gratefully acknowledged.

The results are published in SCIENTIFIC REPORTS 6:21165 (2016) [19].

SCIENTIFIC REPORTS 6:21165

A perfectly stoichiometric and flat CeO_2 (111) surface on a bulk-like ceria film

C. Barth[1] , C. Laffon[1], R. Olbrich[2], A. Ranguis[1], Ph. Parent[1] and M. Reichling[2]

[1] Aix-Marseille University, CNRS, CINaM UMR 7325, 13288 Marseille, France.
[2]Fachbereich Physik, Universität Osnabrück, Barbarastr. 7, 49076 Osnabrück, Germany. Correspondence and requests for materials should be addressed to C.B. (email: barth@cinam.univ-mrs.fr)

Abstract

In surface science and model catalysis, cerium oxide (ceria) is mostly grown as an ultra-thin film on a metal substrate in the ultra-high vacuum to understand fundamental mechanisms involved in diverse surface chemistry processes. However, such ultra-thin films do not have the contribution of a bulk ceria underneath, which is currently discussed to have a high impact on in particular surface redox processes. Here, we present a fully oxidized ceria thick film (180 nm) with a perfectly stoichiometric CeO_2 (111) surface exhibiting exceptionally large, atomically flat terraces. The film is well-suited for ceria model studies as well as a perfect substitute for CeO_2 bulk material.

5.2.3 Line defect formation on the (111) surface of Si supported ceria films and ceria crystals compared to cleaved CaF_2 crystals

In section 5.2.1, screw dislocations observed on the film surface have been mentioned in the publication. This kind of feature is classified as a line defect. Line defects are a common observation on many kinds of surfaces whereby screw and edge dislocation are the most prominent examples. Line defects usually form during the growth of materials or crystals due to high pressure, temperature gradients or strong forces acting on the materials due to internal stress or during post processing.
To obtain a picture of the line defects commonly found on cerium oxide, we use NC-AFM images to identify the defects and compare the defect structure of ceria crystals with the films. Additionally, we compare the line defects with a rare line defect observed on a cleaved CaF_2 crystal.
In our study, screw dislocations are the most frequently observed defect on the surface of ceria films and crystals and connect different terrace levels without passing step edges. On the atomic scale, we find an extended Burgers circuit for a screw dislocation which indicates the presence of an edge dislocation. Generally, the ceria crystal and film surface show similar line defects, although they were grown under very different conditions. The defects on the CaF_2 crystal surface differ greatly and reveal that the growing and post preparation conditions are the key element in the defect formation.

The results are prepared for publication and shown as a manuscript draft.

To be submitted

A comparative study on line defects on fluorite type (111) surfaces

R Olbrich[1] , H.H. Pieper[1], S. Torbruegge[1], M. Temmen[1], C. Barth[2] and Michael Reichling[1]

[1]Fachbereich Physik, Universität Osnabrück, Barbarastr. 7, 49076 Osnabrück, Germany.
[2] Aix-Marseille University, CNRS, CINaM UMR 7325, 13288 Marseille, France.

Abstract

Line defects on (111) fluorite type surfaces namely a ceria (CeO_2) crystal, a supported Si-ceria film and a calcium fluoride (CaF_2) crystal are studied with non-contact atomic force microscopy (NC-AFM) and Kelvin probe force microscopy (KPFM). We reveal a large amount of dislocations on the ceria film and ceria crystal surfaces, although, film and crystal are grown under very different conditions. Surface line defects on ceria can be assigned to screw dislocations where three different characteristics are predominant. Screw dislocations with a hexagonal shape forming top terrace levels, long straight step edges with interruptions and hexagonally shaped pits having their origin in screw dislocations. An atomically resolved screw dislocation exhibits slight lattice relaxation what is a hint for the presence of edge dislocations. In contrast, dislocations on the CaF2 crystal having equal lattice parameters are observed extremely rare and appear with a completely different shape. The screw dislocations on CaF_2 have a triangular shape and much larger dimensions.

A comparative study on line defects on fluorite type (111) surfaces

Authors: R. Olbrich, H.H. Pieper, S. Torbruegge, M. Temmen, C. Barth and Michael Reichling

Abstract:
Line defects on (111) fluorite type surfaces namely a ceria (CeO_2) crystal, a supported Si-ceria film and a calcium fluoride (CaF_2) crystal are studied with non-contact atomic force microscopy (NC-AFM) and Kelvin probe force microscopy (KPFM). We reveal a large amount of dislocations on the ceria film and ceria crystal surfaces, although, film and crystal are grown under very different conditions. Surface line defects on ceria can be assigned to screw dislocations where three different characteristics are predominant. Screw dislocations with a hexagonal shape forming top terrace levels, long straight step edges vanishing in the surface and hexagonally shaped pits having their origin in screw dislocations. An atomically resolved screw dislocation exhibits slight lattice relaxation what is a hint for the presence of edge dislocations. In contrast, dislocations on the CaF_2 crystal having equal lattice parameters are observed extremely rare and appear with a completely different shape. The screw dislocations on CaF_2 have a triangular shape and much larger dimensions.

1 Introduction

A perfect crystal or a perfectly grown film exhibits perfect atomic regularity; however real crystals always have imperfections. Imperfections already arise during the growth of crystals [1] and films [2] but can also be a result of stress exerted during post processing. There are kinds of different imperfections like one dimensional point and line defects and two and three dimensional surface and volume defects. The most prominent line defects which are commonly referred to dislocations are the edge and screw dislocations. In real crystals, the strict separation between edge and screw dislocations is not always useful as dislocations can be a mixture of both [3]. There are many studies on line defects on different materials including FCC structures [4-14]. Although, a lot of experimental [15-23] and theoretical studies [24-30] have been conducted dealing with point defects like surface vacancies, there are much less studies on line defects for ceria [31-33]. It is well known that dislocations can influence crystal growth and eventually material properties [34-38]. Recently it has been shown that the diffusion kinetics for ceria is strongly influenced by edge dislocations [39]. Furthermore, the surface morphology of ceria play a crucial role in catalytic applications [40, 41]. As the surface morphology can significantly depend on dislocations a surface study looking at the type and amount of dislocations, is most desirable.
Here, we present and compare experimental data on dislocations observed with an atomic force microscope operated in the non-contact mode (NC-AFM), a technique that is well suited for high resolution imaging of an insulating oxide surface [42] on two different CeO_2 (111) samples, namely the surface of a ceria single crystal and the surface of a ceria film. Both systems exhibit high amount of dislocations on the surface which has similar properties although the crystal and the film are grown under very different conditions. To compare the observed dislocations with another fluorite type surface, we have chosen a CaF_2 (111) crystal where dislocations after preparation are uncommon and differ greatly although the lattice parameter are equal.

2 Experimental

Ceria crystals (Commercial Crystal Laboratories, Naples, FL, USA) are produced with an induction skull melting process [43] involving temperatures in the range of 1500-2000 K and temperature gradients in the melt of several hundred Kelvin. With such high temperatures it is obvious that thermal stress is one of the key elements for defect formation in ceria crystals during the growth.
The ceria film is grown at a temperature of approximately 900 K on a Si wafer with a 3 nm buffer layer of praseodymia by molecular beam epitaxy (MBE) and has a thickness of 180 nm, further details can be found in Ref. [44]. Although, the film growth temperature is moderate thermal stress may occur and introduce defects in the film. In previous studies we have already shown that the thick films have bulk like properties[45, 46].
Beside the thermal stress introduced during growth also post processing may create dislocations. For the crystals, the preparation consists of cycles of argon ion sputtering (U=1.5 keV; $P_{Argon}=5*10^{-5}$ mbar) and annealing to 1100 -1200 K. The preparation steps for the film follow a similar sequence but annealing temperatures are limited to 1000-1100 K as higher temperatures result in ceria silicate formation and decomposition of the film [45].Further details of the annealing process are described in [47].
CaF_2 crystals are commercially available (KORTH KRISTALLE GMBH, Altenholz, Germany). They are grown by the Bridgman-Stockbarger method [43]. The preparation steps consist of in-situ cleavage in UHV and post

annealing at 340 to 350 K to reduce charges on the surface. Hence, the thermal stress on the CaF_2 crystal surface is much lower compared to ceria but stress during cleavage has to be considered.
Measurements are carried out in two different ultra-high vacuum (UHV) systems at a base pressure in the low 10^{-10} mbar range or below. The force microscope used for measurements on ceria is a modified [48] commercial ultrahigh vacuum AFM/STM (Omicron NanoTechnology, Taunusstein, Germany). The force microscope used for measurements on CaF_2 is a well characterized [50-52] UHV 750 NC-AFM system (RHK Technology, Troy, MI, USA).
On both setups commercial type NCH Si Cantilevers (Nanosensors, Neuchatel, Switzerland) with a resonance frequency in the range of 300 kHz and a force constant of approximately 40 N driven by amplitudes of 10-20 nm are used. Interaction from electrostatic forces is minimized by applying a bias voltage. While for the CeO_2 crystal, the bias between the tip and sample is adjusted to a fix value [53], the bias for the film and for the CaF_2 crystal is dynamically adjusted yielding Kelvin probe force microscopy (KPFM) [54] images, revealing local potential variations on the surface. The NC-AFMs are operated in the constant frequency shift mode where the image contrast represents the topography of the surface [49].

3 Results and Discussion

Figure 1 shows representative topographic images from a well prepared cerium oxide (111) crystal surface. The surface is characterized by well-defined smooth terraces mostly separated by one or some triple layer (TL) (310 pm) straight steps. The surface morphology, dominated by hexagonal pits and protrusions has already been described in detail [55-58]. Here, we look at the high amount of dislocations on the surface. An impression of how typical dislocations look like when observed with NC-AFM is given in frame (a) and (b). In (a), a long straight step edge with the height of one TL which has some indentations can be seen. This step is vanishes into the surface and it is possible to move from the lower terrace level to the higher terrace level without passing the step itself. All dislocations where one can move over terrace levels without passing any step are screw dislocation. The apparent beginning of the screw dislocations is marked with a white arrow.

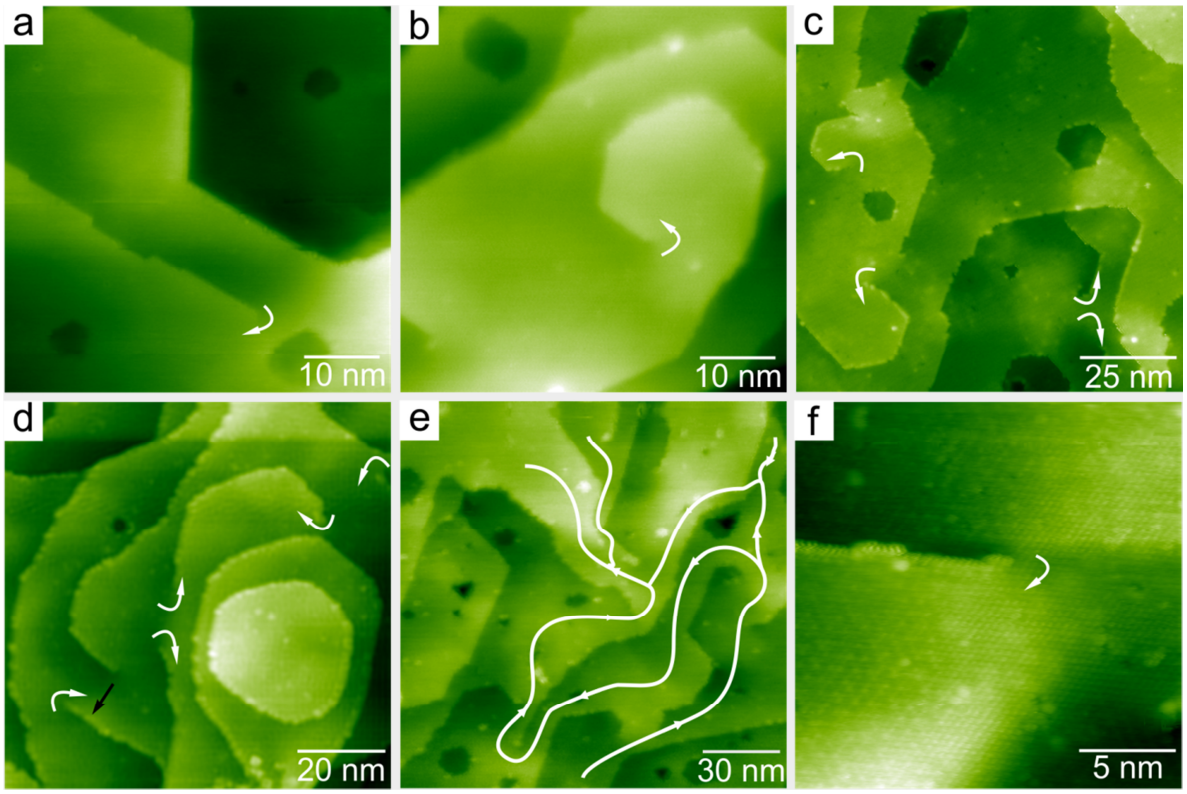

Figure 1 Selected NC-AFM topographic images representing the typical surface morphology of a bulk Ceria (111) surface after annealing to 1100-1200 K. The screw dislocations are marked with a white arrow showing in the positive direction of the screw dislocation. (a) and (b) show the two observed kind of screw dislocations. Straight steps suddenly interrupted and hexagonally shaped top terraces. More complex screw dislocations are shown in (c) and (d). Screw dislocations connecting four terrace levels are presented in (e). (f)is a close up image of the beginning of a screw dislocation with atomic contrast. The Burgers vector always points in [111] direction.

At this point, the step increases very fast and reaches about 130-200 pm height after only 1-3 nm from the starting point. To reach the full TL height, additional 8-12 nm are needed. This behaviour of steps at screw dislocations is a common observation we find for all screw dislocations on the ceria crystal and film. If we would draw a Burgers circuit into the image we would have to go from the lower terrace level following the white arrow to the higher terrace and closing the loop with passing the step edge. The Burgers vector would be at the step edge pointing in [111] direction and its length would be the connection for the additional way which is needed to pass the height of the step edge. Another kind of screw dislocation is shown in Figure 1 (b). Here, the screw dislocation is building the top terrace level on the surface having a well pronounced hexagonal shape. This kind of screw dislocation is found more often after annealing the crystal to 1200 K than after annealing to 1100 K. This is not surprising as more straight steps and hexagonally formed features are found for higher annealing temperatures [55, 56] but is a hint that this dislocation could arise from the post annealing and not during crystal growth. As in (a), the Burgers vector is pointing in [111] direction and also one terrace level with TL height is overcome by following the screw dislocation. Although, we observe many of steps with several TL height [55], a screw dislocation always connects terraces only with one TL height difference. A third possible kind of screw dislocation could have its origin in the rounded and hexagonally shaped pits.

Some more complex screw dislocations are presented in frame (c). Here, the four marked dislocations are all hexagonally shaped. While two screw dislocations connect top terrace levels, the other two dislocations are nearby pointing into the opposite direction so that we can move clock and counterclockwise to the next terrace level. This type of mirrored dislocations can also be observed in frame (d). We speculate that this dislocation arrangement has its origin in the Frank-Read mechanism [59, 60]. Another interesting feature is the terrace on the left part of the image in (d). The step at the end of the terrace is suddenly shifted about 12 nm and it appears that the whole terrace breaks at this point into two parts ongoing with the formation of a screw dislocation (see black arrow).
Image (e) reveals how several terrace levels can be connected over screw dislocations. Starting at the bottom right in the image and following the inserted line we reach the next higher terrace level. Here, one can move on the terrace to the next screw dislocation providing a connection to the third terrace level and even on this third terrace level we find a connection to the fourth terrace level. Overall, four terrace levels each with TL height can be overcome without passing any step just by moving along connections over screw dislocations.
A close-up view with slight atomic contrast of a screw dislocation of a type similar to the one shown in frame(a) is presented in frame (f). The screw dislocation starts in the middle of the image where the terrace splits into two parts. The asymptotic increasing behavior of the steps can also be observed. Following the beginning of the dislocation, the step increases very fast to approx. 120 nm height but has not reached TL height after 10 nm.

To obtain a better understanding of how a dislocation looks like in detail on the ceria surface images revealing the atomic structure of the dislocation are needed. Obtaining atomic resolution with NC-AFM over a screw dislocation is difficult as the tip has to be very close to the surface to have enough interaction to reveal atomic detailsbut has to overcome a step of 150-200 pm. Hence, atomic resolution over a screw dislocation is a compromise of getting enough details without taking the risk to crash into the step.
Two topographic images showing a screw dislocation with atomic details are presented in figure 2. The same screw dislocation is shown in (a) and (b) but the scanning angle is rotated parallel to the orientation of the dislocation in (b). This has the advantage that only a few scan lines have to be taken over for the scan stability critical step edge area while scanning in orthogonal direction to the step a lot more scan lines are crossing the step would cause a much higher probability for the feedback in z-direction to overshoot and loosing topographic details. This behavior can be seen in (a) where a few scan lines are faulty to overshooting z-feedback.
The screw dislocation starts in the middle of the image. The inserted Burgers circuit follows the positive direction of the screw dislocation. The Burgers vector is located at the step edge pointing out of the image in [111] direction. A cross-section is taken after 7 atoms from the starting point of the step edge. As the profile in (d) reveals, the step climbs up to 150 pm at this point which is approx. half of a TL. One can clearly see in (b) that the first three atoms of the beginning step have a much stronger increase in slope than the following atoms and nearly have already reached the 150 pm height.

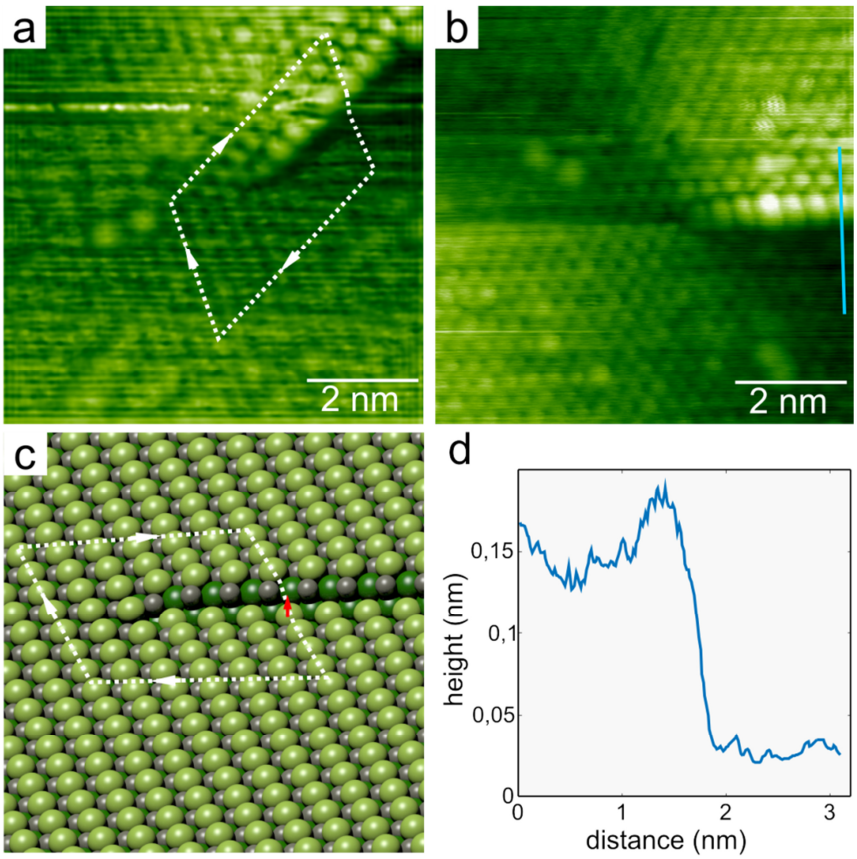

Figure 2 NC-AFM topographic imagesrevealing the atomic contrast of a screw dislocation on a bulk Ceria (111) surface. (a) The Burgers circuit is following the positive direction of the screw dislocation where one terrace level is overcome without crossing any step. The Burgers vector points in [111] direction and is located at the step edge (see red file in (c)). (b) for better scanning perfomance, the scanning angle is rotated parallel to the step. A carefull look reveals a extendet Burgers circuit indicating mixed screw and edge dislcocation. (c) illustration of a screw dislocation. (d) Profile from (b) showing that the step climbs 150 pm after seven atoms from its origin.

A carefull inspection on the Burgers circuit reveals that the circuit is extended and has a slight curve. Expecially the atoms around the beginning of the growing step are shifted lateraly and the atomic rows beneath the step seem to be somewhat compressed. This means, to close the Burgers loop not only the Burgers vector along the step edge has to be inserted but also a small additonal lateral way in the range of half an atomic row. This indicates that there must be some additional relaxation in the lattice which is caused most likely by an edge dislocation which can have its orgin in a deeper layer. Note that the dislocations shown in figure 1 can also be mixtures of screw and edge dislocation but we cannot see the edge dislocation as relaxation in the lattice can not be revealed without atomic resolution in NC-AFM images.
An illustration of a screw dislocation comparable to the AFM image is presented in figure 2 (c). The model is a visualisation of the screw dislocation and Burgers circuit generated with the rendering software Blender using the Atomic Simulation Environment (ASE) [61]. Still we can explain the very strong contrast in the AFM image at the shifted step edge which let atoms at step edge positions appear brighter and larger. With the increasing of the step the TL of O-Ce-O becomes visible and we have some additional surface atoms that can interact with the tip and distort the atomic contrast. As clearly visible, this is more difficult for the scanning direction parallel to the step edge (b) than for the orthogonal scanning direction.

Some evaluated topographical images representative for the typical morphology of the ceria film are shown in figure 3. The surface is characterized by well-formed terraces mostly separated by one or some TL height steps with some rounded or hexagonally shaped pits and protrusions. In contrast to the crystal, the terraces are larger and we find significant electrostatic potential differences and irregularities on the film. A detailed surface study can be found in Ref. [45]. To study the dislocations first an overview scan with a scan area of 400 nm x 400 nm is shown in (a). The screw dislocations are marked with white arrows and the high amount of dislocations (approximately 1×10^{10} screw dislocations/cm^2) is immediately visible. A careful inspection reveals 16 dislocations on the surface that can be classified into screw dislocations where straight step edges vanish into the surface and screw dislocations with hexagonal shape connecting top terraces. Some pits that are the

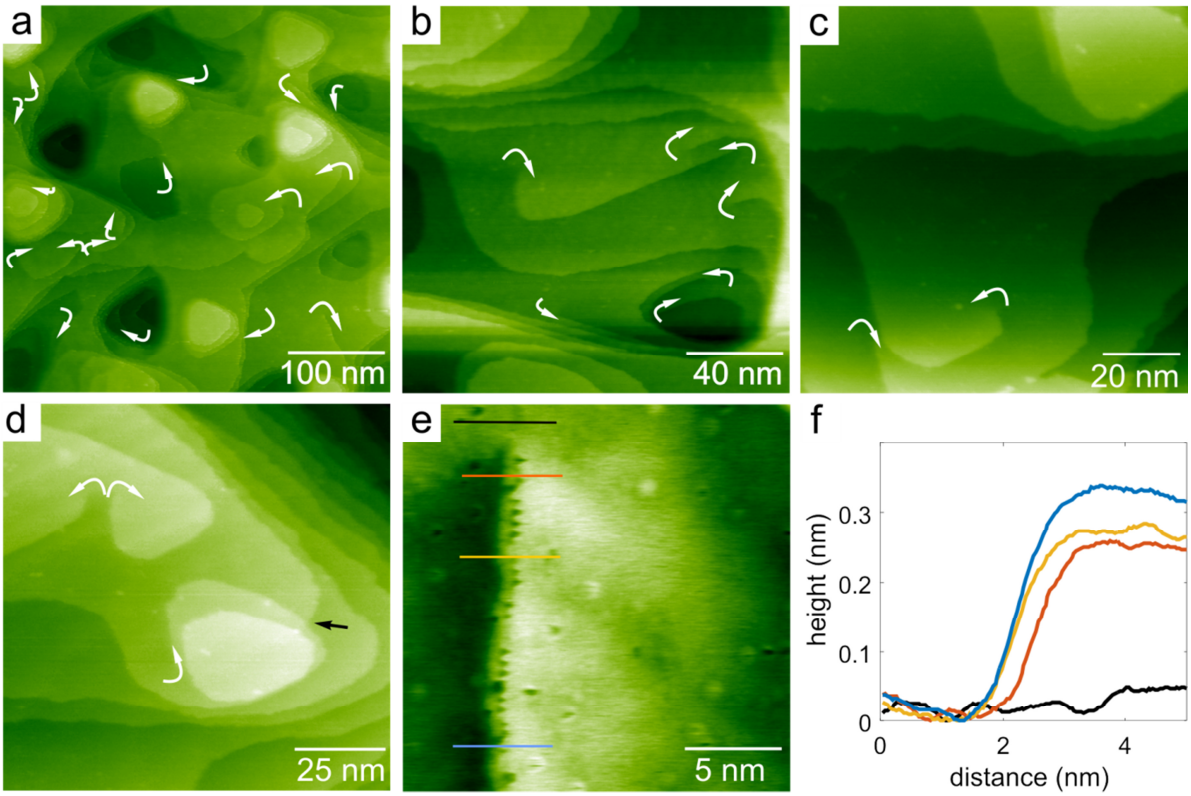

Figure 3 Selected NC-AFM topographic images representing the typical surface morphology of a Ceria (111) film after annealing at 1070 K. (a) The film surface is rich of screw dislocations (16 on 0.16 μm^2). As on the crystal, hexagonally shaped dislocations and dislocations at long straight steps are observed (b)-(e). The profile (e) and (f) show the fast climbing of steps directly after the dislocation origin and the slow increase to the end height of one TL. The dislocations are marked with the white circle which always points into the positive direction of the dislocation.

origin of a screw dislocation can be seen in (a) and (b). The pit shown in (b) can be clearly identified as the beginning of a screw dislocation moving along over three TL high very small terraces until the adjacent terrace at the end of the pit is reached. The upper part of frame (b) reveals an interesting combination of several screw dislocations. From three very closed by screw dislocations, two dislocations are parallel to each other and appear as foothills of the nearby terraces. The third dislocation in the middle is oriented counterclockwise and overall it appears that the terrace breaks at this point and the screw dislocation combination is of the same kind as the one seen in figure 1 (d).

A hexagonally shaped screw dislocation connecting top terrace levels is presented in (c). This dislocation can be compared to the one shown in figure 1(b), however, the hexagonal shape is less pronounced what can be explained by the lower annealing temperature for the film preparation compared to the preparation of bulk crystals. Mirrored screw dislocations are also present on the film surface as obvious from the image shown in (d) where the next terrace level can be reached clock and counterclockwise following adjacent screw dislocations. Another interesting feature in (d) is the screw dislocation where the complete terrace passes a step edge (see black arrow) without any effect on the terrace surface itself. A close up view of a screw dislocation is given in (e). Four cross-sections are taken at different distances from the origin of the beginning step and the profiles are presented in (f). The step climbs up to 220 pm (red profile) after 3-4 nm, however, after additional 4-5 nm the height increases just by 30 pm (yellow profile). The complete TL height of the step is reached after approx. 15 nm (blue profile). Note that structural feature is the same as on the crystal.
In summary, we can say that the ceria film shows the same type of screw dislocations as the ceria crystal. Further the amount of dislocations is similar (approximately $3{,}2 \times 10^{-10}$ scd/cm^2 (crystal) and $2{,}0 \times 10^{-10}$ scd/cm^2 (film)). Also on the film one dislocation always connects terraces with one TL height difference.
Beyond the discussed screw dislocations, we observe on the film two additional kinds of dislocations as illustrated in figure 4. In some cases, NC-AFM imaging reveal terraces that are shifted completely over their whole expansion one TL parallel to [111] direction. An example is shown in (a) where a large terrace is shifted exactly 310 pm. Interestingly, this terrace moves on over several step edges and also a pit without any change on its morphology. Even a screw dislocation is passed without any effect on the terrace. While in vertical direction

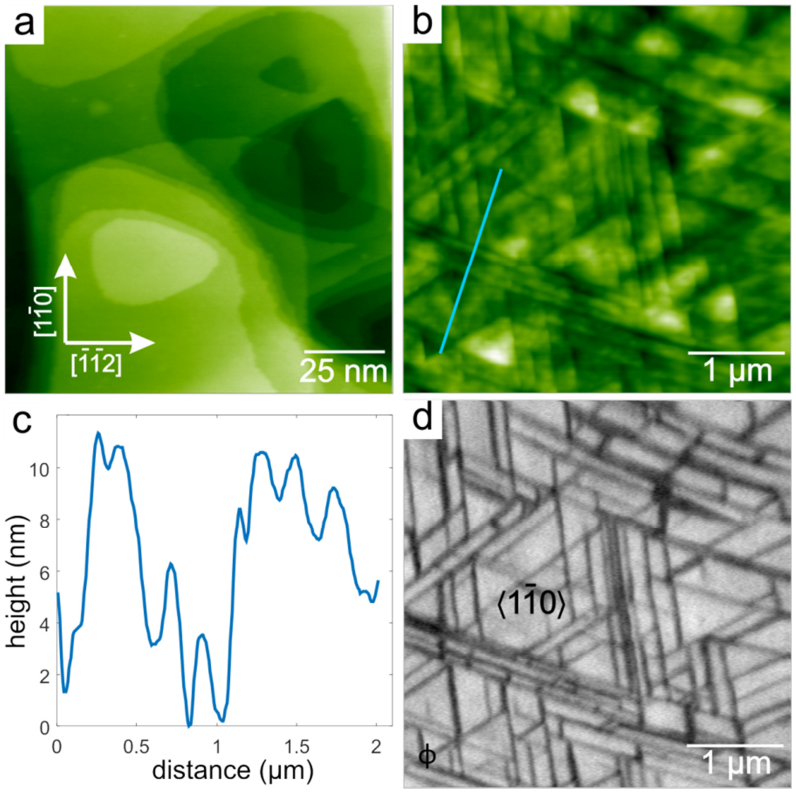

Figure 4 NC-AFM images showing two kinds of dislocations exclusively observed on the ceria film. (a) A terrace is completely shifted one TL in [111] direction and ongoing over step edges and screw dislocations without any effect on the terrace. (b) Topographic image showing slip planes {111} with ⟨1-1 0⟩ Slip directions. sc) Cross section profile showing the height differences. The corresponding KPFM-image in (d) reveals strong potential differences along the ⟨1-1 0⟩ slip directions.

the border of the terrace is very straight and moves along the [110] direction in [-1,-12] direction, the limit of the terrace is rounded and a preferred direction cannot be determined. The origin of such a structural feature must be in a deeper layer in the film, where a complete TL of O-Ce-O is shifted upwards.
The second dislocation type that is only found on the ceria film is shown in (b) and only appears for annealing temperatures near the critical limit of 1100 K just before the film decomposes. Very long straight lines rise through the complete surface. These lines can be seen even clearer in the corresponding KPFM image (d) revealing the electrostatic potential differences on the surface. Here, we can easily determine the ⟨1-10⟩ orientation of the lines. Together the lines form shifted equiangular triangles. In between the triangular areas the film morphology is not affected at all. The profile in (c) belongs to the cross section inserted in (b) and reveals that along the lines, the surface is shifted by about 2 to 6 nm. It is obvious that such strong dislocated lines must have a different origin than the other observed dislocations. We speculate that these lines are glide planes which are formed in the silicon substrate and cause a shift through the complete ceria film. This is supported by the fact that it is observed that Si forms ⟨1-10⟩ glide planes under condition of stress [62]. In our case, the high temperature annealing of the film introduces the building of the glide planes in the Si substrate and with increasing annealing time in the critical temperature regime, the glide planes get more pronounced and become visible on the ceria film surface as well. This also explains why we observe an increase of the shift up to 10 nm of these dislocation lines with increasing annealing cycles. The missing observation of such phenomenon on the crystal at even higher annealing temperatures also supports that the glide planes have their origin in the Si substrate of the film.

To get an impression of the influence of the lattice parameters on the line defects, a comparison with the surface of a CaF_2 (111) crystal is useful as the lattice constant difference between CaF_2 and CeO_2 is less than 1%.

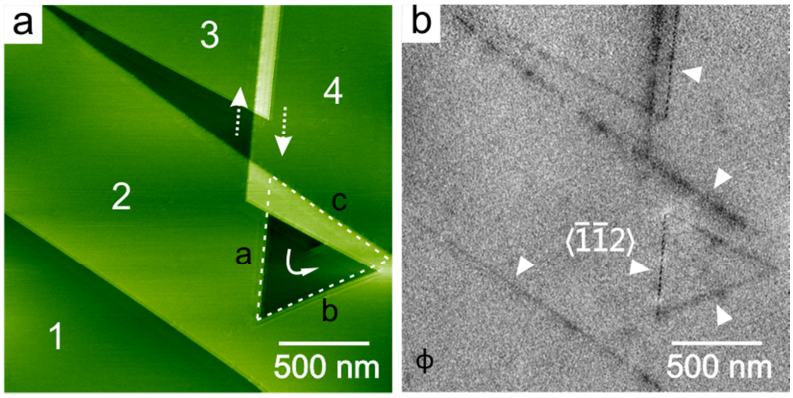

Figure 5 NC-AFM images of a cleaved CaF_2 (111) crystal surface.(a) The topographic image shows two dislocation types. A screw dislocation in form of a triangular pit and terraces (3, 4) broken up where the borders slide over one another ending in the formation of one TL height steps. (b) The KPFM image reveals only a contrast at the TL height step edges and the borders of the triangular screw dislocations corresponding to a locally lower surface potential. The white arrows assign steps of type II [63] at ⟨1-21⟩ directions. The curved arrow in (a) marks the positive direction of the screw dislocation. The dashed equilateral triangle shows that only the borders (a, b) of the screw dislocation are of type II and the third side is shifted into the dislocation.

Figure 5 presents a topographic NC-AFM image taken on a UHV cleaved CaF_2 crystal surface with its corresponding KPFM image. The morphology of cleaved CaF_2 surfaces differs significantly from CeO_2 [64, 65]. Plain terraces with a width of several hundred nanometers or even in the micrometer range are not unusual; in figure 5 (a), on the shown area of 4 μm^2, only four terraces are present. In strong contrast to CeO_2 only a small amount of dislocation is observed on CaF_2. most of the cleaved crystals are free of dislocations and the defects shown in fig 5 (a) is a rare exception. Hence, we speculate that the stress on the CaF_2 crystal during cleavage is much lower than the thermal stress on the CeO_2 samples during annealing. Beside the quantity of dislocations, also the shape of the dislocations differs strongly. The NC-AFM image reveals two kinds of dislocations. The triangular shaped pit can be assigned as the origin of a screw dislocation. It is comparative with the hexagonal screw dislocations on the ceria surfaces but has much larger dimensions with an edge length over 500 nm. Unlike on the hexagonal pits, here the top terrace cannot be reached by following the positive direction of the screw dislocation in the pit but instead is delimited by a TL height step edge. Interestingly, a walk around the triangular pit is possible without passing any step. This behavior can be explained when taking the other visible dislocation type and the KPFM image into account. From the appearance we conclude that terraces (3) and (4) break up and slide counterwise while the borders push each other resulting in a displacement of some ten to hundred nanometers and folding of the edges on top of each other. It is well known that for CaF_2 two predominant steps, namely type I and type II exist [63]. By the KPFM image these step types can be distinguished from different local potential variations. Hence, the marked steps in the KPFM image can all be assigned to type II corresponding to <-1-12> directions. Note that the KPFM image here is shown with inverted contrast compared to [63] in order to represent the surface potential instead of the applied bias voltage to equalize this potential. Obviously, step a and b at the triangular pit include an angle of 60° and are of type II. The third limiting step of the triangular only have an angle of 52° but as the dashed triangle indicates a step II type including an angle of 60° can be found at position c which moves along the edge of terrace 2. However, the third limiting step could still be of type II and just be shifted which could also explain the similar KPFM contrast of this step. Therefore, we speculate that terrace 4 slips into terrace 2 resulting in the compressed triangular pit whereby also the step edge at the end of the screw dislocation in the pit can be explained.

4 Conclusion

We have shown that dislocations are always present at ceria surfaces. Almost every dislocation on the surface can be assigned to a screw dislocation and a careful inspection reveales the possible presence of edge dislocations. We find that there is no big difference in the kind and amount of dislocations on a thick ceria film compared to a ceria single crystal. This is a surprising observation as the film is grown under very different conditions with much lower temperatures than the ceria crystals. As the film undergoes higher temperatures during post deposition annealing than during its MBE growth we speculate that dislocations arise more from our sample preparation rather than during initial film growth. For the crystals, the thermal stress is stronger during growing and we speculate that dislocations also form during growing. Furthermore, we presented a screw dislocation with atomic resolution which allows a good understanding on how a screw dislocation looks

like in detail on the ceria surface. The steps at screw dislocation positions always increase up to 150 to 200 pm after 1 to 2 nm from the origin but reach the height of one TL only after additional 10 to12nm. This asymptotic behavior in increase is observed for all screw dislocations. While step edges on the film and crystal exist that have the height of several TL every observed screw dislocation only connects terrace levels that are separated by one TL. Screw dislocation can be categorized into three types: hexagonally shaped step edges connecting top terrace levels, hexagonal pits reaching the surface terraces and straight step edges vanishing into the surface. The hexagonally shaped screw dislocations become more pronounced at higher annealing temperatures. Due to the screw dislocations, we can move along the surface over several terrace levels without passing step edges and, hence, the dislocations are a connection to different terrace levels. So far, the film reveals two additional dislocation types. One TL shifted terraces and glide planes shifted by several nanometers. Whereas the reason of the arise of the former one cannot be revealed the later one can be assigned to ⟨1-10⟩ glide planes that form in the Si substrate due to thermal stress during annealing close to a critical temperature.

In strong contrast to the dislocations we observed on ceria are dislocations on CaF_2 surfaces. While on ceria dislocations are a common feature on CaF_2 they are exceptional. Also the shape of the few dislocations found on CaF_2 is strongly different. Hence, the influence of the fluorite type lattice parameter is of minor importance for the formation of line defects whereas the preparation, growing conditions and material properties of the samples are much more significant.

We are grateful for providing the ceria film samples to Prof. Dr. T. Schroeder (IHP, Im Technologiepark 25, 15236 Frankfurt (Oder))

References

1. Billig, E., *Some Defects in Crystals Grown from the Melt I. Defects Caused by Thermal Stresses.* Proceedings of the Royal Society of London Series a-Mathematical and Physical Sciences, 1956. **235**(1200): p. 37-55.
2. Gao, H.J., *Some general properties of stress-driven surface evolution in a heteroepitaxial thin film structure.* Journal of the Mechanics and Physics of Solids, 1994. **42**(5): p. 741-772.
3. Hull, D. and D.J. Bacon, *Introduction to Dislocations* 2011, Butterworth-Heinemann: Elsevier.
4. Stemmer, S., et al., *Dislocations in $PbTiO_3$ Thin Films.* Physica Status Solidi a-Applied Research, 1995. **147**(1): p. 135-154.
5. Święch, W., M. Mundschau, and C.P. Flynn, *Characterization of single crystal films of molybdenum (011) grown by molecular beam epitaxy on sapphire (1120) and studied by low-energy electron microscopy.* Surface Science, 1999. **437**(1-2): p. 61-74.
6. Qin, Y.L., et al., *Dislocations in $SrTiO_3$ thin films grown on $LaAlO_3$ substrates.* Journal of Materials Research, 2002. **17**(12): p. 3117-3126.
7. Rodney, D., *Molecular dynamics simulation of screw dislocations interacting with interstitial frank loops in a model FCC crystal.* Acta Materialia, 2004. **52**(3): p. 607-614.
8. Nicola, L., et al., *Plastic deformation of freestanding thin films: Experiments and modeling.* Journal of the Mechanics and Physics of Solids, 2006. **54**(10): p. 2089-2110.
9. Jin, Z.H., et al., *The interaction mechanism of screw dislocations with coherent twin boundaries in different face-centred cubic metals.* Scripta Materialia, 2006. **54**(6): p. 1163-1168.
10. Martinez, E., et al., *Atomistically informed dislocation dynamics in fcc crystals.* Journal of the Mechanics and Physics of Solids, 2008. **56**(3): p. 869-895.
11. Peranio, N. and O. Eibl, *Gliding dislocations in Bi_2Te_3 materials.* Physica Status Solidi a-Applications and Materials Science, 2009. **206**(1): p. 42-49.
12. Fertig III, R.S. and S.P. Baker, *Dislocation dynamics simulations of dislocation interactions and stresses in thin films.* Acta Materialia, 2010. **58**(15): p. 5206-5218.
13. Hunter, A., et al., *Influence of the stacking fault energy surface on partial dislocations in fcc metals with a three-dimensional phase field dislocations dynamics model.* Physical Review B, 2011. **84**(14): p. 144108.
14. Heyde, M., G.H. Simon, and L. Lichtenstein, *Resolving oxide surfaces - From point and line defects to complex network structures.* Physica Status Solidi B-Basic Solid State Physics, 2013. **250**(5): p. 895-921.
15. Grinter, D.C., et al., *Defect structure of ultrathin ceria films on Pt(111): Atomic views from scanning tunnelling microscopy.* Journal of Physical Chemistry C, 2010. **114**(40): p. 17036-17041.
16. Jerratsch, J.F., et al., *Electron Localization in Defective Ceria Films: A Study with Scanning-Tunneling Microscopy and Density-Functional Theory.* Physical Review Letters, 2011. **106**(24): p. 246801.
17. Lu, J.L., et al., *Morphology and defect structure of the CeO2(111) films grown on Ru(0001) as studied by scanning tunneling microscopy.* Surface Science, 2006. **600**(22): p. 5004-5010.

18. Nörenberg, H. and G.A.D. Briggs, *Defect structure of nonstoichiometric CeO_2(111) surfaces studied by scanning tunneling microscopy.* Physical Review Letters, 1997. **79**(21): p. 4222-4225.
19. Nörenberg, H. and G.A.D. Briggs, *Defect formation on CeO_2(111) surfaces after annealing studied by STM.* Surface Science, 1999. **424**(2-3): p. L352-L355.
20. Shahed, S.M.F., Y. Sainoo, and T. Komeda, *Scanning Tunneling Microscope Study of Surface Morphology Variation of CeO_2(111) with Changing Annealing Condition.* Japanese Journal of Applied Physics, 2011. **50**(8): p. 08LB05.
21. Esch, F., et al., *Electron Localization Determines Defect Formation on Ceria Substrates.* Science (Washington, DC, United States), 2005. **309**(5735): p. 752-755.
22. Namai, Y., K.-i. Fukui, and Y. Iwasawa, *Atom-Resolved Noncontact Atomic Force Microscopic Observations of CeO_2(111) Surfaces with Different Oxidation States: Surface Structure and Behavior of Surface Oxygen Atoms.* Journal of Physical Chemistry B, 2003. **107**(42): p. 11666-11673.
23. Namai, Y., K.-i. Fukui, and Y. Iwasawa, *Atom-resolved noncontact atomic force microscopic and scanning tunneling microscopic observations of the structure and dynamic behavior of CeO_2(111) surfaces.* Catalysis Today, 2003. **85**(2-4): p. 79-91.
24. Nolan, M., S.C. Parker, and G.W. Watson, *The electronic structure of oxygen vacancy defects at the low index surfaces of ceria.* Surface Science, 2005. **595**(1-3): p. 223-232.
25. Wang, Y.L., et al., *The effect of oxygen vacancy concentration on the elastic modulus of fluorite-structured oxides.* Solid State Ionics, Diffusion & Reactions, 2007. **178**(1-2): p. 53-58.
26. Wang, Y.G., et al., *DFT+U Study on the Localized Electronic States and Their Potential Role During H_2O Dissociation and CO Oxidation Processes on CeO_2(111) Surface.* Journal of Physical Chemistry C, 2013. **117**(44): p. 23082-23089.
27. Sayle, T.X.T., S.C. Parker, and C.R.A. Catlow, *The Role of Oxygen Vacancies on Ceria Surfaces in the Oxidation of Carbon-Monoxide.* Surface Science, 1994. **316**(3): p. 329-336.
28. Plata, J.J., A.M. Márquez, and J.F. Sanz, *Transport properties in the CeO_{2-x} (111) surface: From charge distribution to ion-electron collaborative migration.* Journal of Physical Chemistry C, 2013. **117**(48): p. 25497-25503.
29. Paier, J., C. Penschke, and J. Sauer, *Oxygen Defects and Surface Chemistry of Ceria: Quantum Chemical Studies Compared to Experiment.* Chemical Reviews, 2013. **113**(6): p. 3949-3985.
30. Nolan, M., et al., *Density functional theory studies of the structure and electronic structure of pure and defective low index surfaces of ceria.* Surface Science, 2005. **576**(1-3): p. 217-229.
31. Maicaneanu, S.A., D.C. Sayle, and G.W. Watson, *Evolution and atomistic structure of dislocations defects and clusters within CeO_2 supported on ZrO_2.* Chemical Communications, 2001. **2001**(03): p. 289-290.
32. Li, Z.P., et al., *Dislocation associated incubational domain formation in lightly gadolinium-doped ceria.* Microscopy and Microanalysis, 2011. **17**(1): p. 49-53.
33. Sayle, T.X., et al., *Mechanical properties of ceria nanorods and nanochains; the effect of dislocations, grain-boundaries and oriented attachment.* Nanoscale, 2011. **3**(4): p. 1823-37.
34. Frank, F.C., *The influence of dislocations on crystal growth.* Discussions of the Faraday Society, 1949. **5**(5): p. 48-54.
35. Frank, F.C., *Crystal growth and dislocations.* Advances in Physics, 1952. **1**(1): p. 91-109.
36. Seeger, A., *The generation of lattice defects by moving dislocations, and its application to the temperature dependence of the flow-stress of F.C.C. crystals.* Philosophical Magazine, 1955. **46**(382): p. 1194-1217.
37. Penn, R.L. and J.F. Banfield, *Imperfect oriented attachment: Dislocation generation in defect-free nanocrystals.* Science, 1998. **281**(5379): p. 969-971.
38. Bierman, M.J., et al., *Dislocation-driven nanowire growth and Eshelby twist.* Science, 2008. **320**(5879): p. 1060-1063.
39. Sun, L., D. Marrocchelli, and B. Yildiz, *Edge dislocation slows down oxide ion diffusion in doped CeO_2 by segregation of charged defects.* Nature Communications, 2015. **6**: p. 6294.
40. Fornasiero, P. and A. Trovarelli, *Catalysis by Ceria and Related Materials*. 2014, London: Imperial College Press.
41. Gandhi, H.S., G.W. Graham, and R.W. McCabe, *Automotive exhaust catalysis.* Journal of Catalysis, 2003. **216**(1-2): p. 433-442.
42. Lauritsen, J.V. and M. Reichling, *Atomic resolution non-contact atomic force microscopy of clean metal oxide surfaces.* Journal of Physics: Condensed Matter, 2010. **22**(26): p. 263001.
43. Dhanaraj, G., et al., *Springer Handbook of Crystal Growth*. 2010, Berlin: Springer.
44. Zoellner, M.H., et al., *Stacking behavior of twin-free type-B oriented CeO_2(111) films on hexagonal Pr_2O_3(0001)/Si(111) systems.* Physical Review B, 2012. **85**(85): p. 035302.
45. Olbrich, R., et al., *A well-structured metastable ceria surface.* Applied Physics Letters, 2014. **104**: p. 081910.
46. Barth, C., et al., *A perfectly stoichiometric and flat CeO2(111) surface on a bulk-like ceria film.* Scientific Reports, 2016. **6**: p. 21165.
47. Pieper, H.H., et al., *Versatile system for the temperature-controlled preparation of oxide crystal surfaces.* Review of Scientific Instruments, 2012. **83**: p. 055110.
48. Torbrügge, S., et al., *Improvement of a dynamic scanning force microscope for highest resolution imaging in ultrahigh vacuum.* Review of Scientific Instruments, 2008. **79**(8): p. 083701.
49. Gritschneder, S., Y. Iwasawa, and M. Reichling, *Strong adhesion of water to CeO_2(111).* Nanotechnology, 2007. **18**: p. 044025.
50. Lübbe, J., et al., *Achieving high effective Q-factors in ultra-high vacuum dynamic force microscopy.* Measurement Science and Technology, 2010. **21**(10): p. 125501.

51. Lübbe, J., et al., *Thermal noise limit for ultra-high vacuum noncontact atomic force microscopy.* Beilstein Journal of Nanotechnology, 2013. **4**: p. 32-44.
52. Lübbe, J., L. Doering, and M. Reichling, *Precise determination of force microscopy cantilever stiffness from dimensions and eigenfrequencies.* Measurement Science & Technology, 2012. **23**(4): p. 045401.
53. Gritschneder, S., et al., *Structural features of CeO_2(111) revealed by dynamic SFM.* Nanotechnology, 2005. **16**(3): p. S41-S48.
54. Nonnenmacher, M., M.P. O'Boyle, and H.K. Wickramasinghe, *Kelvin probe force microscopy.* Applied Physics Letters, 1991. **58**(25): p. 2921-2923.
55. Pieper, H.H., et al., *Morphology and nanostructure of CeO_2(111) surfaces of single crystals and Si(111) supported ceria films.* Physical Chemistry Chemical Physics, 2012. **14**(44): p. 15361-15368.
56. Torbrügge, S., M. Cranney, and M. Reichling, *Morphology of step structures on CeO_2(111).* Applied Physics Letters, 2008. **93**(7): p. 073112.
57. Torbrügge, S., et al., *Manipulation of individual water molecules on CeO_2(111).* Journal of Physics: Condensed Matter, 2012. **24**: p. 084010.
58. Torbrügge, S., et al., *Evidence of Subsurface Oxygen Vacancy Ordering on Reduced CeO_2(111).* Physical Review Letters, 2007. **99**(5): p. 056101.
59. Durbin, S.D., W.E. Carlson, and M.T. Saros, *In situ studies of protein crystal growth by atomic force microscopy.* Journal of Physics D-Applied Physics, 1993. **26**(8B): p. B128-B132.
60. Springholz, G., et al., *Spiral growth and threading dislocations for molecular beam epitaxy of PbTe on BaF_2 (111) studied by scanning tunneling microscopy.* Applied Physics Letters, 1996. **69**(19): p. 2822.
61. *Atomic Simulation Environment*. Feb. 2016; Available from: https://wiki.fysik.dtu.dk/ase/.
62. Wei, Y., L. Li, and I.S.T. Tsong, *Surface morphology of Si(111)-(7×7) under an external isotropic tensile stress* Journal of Vacuum Science & Technology a-Vacuum Surfaces and Films, 1995. **13**(3): p. 1609-1612.
63. Pieper, H.H., C. Barth, and M. Reichling, *Characterization of atomic step structures on CaF_2(111) by their electric potential.* Applied Physics Letters, 2012. **101**: p. 051601.
64. Overney, R.M., et al., *Cleavage Faces of Alkaline-Earth Fluorides Studied by Atomic Force Microscopy.* Surface Science, 1992. **277**(1-2): p. L29-L33.
65. Reichling, M., et al., *Degradation of the CaF_2(111) surface by air exposure.* Surface Science, 1999. **439**(1-3): p. 181-190.

5.2.4 Ordered surface and subsurface vacancies. The progressive reduction from CeO_2 to Ce_2O_3

As outlined in chapter 4.2 cerium oxide can be found in a brought range of oxidation states from its fully oxidized state CeO_2 to its fully reduced state Ce_2O_3. In chapter 5.2.2 it was shown that the ceria film can be reduced by annealing in UHV and in chapter 5.2.1 the preparation of reduced ceria surfaces with large flat terraces was introduced. In ref. [93] it has been shown by LEED measurements that the ceria film exposes unique surface reconstructions during the reduction process. As LEED measurements cannot give an as precise picture as NC-AFM imaging these results consequently lead to the question of how the surface reconstruction are look in detail when observed with NC-AFM.
In our measurements on ceria film samples, we observed several intermediate phases depending on the annealing temperature. NC-AFM images reveal several stoichiometries with unique surface reconstructions. We observe a $(\sqrt{7} \times \sqrt{7})$R19,1°, $(\sqrt{3} \times 7)$R19,1°, $(\sqrt{3} \times \sqrt{3})$R30° and the (1×1) A-type reconstruction in our experiments whereby the $(\sqrt{3} \times 7)$R19,1°, $(\sqrt{3} \times \sqrt{3})$R30° are not known from literature and the former reconstruction is the only reconstruction that stabilizes in an oblique rather than a hexagonal structure.
Our cooperative partners M. V. Ganduglia-Pirovano (Instituto de Catálisis y Petroleoquímica, Consejo Superior de Investigaciones Científicas-CSIC, 28049 Madrid, Spain), and G. E. Murgida (Departamento de Física de la Materia Condensada, GIyA, CAC-CNEA, 1650 San Martín, Buenos Aires, Argentina) show with a theoretical DFT+U and thermodynamically statistical approach that the top layers of the film surface builds slices of reduced ceria forming stoichiometries that cannot be stabilized in the bulk. The observed surface reconstructions are modeled and a precise knowledge of their stability is obtained. Further the annealing temperature and partial oxygen pressure conditions for their occurrence in the AFM experiment is examined.
The support of G. E. Murgida, V.Ferrari, A. M. Llois, C. Barth, M. V. Ganduglia-Pirovano is gratefully acknowledged.

The results are published in The Journal of Physical Chemistry C , 121, 6844-6851 (2017).

The publication shows that for the ceria film a controlled stabilization of different surface phases is possible by annealing in UHV. However, on thin films the reduction by hydrogen [87] or CU [86] has been reported. For future experiments a controlled reduction by reducing agents observed by NC-AFM could be of interest. Further a NC-AFM study on atomic scale with the controlled oxidation of the fully reduced ceria film would show if the surface phases would appear in reverse order.

The Journal of Physical Chemistry C , 121, 6844-6851 (2017)

Surface stabilises ceria in unexpected stoichiometry

R Olbrich[1] , Gustavo E. Murgida[2], Valeria Ferrari [2], Clemens Barth[3], Ana Maria Llois[2], Michael Reichling[1] and Maria Verónica Ganduglia-Pirovano[4]

[1]Fachbereich Physik, Universität Osnabrück, Barbarastr. 7, 49076 Osnabrück, Germany.
[2] Departamento de Física de la Materia Condensada, GIyA, CAC-CNEA, 1650 San Martín, Buenos Aires, Argentina and Consejo Nacional de Investigaciones Científicas y Técnicas -CONICET, C1033AAJ, Buenos Aires, Argentina
[3] Aix-Marseille University, CNRS, CINaM UMR 7325, 13288 Marseille, France.
[4] Instituto de Catálisis y Petroleoquímica, Consejo Superior de Investigaciones Científicas-CSIC, 28049 Madrid, Spain

Abstract

The prototype reducible oxide ceria is known for its rich phase diagram and its ability to absorb and deliver oxygen. The high oxygen storage capacity is the basis for the use of ceria in catalytic and sensor applications where the surface plays a paramount role for device functionality. By direct imaging, we reveal the reconstruction of the ceria (111) surface in five periodic structures representing reduction states ranging from CeO_2 to Ce_2O_3 . Theoretical modelling shows that the $(\sqrt{7}\times3)$ R19.1° reconstruction representing the previously unknown Ce_3O_5 stoichiometry is stabilised at the surface but cannot be assigned to a bulk structure. Statistical modelling explains the thermodynamic stability of surface phases depending on the oxygen chemical potential and the coexistence of certain phases over a range of temperatures. These results are crucial for exploiting geometric and electronic structure-function correlations and the rational design of novel ceria-based functional systems.

5.2.4.1 Details of reconstructed surfaces revealing the ι- and oblique phases

The previous section introduced the series of observed surface reconstructions. It was shown that the reconstructions exclusively depend on the temperature of annealing in UHV. It is obvious from the relatively narrow temperature range where the different phases appear that the preparation of these reconstructions is not straightforward. Even when the uncertainty at the annealing temperature is overcome, not every time a sufficient resolution is achieved in NC-AFM imaging to observe the reconstructed surface. To understand the measurement series where most reconstructions could be successfully imaged in more detail, we look at some images from two different series. Results from the first series are compiled in figures 5.5, 5.6, 5.7 while figures 5.8 and 5.9 are taken from the second series.

Figure 5.5 shows a result for a ceria film surface annealed at 1020 K. The overview scan in (a) reveals the typical high temperature morphology with large terraces separated by step edges. A careful inspection reveals that there is an additional local structure near step edges. The corresponding KPFM image (b) shows only minor potential variations in the range of 40 to 60 mV on the surface where only the triangular pit appears with a strong contrast. The topographic images (c) and (d) represent the framed areas in image (a) with the Δf set point slightly increased from -1,5 Hz to approx. -2,5 Hz. At this relative low Δf set point the surface reconstructions are imaged at the step edges but appear as blurry bright spots. To reveal the impact of the Δf set point on the appearance of contrast features in NC-AFM images, we choose an area of 30 nm × 30 nm and repeated the imaging on this area while increasing the Δf set point. This is shown in figure 5.6 (a-d). The images present three terraces separated by TL steps. For a Δf value of -2,5 Hz (a) only near the steps, the reconstructed surface is visible. In image (b), the set point

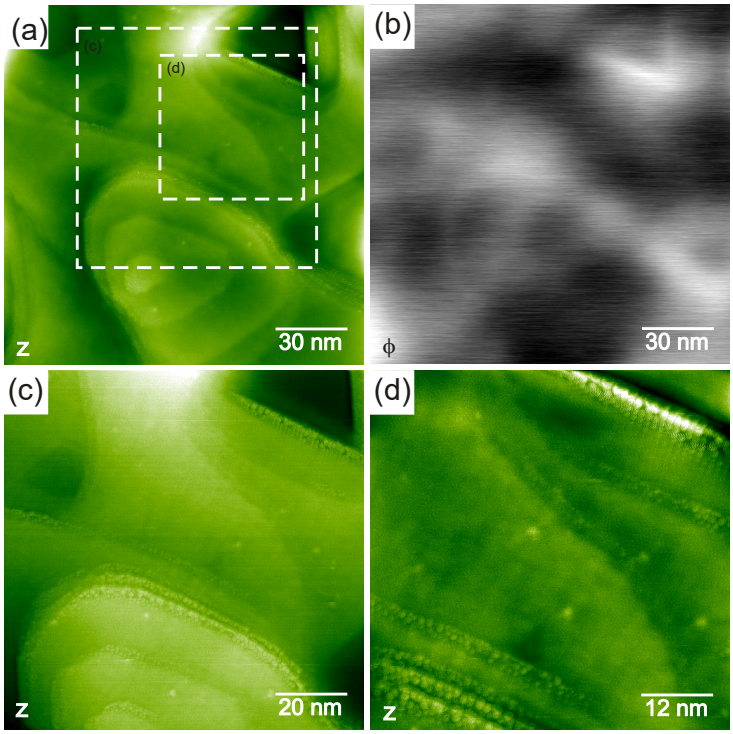

Fig. 5.5: (a) Topographic NC-AFM image taken on the ceria film M1969 after annealing at 1020 K. The surface consist of large terraces separated by mostly single Tl height steps. (b) Corresponding KPFM image showing small potential variations (40 to 60 mV). (c,d) Topographic images showing the framed areas in (a). Even on large frames, the surface reconstructions can be resolved nearby steps.

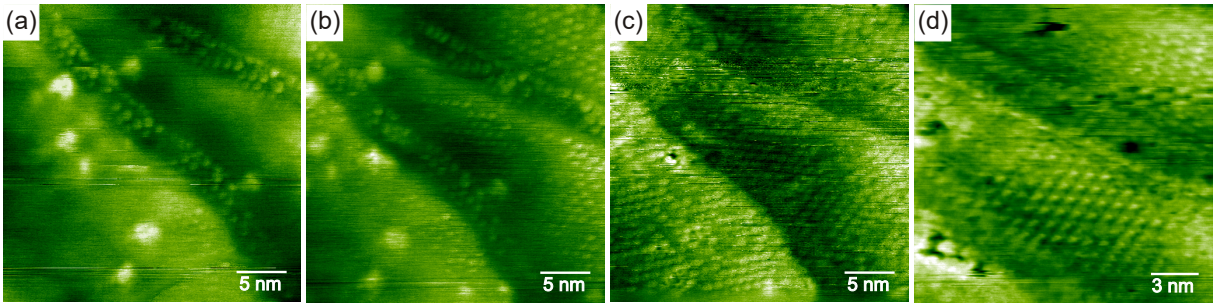

Fig. 5.6: Topographic NC-AFM images with slightly increased Δf set points taken on the film M1969 showing two TL step edges. (a) $\Delta f \approx$-2.5 Hz. (b) $\Delta f \approx$-3 Hz. (c) $\Delta f \approx$-4 Hz. (d) $\Delta f \approx$-7.5 Hz. With increasing set point the surface reconstructions are resolved with much better contrast. The top terrace shows the oblique reconstruction and the other two terraces both show the ι-phase but with different rotation.

is increased to (-3 Hz) whereby the reconstructed surface gets also more clearly visible on terrace areas. Increasing the set point to -4 Hz results in image (c). Here the ι- and oblique reconstructions are observed on the complete surface area. Although, the periodicity and rotation of the reconstructions can be revealed, the overall contrast is still a bit blurry. Only a stronger increase of the set point to -7,5 Hz results in a sharp contrast as shown in image (d). From the images we can reveal the oblique surface phase for the top terrace and the ι-phase for the two other terraces which appear with different rotation ($\pm 19, 1^{\circ}$).

Figure 5.7 shows the frequency shift- (a) and KPFM- image (b) matching to figure 5.6 frame (d). The increased Δf set point results in a strong contrast in the frequency shift image as also the topography feedback controller is set to a slower regulation (quasi constant height modus). The oblique and ι-phase are highlighted in the image by their unit cells. The KPFM image reveals an area with a good contrast at the nanoscale while on the rest of the area no noticeable potential variations are measured. This area is highlighted by the dashed square in the images and shown enlarged and with an expanded contrast scale in (c) and (d). It is obvious from the images that tip changes influence the contrast [124] in the KPFM image strongly resulting in a stronger contrast in the frequency shift image. For the parts where potential variations in the range of 20 mV are measured, the Δf-image reveal the oblique phase with several smaller bright and less bright spots of nuclear size. This spots could correspond to surface and subsurface vacancies as described in the previous introduced model for the oblique phase. In the middle of the image, the Kelvin contrast is less pronounced for some scan lines while in the Δf-image, the oblique phase is imaged with only some more extended bright and dark spots which is comparable to the already described contrast of the oblique phase in most NC-AFM images. Having passed this region the contrast changes again to the former observation but changes back after a few scan lines. This observation lead to the question whether the contrast imaged during the regulation of KPFM is more accurate or if this contrast is an artifact introduced by the Kelvin feedback loop. As the contrast matches well to the derived surface model, we speculate that the tip changes result in a sharper tip apex and that the tip is

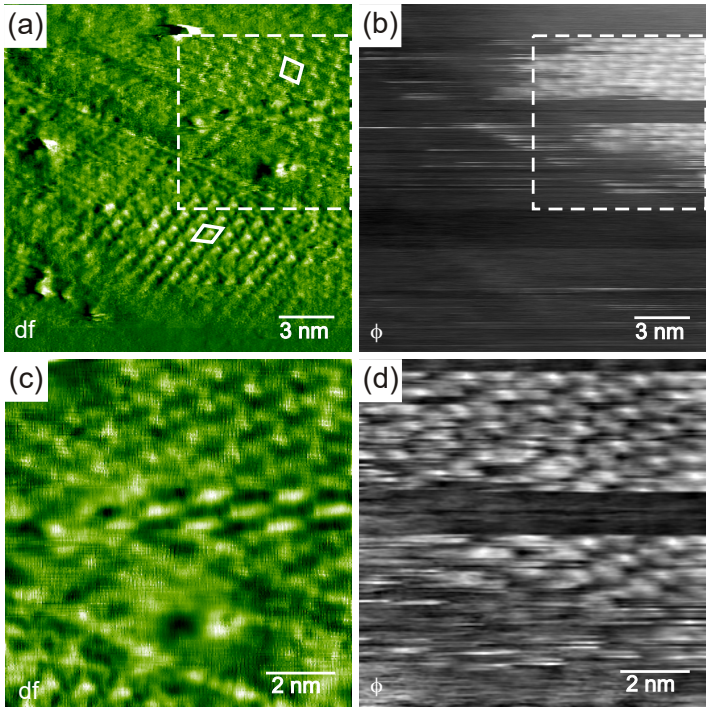

Fig. 5.7: Frequency shift and KPFM images corresponding to figure 5.6 (d). For the highlighted part of the image (shown enlarged and with enhanced contrast in (c, d)), the KPFM contrast is also clear on the nanoscale which results from a tip change. The different tip conditions lead to two different contrasts. While the KPFM image contrast is strong, the oblique phase is imaged with several smaller brighter and darker spots. When the KPFM image reveals only a minimal contrast, the oblique phase is observed only as four larger bright spots. The overall potential variations are in the range of 20 mV.

on a different potential. This explains the contrast change in the KPFM image and the different contrast in the Δf-image.

The preparation history of the ceria film samples suggests that many measurements are performed on a reconstructed surface. However, in most of these measurements reconstructions could not be resolved and on the nanoscale the surface appeared irregular. We speculate that the condition of the tip is most important for the observation of the surface phases and that tip changes that are difficult to control are necessary to obtain a sufficient image quality on reconstructions. In figure 5.8 (a) a topographic NC-AFM image is shown revealing the usual surface morphology. The white arrows mark two points where the contrast changes induced by a tip change at a step edge. The tip change results in a much better resolution on terraces and step edges. After the tip change, the terrace areas which were former imaged with irregular contrast reveal the described reconstructions even at a lower Δf set point indicating a much stronger tip surface interaction. Especially on larger frames of 25 nm × 25 nm (b), the reconstructions appear with a strong contrast. Over these spots, the frequency shift difference is relatively high which allows the observation of the ι- and oblique- phases on frames with up to 80 nm × 80 nm. One disadvantage of the strong interaction is that it is very difficult to reveal atomic resolution on some of the reconstructions as only a slight increase of the Δf set point results in strong distortions. This is the reason why for the oblique phase more or less the NC-AFM image could not reveal single surface atoms (Fig. 2 (c) of the previous publication). For the ι-phase (Fig. 2 (b) of the previous publication), the bright dots can barely be resolved as three atoms. As the bright spots appear for both phases identical on larger frames we also assigned the bright spots of the oblique phase to three atoms which is consistent with the derived surface model. Figure 5.8 (c) shows that sufficient image quality for

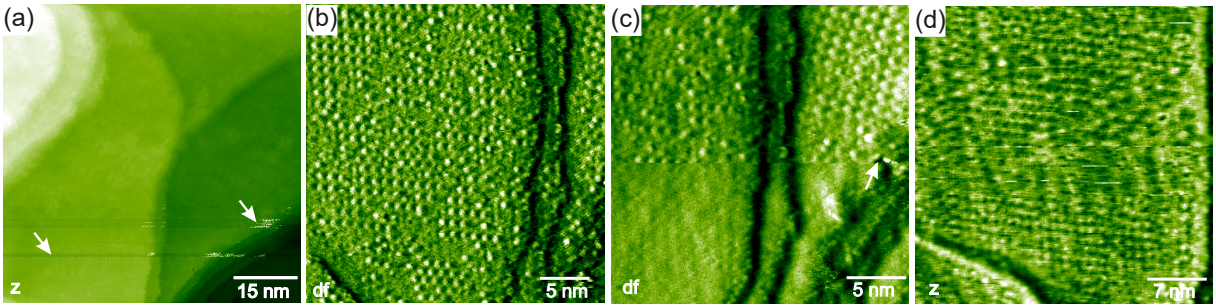

Fig. 5.8: NC-AFM images taken on the film M1969 revealing tip changes that result in a tip well suitable for the resolution of the surface reconstructions. (a) The topographic image shows two tip changes marked with the arrows. After the tip changes, the terrace and step structure is resolved much better. (b) Image revealing the oblique and ι-phase coexists on same terraces. (c) After a further tip change the reconstructions are nearly invisible in the image. (d) With an increased Δf set point the reconstructions can be resolved again but with lower quality.

revealing the surface reconstructions can also be lost due to a tip change. Here, a surface irregularity highlighted by the white arrow lead to a minor tip change so that the contrast from the surface reconstruction nearly vanishes, although, the step edges are still imaged with a strong contrast. After this change we could image the reconstruction again by increasing the Δf set point but as shown in the topographic image in figure 5.8 (d) with a significantly lower resolution. In summary, only a small range of tip conditions yield a satisfactory image quality to identify surface reconstructions on an otherwise irregular appearing surface.

As mentioned above, the relatively strong tip surface interaction allows the observation of the reconstructed surface on large scales. An example is shown in figure 5.9 (a). The topographic image with a size of 80 nm $\times$ 80 nm reveals the ι- and oblique- (O) phases coexisting on terraces. Also in this measurement, a tip change highlighted by the white arrow is necessary to obtain a sufficient resolution to observe the reconstructed surface. The image shows that the oblique phase is preferentially located near step edges while the ι-phase is found in the middle of terraces. Image (b) is an enlarged frame of image (a) and the inserts show the positions of the images (c-f). The images (c) and (d) show in more detail the domination of the ι-phase on terraces and the oblique phase is found near by steps. Overall, the slight domination of the ι-phase matches the previously shown stability plot (Fig. 4 of the previous publication) as this phase is minimally energetically preferred over a broad range of temperatures.

The findings discussed above demonstrate that ordered surface vacancies usually occur in form of reconstructed surfaces on the ceria film. The investigation of different observed phases helps to expand the knowledge of surface structures and helps in the identification of phases beyond the conventionally bulk phase diagram and may be crucial for new materials discovery, for instance, of metastable phases. We discussed the major challenge for obtaining a sufficiently high resolution to observe surface reconstructions in NC-AFM measurements. To increase the image quality and to observe the reconstructed surfaces

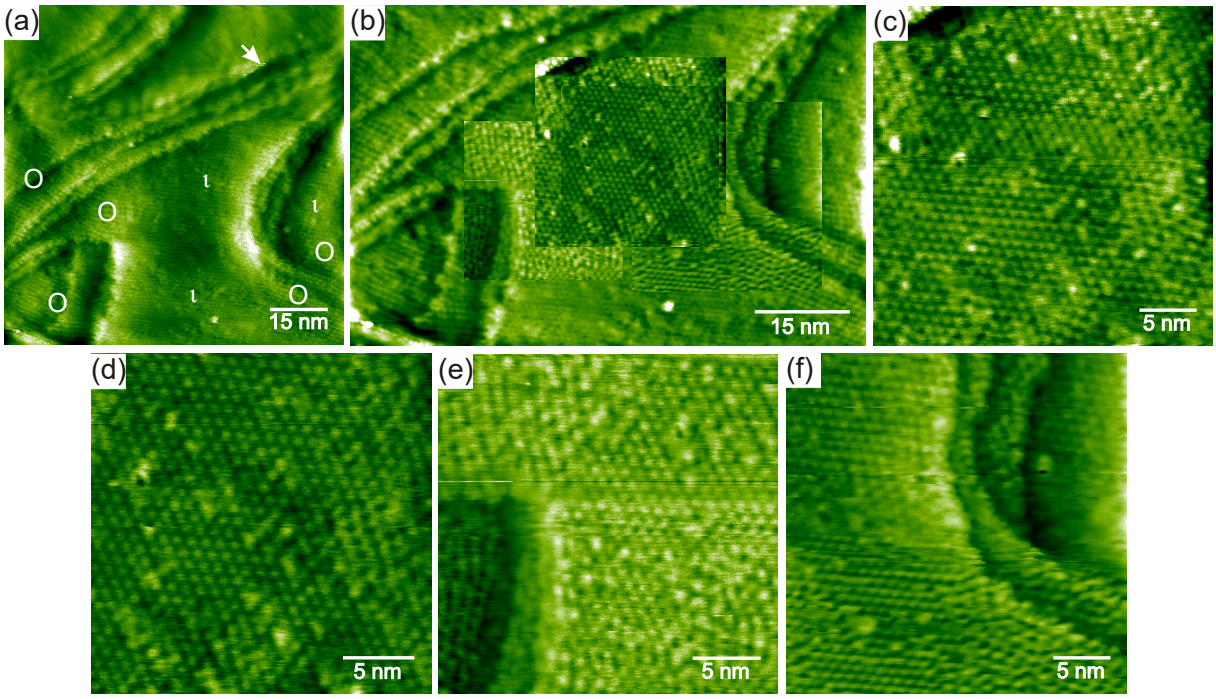

Fig. 5.9: (a) Topographic image taken on the film M1969. The contrast is strongly enhanced after a tip change (arrow), whereby the reconstructed surface can even be resolved on a large scale of (80 nm × 80 nm). The terraces reveal the ι- and oblique- phase. (b) Enlarged excerpt from (a) showing the scan positions of the images (c-d). (c,d) Area covered with the iota phase. (e) Near the step edge, the iota phase merge with the oblique phase. (f) While in top the ι- phase expands over both sides of the step edge in the bottom only the oblique phase is located at the step edge.

more frequently, it should be considered to perform NC-AFM measurements at low temperatures. This may help prohibiting unwanted tip changes and should allow gathering more details on the atomic scale.

5.2.5 Vacancies, hydroxyls and water on the ceria surface.

In this section, we focus on unordered surface vacancies that we observe during our measurements on the film surface. Further, we show surface protrusions that are assigned to hydroxyls and a high coverage of the ceria film surface with water molecules.

NC-AFM measurements on $CeO_2(111)$ single crystal surfaces revealed a relative low amount of surface defects assigned to oxygen vacancies [65, 73, 83, 104, 105, 108, 126–128]. This was a bit unexpected as the preparation of this surfaces with annealing cycles at temperatures in a range of 1100 to 1200 K under UHV conditions is expected to lead to a partial surface reduction. It is speculated that the high oxygen reservoir in the single crystals suppresses the reduction and vacancy formation at the surface. However a 2×2 surface reconstruction assigned to CeO_2 with subsurface oxygen defects has been observed and explained [110, 129].
In contrast to the single crystals, on the cerium oxide film we observe much more surface vacancies for similar preparation conditions. As shown in the previous section 5.2.4 the film surface exposes the A-type of Ce_2O_3 after annealing at 1070 K.
In figure 5.10, a measurement series revealing several surface vacancies is shown. The film sample is prepared with careful annealing cycles at 1070 K. The topographic image series is taken after the thermal drift is minimal so that the scan area remains nearly the same over a period of 30 minutes and the same vacancies can be observed in consecutive images. Over the complete series, a weak atomic contrast is achieved revealing a 1×1 surface reconstruction. However, the image series shows on an area of 6×6 nm^2 a relatively large amount of surface defects which appear as dark spots with the size of single atoms. We interpret these defects as oxygen surface vacancies leading to a local surface reduction. Another observation is that the amount of vacancies is not constant during the series and that the positions of vacancies change. To identify vacancies that vanished or changed position we marked them in the images with an "x". Vacancies that newly appear are marked with an "v" and position stable vacancies are marked with an "s". Over the complete series, there are only two stable vacancies forming the only apparent vacancy pair at the surface in the series. Some surface vacancies are stable over the time period of image (d) to (g) (20 min). A lot of vacancies that disappear in following images are observed in the images (a) and (b). In (b) six vacancies cannot be assigned again in image (c) but some vacancies on new positions are observed which may indicate vacancies hopping to new positions. However, from the NC-AFM images it cannot be derived if the vacancies have moved or vanished. A careful look reveals that some vacancies are imaged only partly. We speculate that these vacancies change or form just at the time of measurement. It also has to be considered that the measurement itself may provoke and support vacancy formation or movement as the tip exerts strong local forces on surface oxygen atoms. This is reinforced by the common observation of tip changes over irregularities like vacancies. In the image series, tip changes are avoided by choosing a relative low frequency shift set point which has the disadvantage of only obtaining a weak atomic contrast. However, the series reveals that the film surface provides much more surface vacancies than the surfaces of single crystals and is probably locally more reduced.
An image series showing small protrusions at the atomic scale is presented in figure 5.11. The topographic images are obtained after several annealing cycles at a temperature of

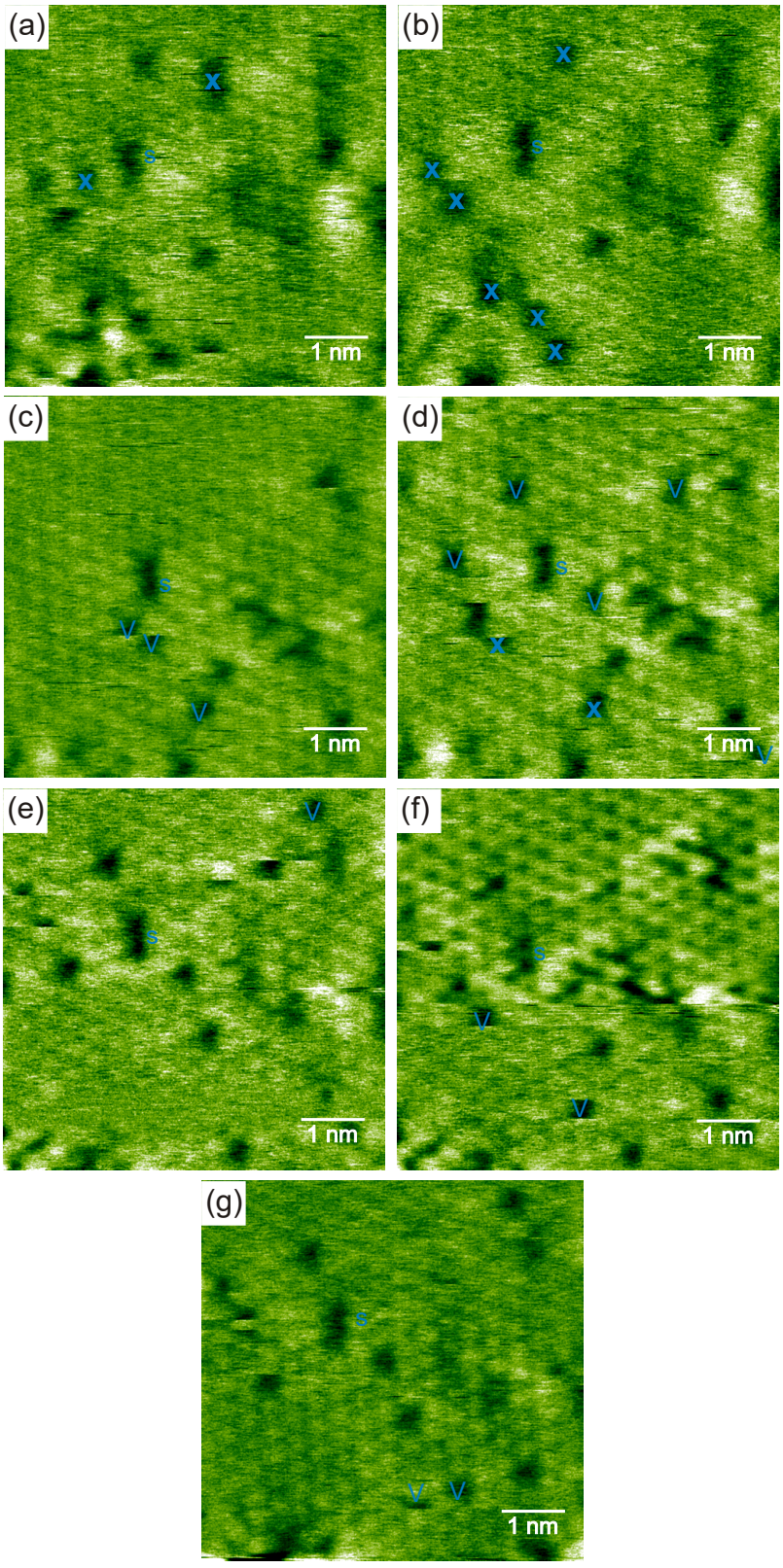

Fig. 5.10: NC-AFM topographic images series revealing surface vacancies. Every image takes approx. 5 minutes of time. Hence image, (g) was taken 30 minutes after image (a). All images show a weak atomic contrast and a significant number of vacancies. The thermal drift is relatively low, so that the positions of features on every image can be identified and compared. Interestingly, the positions of the vacancies partly change from image to image and while some vacancies disappear some new appear. Some vacancies that disappear in the following images are marked with "x" and vacancies that appear or changed the position are marked with "v". A stable vacancy pair over the complete series is marked with "s". From image (a) to (g), it can be summed up that some vacancies are stable and do not change their position while other vacancies rearrange completely or vanish.

approx. 1070 K and again reveal a 1×1 surface. Image (a) shows a scan area of $5\times5\,\mathrm{nm}^2$ and the white dashed line marks the scan area for the images (b-f) with a slightly de-

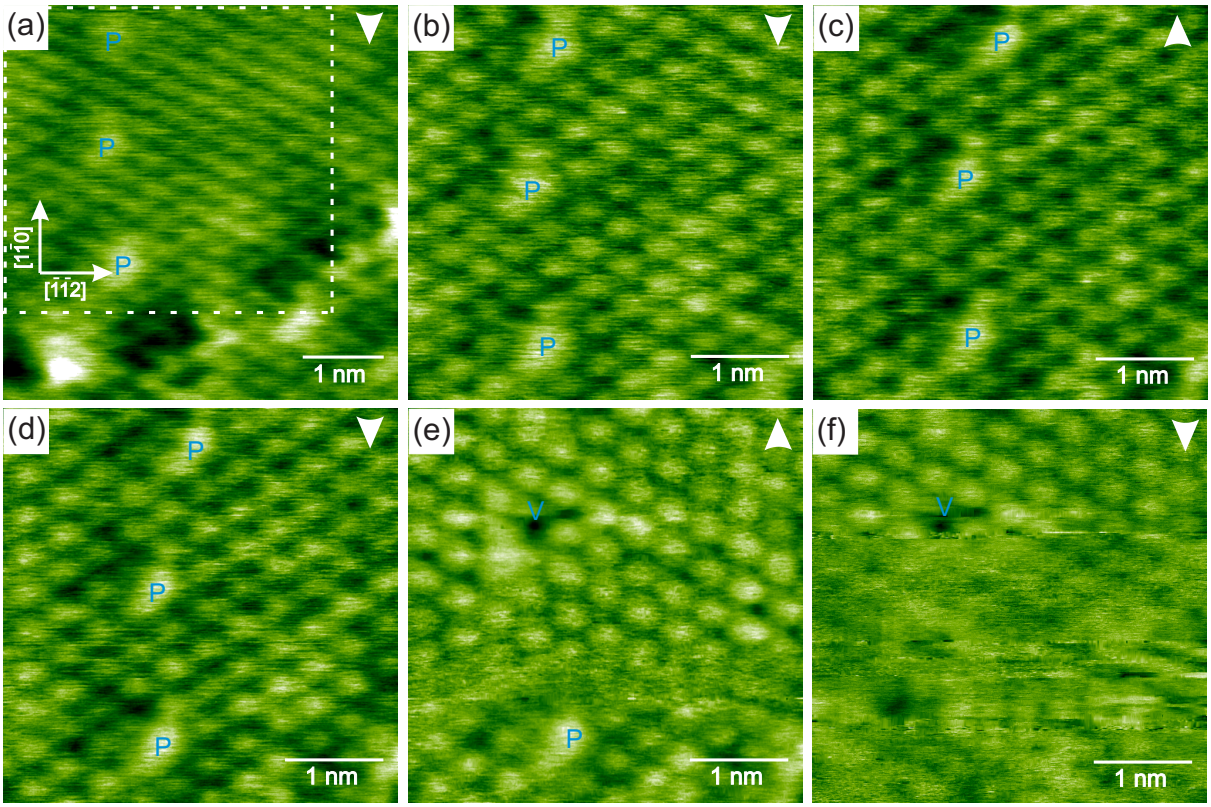

Fig. 5.11: (a-f) NC-AFM topographic images series on the ceria film surface (M1969) after 1070 K annealing cycles showing a contrast change. The white arrow indicates the scanning direction and the dashed line in (a) highlights the scan area of the images (b)-(f). Three small protrusions are marked with "P" and are observed at the same positions in images (a-d). In (e), the protrusion in the bottom of the image is still visible but after a slight contrast change, the atoms appear more disc-like and both other protrusions disappear but instead a hole marked with "V" appears.

creased scan area of $4\times4\,nm^2$. In this scan area, three small protrusions marked with "P" are imaged with brighter contrast. Comparing the protrusions in the images (b-e), the drift is below 10 pm per minute and can be neglected. The protrusions have a blurred contrast and seem to be positioned not on top of the surface oxygen atoms but instead more in between the atomic rows. This position is located over a subsurface cerium or oxygen atom. For the unreduced CeO_2 film, the surface directions are known as discussed in chapter 4.3.1. In this case the x direction corresponds to $[\bar{1}\,\bar{1}\,2]$ and the protrusions are positioned over subsurface oxygen. On the surface of single crystals, such protrusions are well known and have tentatively been assigned to hydroxyls trimers [127, 128]. Opposite to the observed protrusions hydroxyls trimers are usually imaged with a relative sharp contrast and the blurred contrast usually is assigned to water molecules on the surface as the H_2O molecule is not bounded so strongly and can rotate on the surface. Water molecules favor positions on top of subsurface cerium [117]. As already pointed out the NC-AFM images also could show the 1×1 A-type of Ce_2O_3. The corresponding models for CeO_2 and Ce_2O_3 are shown in figure 5.12. For Ce_2O_3 the model suggests a stacking in the form of A-C-B for the first Triple-Layer (O_{surf}-Ce-O_{sub}) while the stacking for the

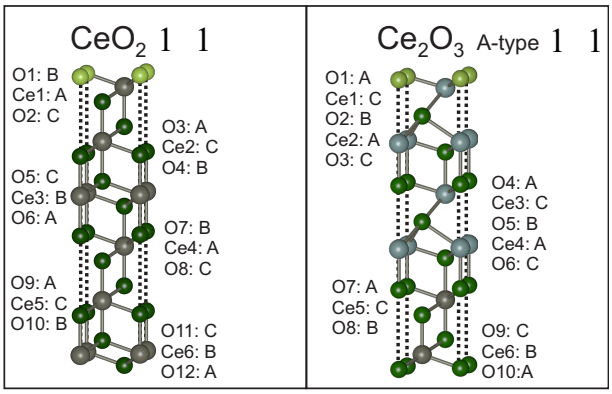

Fig. 5.12: Stacking sequence of the modeled CeO_2 and Ce_2O_3 unit cells. The models show a countercyclical stacking sequence.

clean CeO_2 surface is (B-A-C). For the $[\bar{1}\ \bar{1}\ 2]$ direction, this results that the upper three surface atoms are opposite in both structures. The Ce^{4+} position for CeO_2 corresponds to the subsurface O position for Ce_2O_3 and the subsurface O position corresponds to the Ce^{3+}. For the Ce_2O_3 A-type surface the observed protrusions are located on Ce-positions and we assign them to water molecules. Hence, the images in figure 5.11 show the Ce_2O_3 A-type surface.

Following the series, the position of the protrusions don't change in the first four images. In image (e), the protrusions at the bottom of the image are still visible, however a slight contrast change appears after a quarter of the image is recorded. The contrast change is apparent as the surface atoms that are imaged with a more disc-liked shape. The two other protrusions are not observed anymore but instead a small pit marked with "V" is imaged. This hole is still observed in the last image (f) of the series where the atomic resolution is lost after the first quarter of the image and could not be restored. Two possibilities can explain the observation; (i)either the former protrusion is measured as a pit due to a tip change accompanied with a changed interaction and resulting in a contrast inversion (ii) or the protrusion moved and a surface vacancy is formed. We speculate that the latter one is more realistic in this case as, although, the surface atoms appear with a more disc-like shape, they do not show a contrast inversion. The formed hole observed in image (e) is located neighbored of the previous protrusion whereby we suppose that there is no change of the scan area due to the slight contrast change during measuring as the tip has not been retracted. We speculate that the vacancy is formed due to the interaction of the surface with the water molecule and that the molecule has been absorbed by the tip.

The topographic image shown in figure 5.13 reveals also three protrusions, however, in contrast they are directly located on top of a surface oxygen atom which can be clearly seen from the enlarged image (b). This kind of protrusion has been assigned to single hydroxyls [127, 128]. In (c) an illustration of a single hydroxyl, a hydroxyl trimer and a water molecule on the ceria surface are presented. The easiest way to distinguish the three species from each other is the location with respect to the cerium lattice. The single hydroxyl is expected to be found on top of surface oxygen atoms, the hydroxyl trimers on subsurface oxygen positions and the water molecules on cerium positions. However, this approach of identifying the observed protrusions is only phenomenologically and relies on previous observation on ceria single crystals.

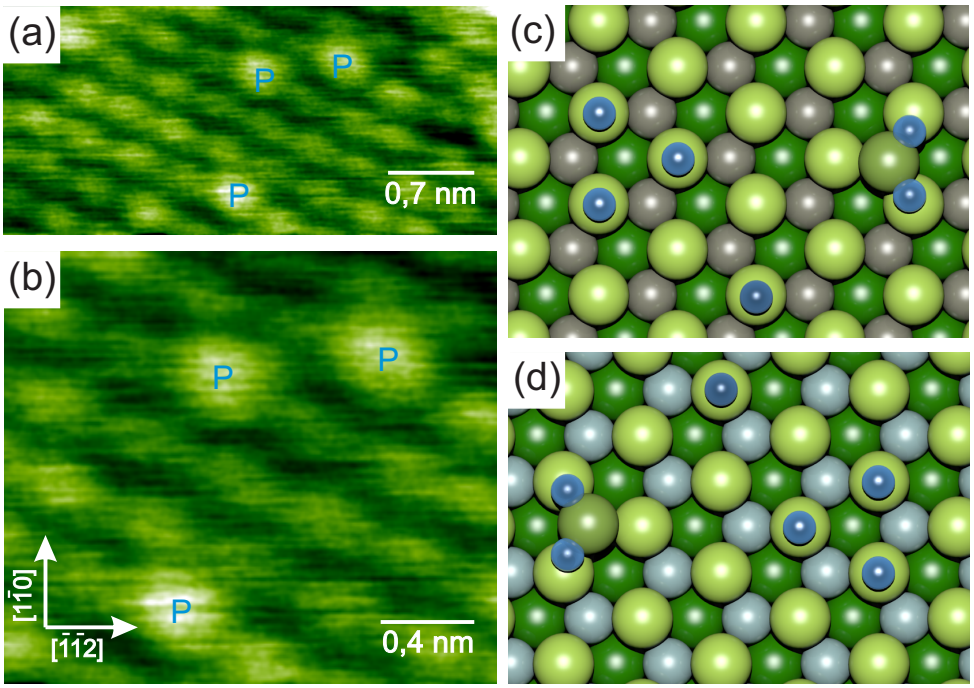

Fig. 5.13: (a) NC-AFM topographic images revealing protrusions ("P") directly placed on atomic positions and hence assigned to single hydroxyls. The measured height of the protrusions is 30 pm. (b) Enlarged cutout of frame (a). (c,d) Illustration of single hydroxyls, hydroxyl trimers and a water molecule on the CeO_2 (c) and Ce_2O_3 (d) surface. Single hydroxyls are placed directly over an oxygen position, hydroxyl trimers on top of subsurface oxygen positions and water molecules on top of cerium positions. Color code: light green= surface O; gray=Ce^{4+}, light gray=Ce^{3+}, dark green subsurface O and blue=H.

A measurement series showing a very high coverage of protrusions on the ceria film surface is presented in figure 5.14. In series (A), the topographic images are shown and in (B) the corresponding frequency shift images. The scanning direction is indicated by the white arrows. The series is carried out several months after the last bake out of the UHV chamber. During this time period dozens of loadlock operations are done where despite of careful cleaning and bake out of the loadlock, additional residual gas and also water migrate into the UHV chamber. Note, image series that are taken directly after a bakeout do not show such high amount of adsorbates.
The series reveal 24 successively recorded images with atomic resolution which are recorded over a time period of two hours (each image takes approx. 5 minutes). Due to stronger lateral drift at the beginning of the series, manual position corrections are made for the images (b),(d) and (f) to stay in place. After image (f), the lateral drift becomes very low and is stabilized at the end of the series at approx. 80 pm/min. The measurement is started approximately two hours after the last annealing cycle at vacuum conditions of $3{\cdot}10^{-10}$ mbar. All images are measured in the quasi constant height mode where either in the recorded topography signal and in the frequency shift signal atomic resolution is achieved. The frequency shift set-point is carefully increased during the series to obtain an enhanced resolution and to compensate drift in z-direction. During the complete series, electrostatic interactions are compensated by activating the KPFM loop. The images

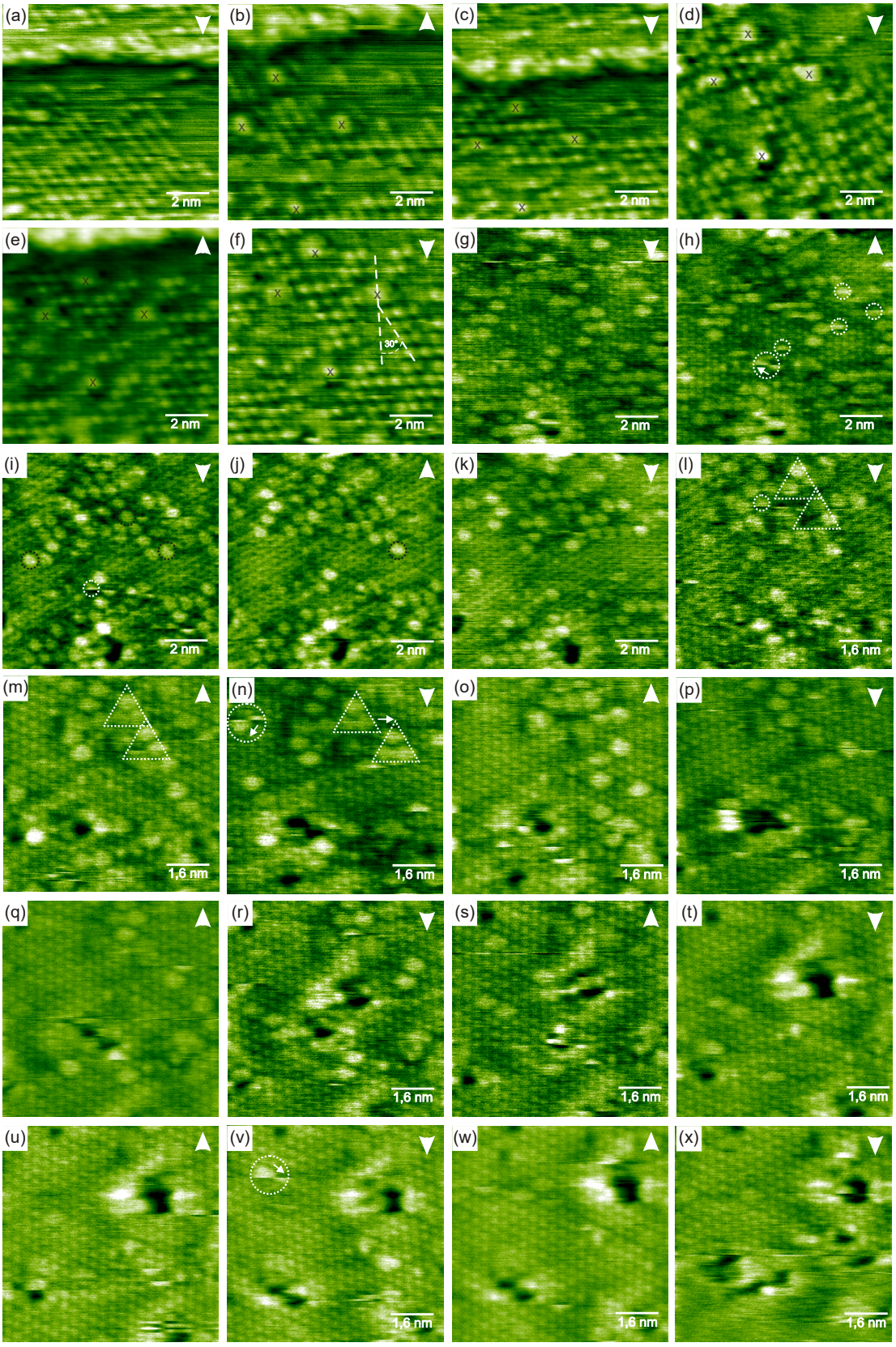
(a)
2 nm
(b)
2 nm
(c)
2 nm
(d)
2 nm
(e)
2 nm
(f)
30°
2 nm
(g)
2 nm
(h)
2 nm
(i)
2 nm
(j)
2 nm
(k)
2 nm
(l)
1,6 nm
(m)
1,6 nm
(n)
1,6 nm
(o)
1,6 nm
(p)
1,6 nm
(q)
(r)
1,6 nm
(s)
1,6 nm
(t)
1,6 nm
(u)
(v)
1,6 nm
(w)
1,6 nm
(x)
1,6 nm

Fig. 5.14: (A)

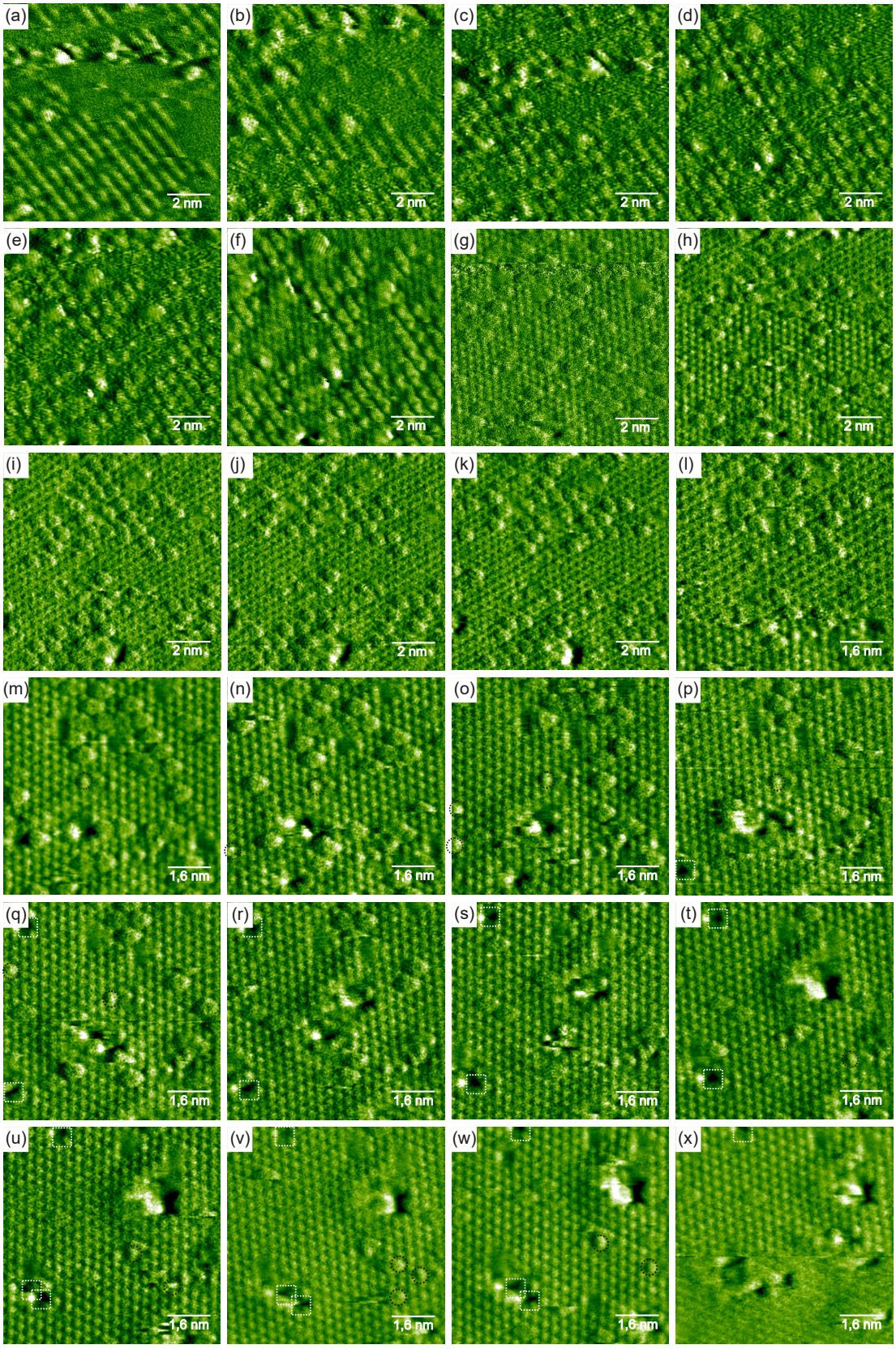
(a)
2 nm
(b)
2 nm
(c)
2 nm
(d)
2 nm
(e)
2 nm
(f)
2 nm
(g)
2 nm
(h)
2 nm
(i)
2 nm
(j)
2 nm
(k)
2 nm
(l)
1,6 nm
(m)
1,6 nm
(n)
1,6 nm
(o)
1,6 nm
(p)
1,6 nm
(q)
1,6 nm
(r)
1,6 nm
(s)
1,6 nm
(t)
1,6 nm
(u)
1,6 nm
(v)
1,6 nm
(w)
1,6 nm
(x)
1,6 nm

Fig. 5.14: (B)

.

Fig. 5.14: (A) Topographic NC-AFM measuring series. **(B)** Corresponding frequency shift series. The scanning area of the images (a-k) is $(10 \times 10\,\text{nm})$ and $(8 \times 8\,\text{nm})$ for images (l-x). The series shows a very high coverage with water molecules at the beginning that is probably removed by the tip with increasing scanning time. In the topographic images the scanning direction is indicated by the white arrows. Special features are highlighted in the image series where details are given in the discussion.

.

are obtained on the dashed area shown in figure 5.16 where (a) shows an overview scan directly before and (b) directly after the series. The difference between the two images is discussed later. In the beginning of the series (a-c, e) the step edge included in the dashed area is observed again. In order to obtain a better resolution and to avoid crashing into the step edge the scan area is moved a few nanometers away from the step edge onto the terrace. The protrusions appear with a triangular shape and a blurred contrast and lay on three surface oxygen atoms as shown in the enlarged frames in figure 5.15. From the previous discussion and with the comparison of NC-AFM images on water covered ceria crystals surfaces [127] we assign the coverage as water molecules and that the ceria surface has undergone a phase transition to the A-type of Ce_2O_3 [20], as water molecules must be placed on cerium lattice positions(see figure 5.13 (c,d)).

In the first images of the series four well recognizable points on the surface are marked with an "x" allowing a tracking of changes relative to this positions. We first observe that the water coverage appears mostly ordered in rows rotated by 30° to the oxygen rows of the cerium surface (f) which are next nearest neighbor cerium positions. The coverage is relatively stable. At the beginning, some molecules rearrange which is especially noticeable during the images (d-f) where in between the area of the highlighted points some molecules change their positions. When following the series, it is obvious that the ordered structure of the coverage changes and to some extend is completely disordered. This pro-

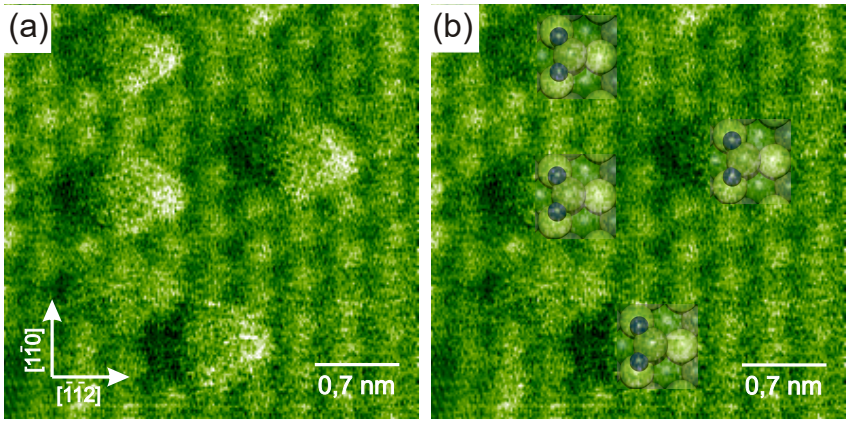

Fig. 5.15: (a) Enlarged frame of figure 5.14 **(B)** (o) revealing the triangular shape and blurry contrast of the particles pointing in the $[\bar{1}\ \bar{1}\ 2]$ direction. (b) Illustration of physisorbed water placed on the particles. The placement of water on the surface is only possible for a rotation of 180° to match cerium positions [105, 130] which suggests that the observed surface has undergone a phase transition to 1×1 A-type of Ce_2O_3.

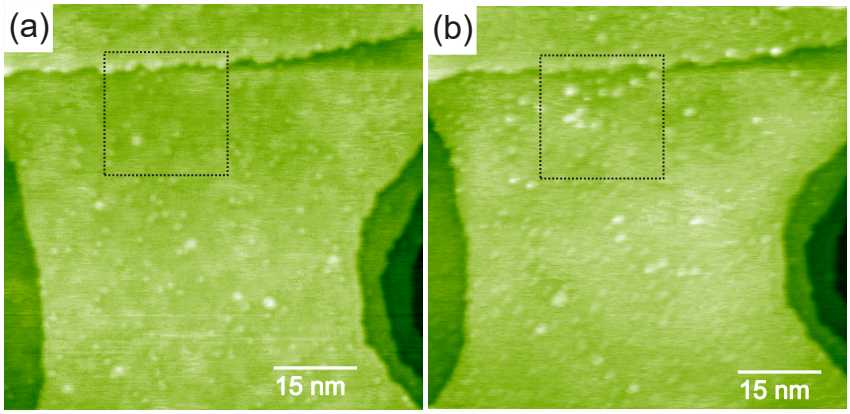

Fig. 5.16: Topographic NC-AFM image showing the terrace on the ceria film surface before (a) and after (b) the measurement series which is presented in figure 5.14. The dashed square is the estimated scan area of the series. The overview scan exhibits an excellent contrast with very sharp step edges and some irregularities.

cess starts at the beginning of image (g), where the line time is slightly decreased and the frequency shift set point is slightly increased. The change in the image parameter settings leads to a better resolved 1×1 surface reconstruction but may provoke disordering of the water coverage due to the stronger tip-surface interaction as result of the higher Δf set point. We speculate that most likely the changes of the water coverage are caused by the tip.

Another feature are water molecules that are imaged only fragmentary. Some of them are highlighted in image (h) with white dashed circles. Three possible causes can lead to these fragments. Water molecules that just adsorb on the scanned surface area, molecules that are removed during the measuring or molecules that are pushed or pulled by the scanning tip. The later can be observed in image (h), (n) and (v) where the white arrow indicates the displacement of the water molecules which is in opposite direction in those images. The opposite direction is a hint that the movement is not related to the thermal drift. The adsorption and removing of the fragments can be retraced by the fragmentary measured molecule in (n) which is not observed in the previous image (m) and disappears again in the following image (o). The described observations lead to the assumption that the changes of the water coverage are caused by the tip. The tip probably pushes or pulls the molecules on the surface or molecules adsorb on the tip apex where they can stay or move back to the ceria surface again.

Another interesting feature is observed in images (l-n). The triangles highlight an area that include three water molecules. In the first image (l), the triangles each include only two molecules and one unoccupied position which is located in the upper triangle in the bottom right and in the lower triangle in the bottom left. In the following image (m) in the upper triangle the free position is now occupied with a water molecule while in the other triangle a fragmentary molecule is observed which is just about to form at the unoccupied position. It stays unclear if these molecules just moved to these positions or newly adsorb there. Also two additional molecules are now observed beneath the lower triangle that are probably related to the molecules observed some atomic rows left in the previous image (l). The fragmentary molecule is fully observed in the next image (n)

accompanied with a shift of the lower triangle two atomic rows in [$\bar{1}$ $\bar{1}$ 2] direction. The interesting observation is that the three particles in the triangle moved together. In the following image (o) the triangular compositions are dissolved and of the lower triangle only the particle in the bottom left is still observed but directly neighbored to a new located molecule that in the previous image already appeared as a fragment and may have provoked the dissolution of the triangular composition. Overall, these observations indicate a specific interaction among the molecules.

As discussed, the identification of the water molecules is based on a phenomenological approach based on the previous results of the NC-AFM study on water on a Ceria crystal (111) surface [127]. The main difference is that we assume to prepare our film surface in the 1×1 A-type of Ce_2O_3. We also do not expose our surface directly to water, while in the previous study the ceria surface is exposed to different amounts of water with a maximum pressure of $1 \cdot 10^{-9}$ mbar for up to 6 hours. We only anneal the ceria film at 1050 K in UHV where the maximum pressure of $8 \cdot 10^{-10}$ mbar is only reached at the highest annealing temperature and the series is recorded directly after the sample is cooled down at a pressure of $4 \cdot 10^{-10}$ mbar. Hence, in our measurement series the expected amount of water should be much less and also the time period where the water can adsorb on the surface is much shorter. A possible explanation for the unusual high water coverage of the film surface observed in the series is the long time after the last back out. Also water molecules might migrate on the tip and the cantilever adsorbing on the sample surface during the approach. However, on single crystal surfaces such a high amount of water was not observed under similar vacuum conditions.
At the end of the series, the imaged surface area is almost free of water molecules as clearly visible in the images (t-x). The overview scan in figure 5.16 (b) is measured 10 minutes after the last image (x) of the series. In the estimated scan area, the irregularities are slightly more pronounced in comparison to the measured image directly before the series beginning. We speculate that the tip pushed most of the water molecules from the scanned area during the two hours of measuring and which lead to the additional observed irregularities. However, also outside the scan area of the series, changes in the irregularities are visible in the overview images but the amount of irregularities increases not significantly .
Among the water molecules, the series also shows surface vacancies and some protruding atoms which are highlighted in the Δf images in figure 5.14 (B). Two single vacancies that are stable over a time period of 30 minutes are highlighted with white dashed squares in the images (p-x). These vacancies do not change their position during the measurement and their movement observed in the series belongs only to the general thermal drift.
Some protruding atoms are highlighted by the black circles in the images (n-q) and (t-w). In comparison to figure 5.13, we assign these protrusions to single hydroxyl species. To some extent these hydroxyls are stable but around their location surface irregularities appear which look like vacancies as observed in image (r, s) and in (x). When comparing image (w) with image (x), we find that at the location of the two highlighted hydroxyls in (w), a new surface vacancy is found in (x). This may corroborate the recently suggested correlation between vacancy formation and hydroxyl species [111].

This section showed that the ceria film is rich of surface irregularities that can be assigned to surface oxygen vacancies, water or hydroxyl species. Even the preparation under relative good UHV conditions cannot exclude a water contamination of the ceria surface. The interpretation of observed irregularities is more difficult on the film compared to single crystals as always a reduction to the 1×1 A-type of Ce_2O_3 has to be considered.

These results are very interesting but the water dosage was not conducted in controlled manner. Hence, a experiment with a controlled water dosage should be performed as proof. A dosage with molecular hydrogen would allow a direct comparison of the results with previous experiments on ceria crystals [105,126,128]. Further high reactive hydrogen dosage for reducing the surface and reaction experiments with atomic oxygen interacting with hydroxyls on the surface may give new insights in ceria surface reaction mechanisms.

5.2.6 Comparative analysis of the surface morphology of Si-supported ceria films and two different ceria crystals

In section 5.2.3 NC-AFM imaging on single crystals has already been introduced and in [18, 108] some general similarities and differences between the film and the bulk material are discussed.So far, these results document only the older crystal samples SCO (Crystal Guru, Florida, USA) which are, as explained in section 4.3.2, in a bad condition and not sufficient for future use anymore.

Compared to the film, the morphology of the SCO crystals equals in several points: both show a terrace structure separated by one or several TL height step edges while merely on the crystal more several TL high steps are found [108]. To collate the NC-AFM measurements on both crystals with the films first some general observations not yet described are presented.

As discussed in [18], the films can be measured on much larger scan frames than the crystal surfaces due to the much less rough surface even in the as-prepared condition. Although, some measurements show only the typical roughness of the pyramidal or terrace structure, a few large scale images exhibit some raised areas. An example is given in figure 5.17. Here, the AFM image (a) is measured after a regular annealing cycle. The surface clearly shows several raised areas that are two to six nanometers above the average height as indicated by the inserted profiles in (c). The surface structure on the areas is not affected. Interestingly, the KPFM image has a height independent contrast for these areas of 120 to 150 mV. Also only in the topographic image, less visible raised areas appear with a distinct Kelvin contrast indicating an equal composition of these areas.

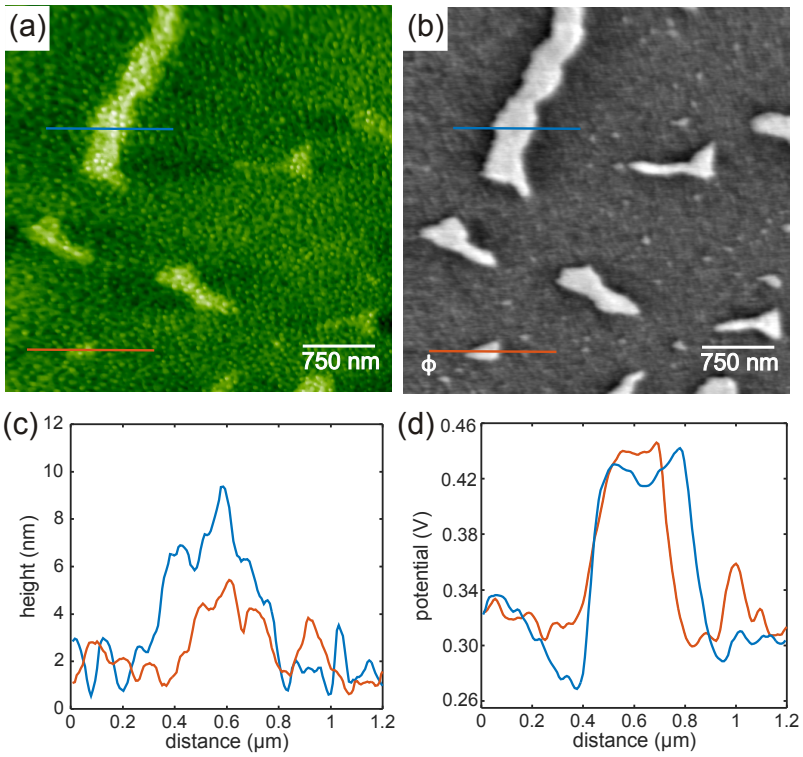

Fig. 5.17: (a-d) NC-AFM topographic image and KPFM image on the ceria film M1969 with corresponding line profiles. On large scales (>1 µm) we observe some irregularities in width of several hundred nanometers which are 2 to 6 nm above the average surface height. These irregularities are on local 120 to 150 mV higher potential compared to the rest of the surface. As clearly visible, all the irregularities have the same local potential although they differ in height by 50 percent.

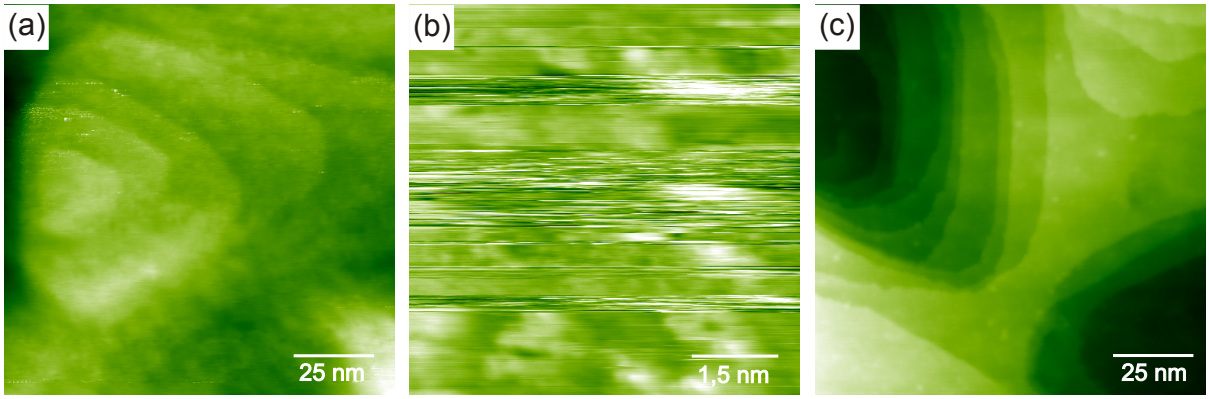

Fig. 5.18: (a-c) Topographic images measured on the film M1969. The images were recorded in chronological order with the same tip revealing strong contrast changes. We speculate that the tip randomly picks something up which results in a decreased contrast where steps are just still visible.

From the images it cannot be revealed if these features are a random contamination or defects created during film growth. However, these features have to be considered during NC-AFM measurements as the scanning along the border of these areas might lead to a false interpretation of the surface roughness.

In the previous sections it was pointed out that obtaining images with atomic resolution on the film samples is not straightforward and more difficult and time consuming than on the surface of our old ceria crystal samples. One reason for this are the irregularities (compare section 5.2.1 figure 3 frame (g) and (h) of the publication and section 5.2.2 figure 2 frame (d) of the publication) that are observed on the surface [18,19]. The irregularities are not related to a non-sufficient surface preparation but seem to be partly affected by the tip-surface interaction. This speculation is supported by our observation in many measurements where a lot of tip changes appear that results in different image qualities. One example is presented in figure 5.18. The evaluated topographic images show three states of a measurement series with a tip that exhibits only a weak resolution after some measurement time (a), although no crash of the tip happened. Step edges can hardly be resolved and from the optical impression, the surface is not free of contaminants. In image (b), the surface is measured with this tip on a small scale with an increased frequency shift set point. There are some clearly visible contrast changes yielding a strong distortion of the recorded data and an overall unstable measurement. Sometimes, this unstable behavior suddenly ends and the contrast becomes much better as shown in image (c). Now the surface structure is resolved in detail and step edges and terraces have a very sharp contrast. The formerly resolved irregularities are only present in a minor amount and the surface appears overall relatively clean and flat. In this state atomic resolution imaging is possible but an increasing frequency shift set point very fast leads to unstable behavior again and results in the loss of detailed resolved structures. Most likely due to a certain tip-surface interaction, the tip picks up and drops something from the surface causing such complications during measurements. One could speculate that the Si material of the tip or ceria material that has been picked up by the tip interacts with the surface oxygen of the ceria film. Tip changes leading to a resolving irregularities

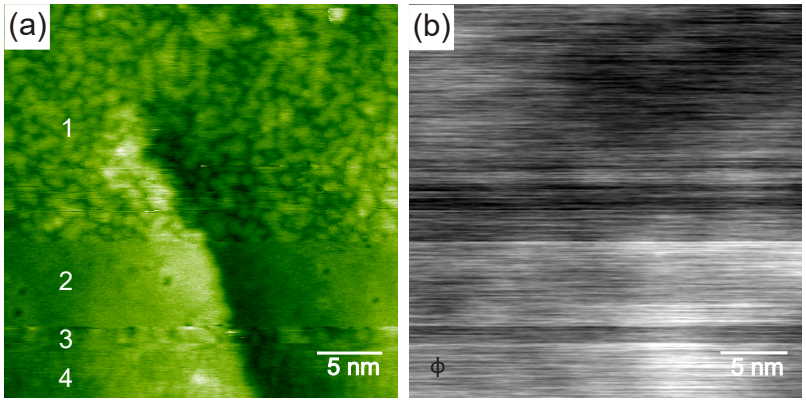

Fig. 5.19: (a) NC-AFM topographic image on the ceria film M1969 exhibiting a surface morphology strongly depending on the tip condition. (b) Corresponding KPFM image. The topographic image reveals a screw dislocation with a step climbing on TL. In the image, four tip changes (1-4) can clearly be distinguished. (1) The surface appears completely covered with irregularities which changes suddenly (2) to a very smooth and clear looking surface where on the terraces only some very small holes can be observed. Then for a few scan lines, the surface appears completely covered again (3) but after another tip change, the terraces are clear again but not as smooth as in the middle (4). The tip changes also can be observed in the KPFM image where the four different tip conditions effect the measured potential in the range of $\pm\,100\,\mathrm{mV}$.

are shown in figure 5.19 (a). Here, a screw dislocation is observed in the topographic image. A total of four tip changes can be seen in the image. First, the terrace seems to be fully covered by irregularities but in the middle of the image, the surface appears clean without any irregularities. To the bottom of the image for some scan lines the irregularities are resolved again until with a further tip change the surface looks smooth again but exhibits still some small irregularities. The tip changes are also reproduced by the KPFM image (b) and lead to potential variations of $\pm 100\,\mathrm{mV}$ indicating modifications of the tip apex, as described in ref. [124]. However, these effects must be considered during image interpretation. Otherwise observed irregularities related to scanning artifacts could be misleadingly interpreted as surface contamination.

Irregularities are also observed at atomic resolution as shown in the topographic and the corresponding frequency shift image in figure 5.20 (a, b). The image exhibits a 1×1 surface partially covered with some small random shaped protrusions. As the atomic structure is resolved in the same scanning lines as the irregular protrusions we can exclude that the irregularity is in this case a scan artifact.

Another but rare observation is the manipulation of the clean surface during measurements when increasing the Δf set-point. One example is presented in figure 5.20 (c, d). The images show a hexagonal island on a larger terrace. All steps in the image have one TL height. In (c) the borders of the hexagonal island are undamaged and the surface appears to be clean. Image (d) was taken after several minutes of measuring on the island with constantly increased Δf set-point. As a result, a small hole is formed in the island

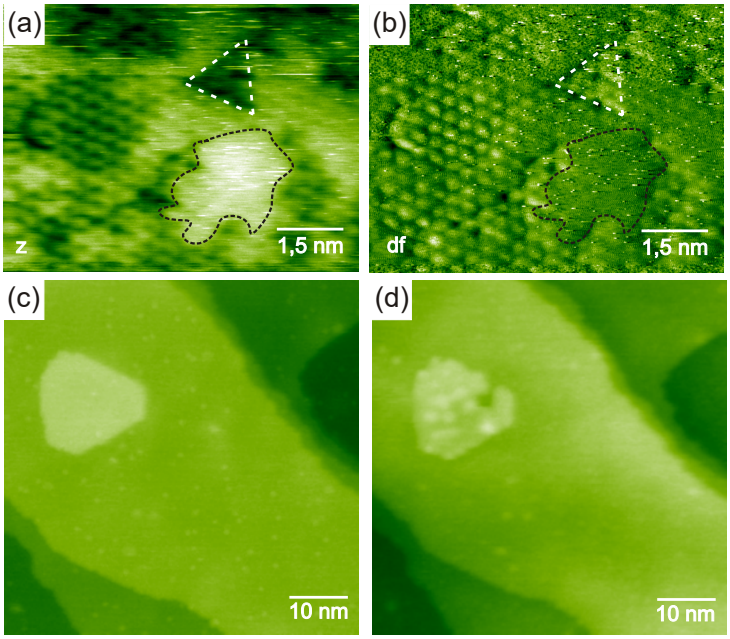

Fig. 5.20: (a,b) NC-AFM images on the ceria film M1969 revealing atomic scale irregularities. The irregularity appears as a randomly shaped feature with a height of 100 to 150 pm and a width of 1.5 to 2 nm. The atomic structure of the irregularity itself cannot be resolved.
(c,d) NC-AFM images revealing surface manipulation. On top of the main terrace, a hexagonally shaped protrusion with TL height is visible. The same area is imaged after a few measurements with slightly increased Δf set point, whereby the protrusion now shows a small hole and some material is deposited on the surface.

and material is deposited on the island. Probably the tip has pulled out several surface particles and then spread them on the island.

The surface properties of the old crystal samples SCO have been discussed in detail in [65, 73, 83, 104, 105, 108, 110, 126–128]. The terraces on the SCO samples are smaller compared to the ones on the film and often have a width of only 10 to 20 nm. The crystals allow a higher annealing temperature at 1200 K for preparation and in contrast to the film, much less irregularities are observed on their surface. Although, the step edges appear equal in topographic images, KPFM imaging reveals different potentials for step edges on the film compared to step edges on the bulk.

From an experimental point of view, it is much easier to achieve atomic resolution on the old crystal samples. In figure 5.21 an high resolution image on SCO sample is presented. The frequency shift image exhibits a good atomic resolution with a signal of up to 3,5 Hz difference between atomic rows as shown in the cross section profile presented in (c). This value is about three times higher than the usual Δf values we could achieve for measurements on the film samples M1969. The same observation is found for the corresponding KPFM image shown in (b). Here, the atomic positions in the lattice are very well distinguishable with a potential variation of up to 400 mV as outlined in the profile shown in (d). The discussed distortions of the film during measurements with slightly increased Δfset point are also not observed during measurements on the crystal. In fact, the frequency shift set point can be increased to a level where a strong atomic contrast is achieved and atomic resolution can be kept for the time of a complete measurement series typically lasting several hours.

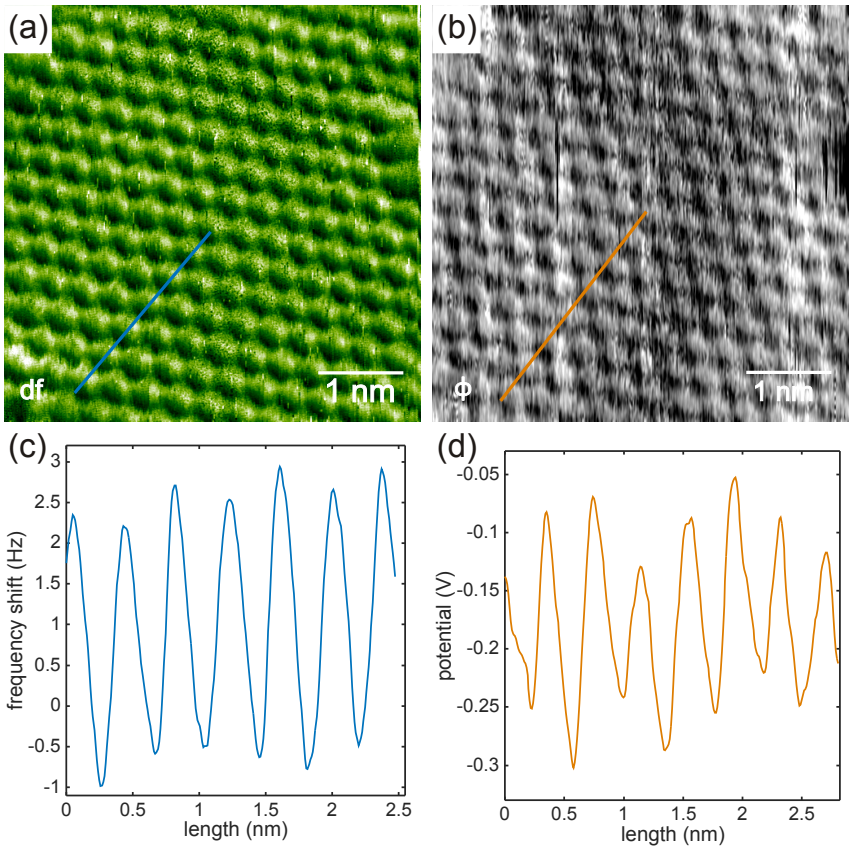

Fig. 5.21: (a,b) NC-AFM and KPFM measurements with and on the ceria SCO sample showing atomic resolution. (c,d) Corresponding profiles. The frequency shift image exhibits excellent atomic resolution with a frequency shift difference of approx. 3 Hz for each atom The Kelvin image also shows good atomic resolution with electrostatic potential variations of up to 400 mV.

The crystal surface has a higher average roughness than the film surface whereby the maximum scan area for NC-AFM measurements is usually limited to less than 500 nm × 500 nm. However, imaging with atomic resolution is possible on much larger scan areas compared to the film. On larger terraces, often scan frames of 20 nm × 20 nm can still be imaged with atomic resolution. Even the preparation of the SCO samples seems not to be so significant as pointed out in the following experiment. A sample attached to a sample holder was stored two years under ambient conditions. The sample experienced many typical preparation cycles. We expected that the long storage would have led to a complete surface contamination. Figure 5.22 shows the surfaces after annealing at a moderate temperature of 420 K for one hour. Usually such a low annealing temperature is not nearly sufficient for the surface to be prepared in a way that it is clean enough for atomic resolution imaging.

In (a) a topographic overview scan is presented and in (b) the measurement area from the images (c) and (d) is highlighted. For the crystal surface, the terraces are exceptionally large but the most surprising fact is the relative low coverage with contaminants considering the low annealing temperature. In image (b) the contaminations are observed at step edges and at vacancy positions on the terrace while still most of the area on the terrace is free of any contamination and exhibits an atomically flat surface. The images (c) and (d) demonstrate that it is possible to achieve atomic resolution on a very large scale of 35 nm×35 nm also across two step edges which is remarkable after the simple preparation. The high resolution images clearly show that the contaminants are all located at the step edges and at defect positions on the surface. We speculate that the low

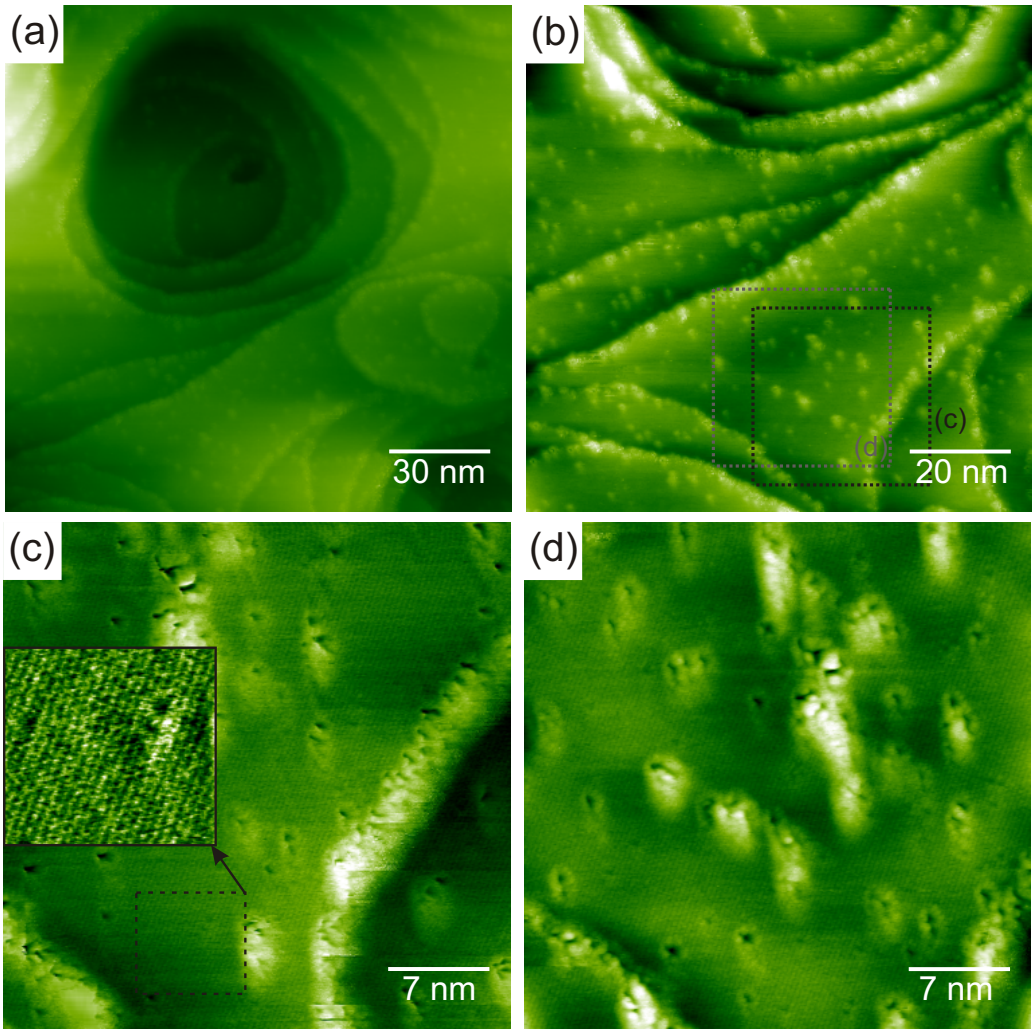

Fig. 5.22: (a-d) NC-AFM topographic measurements on a SCO sample after annealing at a low tempearture of 420 K. The sample was stored 2 years under ambient conditions. A terrace structure rich of step edges can be seen. Considering the low temperature preparation, the observed amount of contaminants is low and atomic resolution images (see enlarged frame insight(c)) on large scales of 35 nm × 35 nm reveal that contaminants are placed at vacancies and the step edges.

annealing temperature is not sufficient to remove many contaminations resulting from the storage but allows them to diffuse on the ceria surface where they accumulate at defect and step edge positions.

However, this experiment shows that the crystal surface can be measured with atomic resolution on large scales even after a minimal preparation whereby the rule of previous preparation cycles has to be considered. For the film surfaces, even after storage in UHV for only a week after the last preparation, the annealing at such low temperature will not result in surfaces clean enough for atomic resolution imaging indicating a much higher surface reactivity. A possible explanation for this observation could be the difference in the reduction state. We speculate that the high oxygen reservoir of the bulk material lead

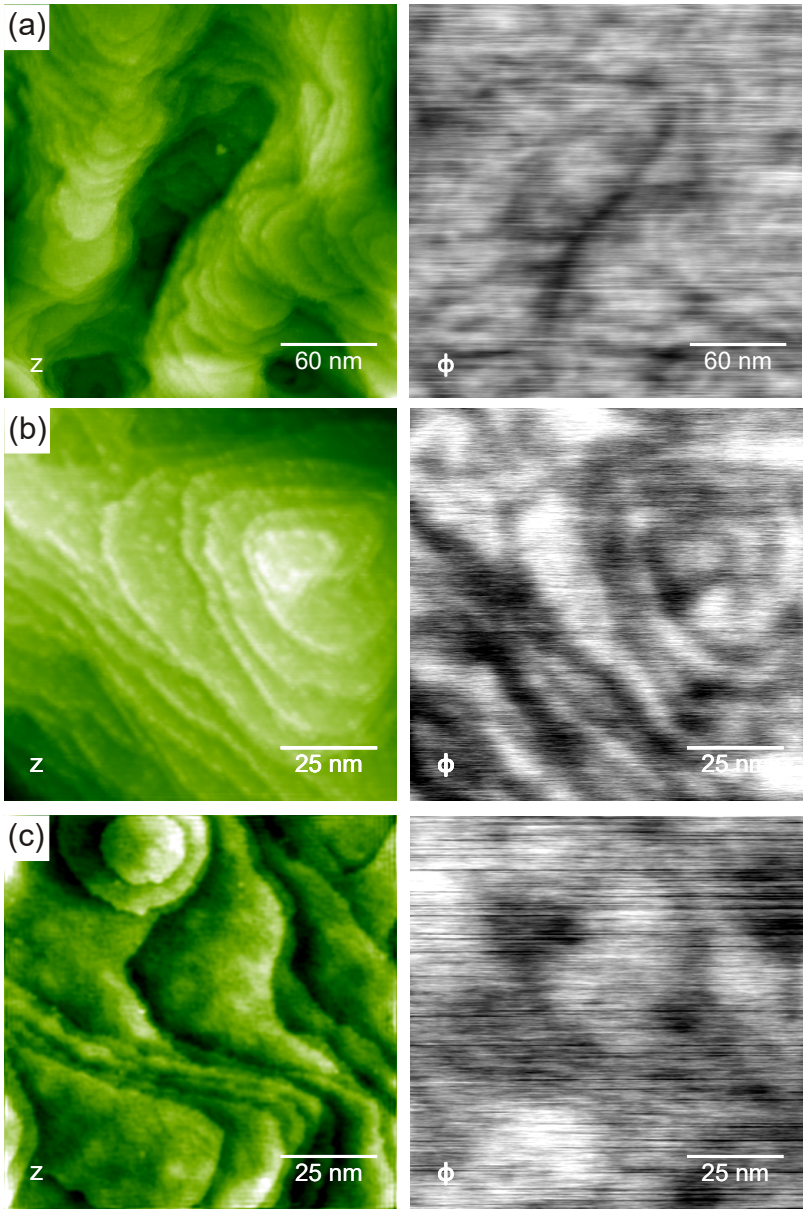

Fig. 5.23: (a-c) NC-AFM and KPFM measurements on the SCN sample. The topographic images are measured after several annealing and sputtering cycles at 1100 to 1200 K. The surface morphology is represented by many small terraces with a width of 5 to 30 nm separated mostly by single TL step edges. The steps are rounded and on the terraces some irregularities can be observed. The corresponding KPFM images reveal a weak contrast. Step edges are on a lower potential than the terraces. The terraces themself show slight potential variations similar to the findings on the ceria film samples.

to a less reduced surface.

As the old crystal samples had produced excellent results and it has been easy to achieve atomic resolution, we expected similar results for the new crystal samples SCN (Surfacenet GmbH; 48432 Rheine, Germany).
The preparation with sputter and annealing cycles at temperatures in the range of 1100-1200 K in UHV follows the same procedure as for the SCO samples. For the first annealing cycle the temperature is held at lower temperature of approx. 400 K as the crystal degases strongly after the first UHV transfer and the pressure rises up to 10^{-6} mbar. The crystal is annealed at least three times at this temperature for 8 hours before the pressure decreases to an acceptable level ($<10^{-5}$ mbar). Then, the temperature is stepwise increased until the target temperature of 1100 K is reached. This process takes another 8 hours. Similar

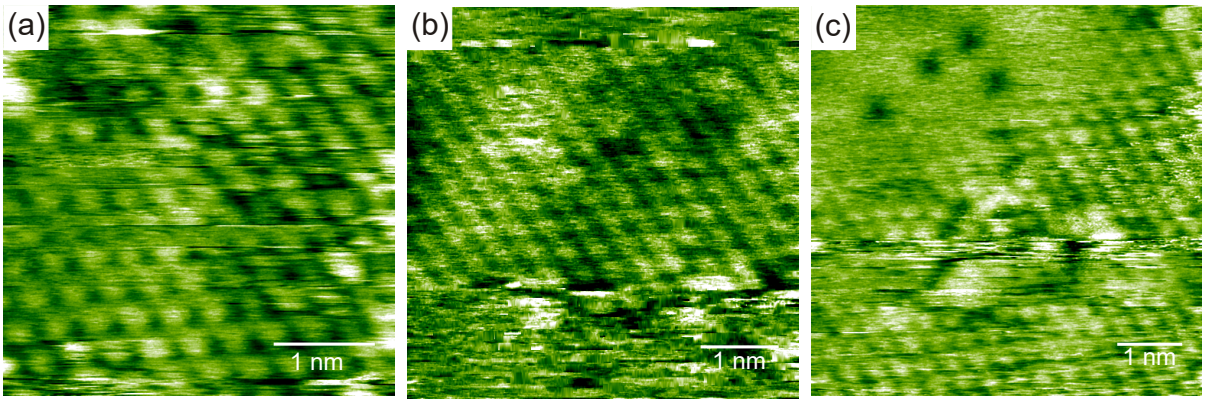

Fig. 5.24: (a-c) NC-AFM measurements on a SCN sample exhibiting atomic resolution. The topographic images reveal a 1×1 surface periodicity most likely corresponding to CeO_2. The atomic resolution is relative weak and measurements are usually unstable due to a high amount of defects and irregularities.

to the SCO samples, the surface has a high roughness and the maximum useful scan size is approximately 300 nm × 300 nm. But also on small scales, sometimes height differences of several ten nanometers appear hampering NC-AFM measurements. Because of this, the scan area must be changed sometimes after the approach. In figure 5.23 topographic images are shown that are representative for the resulting surface morphology. Images (a-c) reveal a terrace structure comparable to the one of the SCO and the ceria film M1969 samples. The terraces are relatively small and have a width of 5 to 30 nm. The surface is rich of step edges which are mostly 1 TL high but also some step edges with several TL height are observed. From this perspective, the surface seems to be identical to the SCO crystals but there are some variations. The step edges are rounded like the steps on the film and not straight as on SCO crystals. The surface is not nearly as clean as on the SCO crystals. The images exhibit some clearly visible irregularities placed on the terraces. The KPFM images also reveal some differences. On the terraces, potential variations are found and step edges appear with a locally lower potential. Interestingly, these observations equal more to the measurements on the film surface. But even compared to the films, we observe more irregularities on the SCN samples. It is, therefore, not surprising that atomic resolution imaging is extremely difficult to obtain. Some of the few images showing atomic resolution are presented in figure 5.24. The topographic images (a-c) all show the 1×1 surface but also a lot of defects. Even on small areas of 4 nm × 4 nm, no image without distortions caused by irregularities could be measured. All of the images showing atomic resolution are like the presented images where only a few lines are of better quality and often like in image (b) the resolution is partially lost. In conclusion, the SCN samples do not provide the expected surface quality known from the SCO samples. The reasons for this are speculative. The SCN samples are thicker than the SCO samples and this could lead to a slightly inaccurate annealing due to a higher temperature gradient but it is unlikely that this would lead to such strong irregularities.

A discussion with the crystal vendor revealed that the best surface part should be the area which usually appears with a deep black color as this area appears more flat under a microscope. For the sample shown in figure 5.25 this area is highlighted with the green

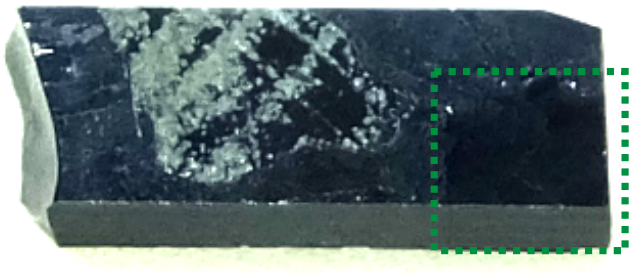

Fig. 5.25: Photograph of one of the SCN samples. The surface of the sample shows some areas with an optical visible roughness. Only the green highlighted area appears with a deep black color and seems to be the best area for NC-AFM imaging but due to the sample holder design only the middle of the surface area can be used for measurements.

dashed box. Unfortunately this area is located at the border of the sample which is inaccessible d for NC-AFM measurements.
An explanation from the chemical point of view could be the fluorine impurities in the SCO samples mentioned in section 4.2. The fluoride impurities which are found in the SCO samples can be implemented into the surface and interpreted as vacancies in STM measurements [109]. For NC-AFM and KPFM the fluoride atoms at the surface would be probably indistinguishable from oxygen atoms. Surface vacancies could be filled up by fluoride impurities and in a NC-AFM measurement, a perfectly defect free surface would be observed. Hence, the fluoride impurities could be a reason for the much more solid measurements possibilities on the old crystals. So far, XPS measurements proved the absence of fluoride impurities in the films. For the new SCN bulk crystals XPS measurements have to show if fluorine impurities can be found in the surface.
The comparison of the three different cerium oxide samples shows that the bulk like film and the SCO and SCN samples have a lot of similar surface properties but also exhibit substantial differences. All samples show a surface with a terrace structure separated by TLs but while the crystals only exhibit small terraces, the terraces on the film surface are much larger and overall the film has a significantly lower roughness. This makes the films to the ideal model system for very sensitive scanning probe techniques. However, on the atomic scale, the films show a lot of irregularities and a difficult to control tip-surface interaction which could be related to a higher surface reactivity compared to the bulk crystals. Also the surface reduction affects the films stronger than the crystals which have a much larger oxygen reservoir. We speculate that the films are prepared in the 1×1 Ce_2O_3 surface at UHV conditions while the crystals exhibit under the same preparation conditions mostly the 1×1 CeO_2 phase. This could be one reason for the much easier possibility of atomic resolution on the crystal surface. Generally atomic resolution imaging is much more straightforward on the crystals. Surprisingly this is not the case for our new replacement crystals which also show not well understood irregularities and defects.

The above discussed results for the new SCN crystals represent the first measurements on these samples. For a future perspective a detailed XPS analysis have to proof the absence of impurities in the SCN samples. However, the examination of crystals that are controlled doped with flourine may shed light on the controversial discussion on impurities in the old SCO bulk crystals. For NC-AFM measurements the preparation procedure of the samples has to be improved (e.g. longer annealing time). The examined crystals

have been the first produced ones from the vendor and the growth process may have been improved since then.

6 Conclusions and ongoing work

The ceria samples used in this work have to be considered as model systems and the basis for a deeper understanding of the widely used catalytic capabilities of this material. In this context, the ceria films are introduced as a alternative model system for NC-AFM studies while the single crystals where already established in previous work [65, 72, 119]. One major goal was the imaging with atomic resolution on the cerium films which turned out to be more complicated than expected from our experience with old ceria crystals. Repeatable atomic resolution imaging could be established on the film surfaces and exploring atomic surface structures yielded new surprising findings.

One of the key findings is the preparation and imaging of surface reconstructions representing reduced states of cerium oxide. The film could be prepared in five different surface states from the fully oxidized state CeO_2 to the fully reduced state Ce_2O_3. Our measurements lead to the discovery of two ceria phases, namely Ce_3O_5 with $\sqrt{3} \times \sqrt{30}\ R30^\circ$ and Ce_3O_5 with the unusual oblique $\sqrt{7} \times 3\ R30^\circ$ stoichiometry which were not reported before elsewhere. Additionally, the more prominent ι-phase (Ce_7O_{12}) could be imaged for the first time with a direct image technic and we showed that some phases can exist together on same terraces. Extensive DFT calculations revealed that the reconstructions can be derived by slices of bulk phases placed on the CeO_2 film whereby some phases like the oblique phase can only be stabilized on the film and cannot be stabilized in the bulk. For all reconstructions, energetically preferred surface models were derived in very good agreement with the experimental results. Due to the nature of the surface reconstructions with their regular oxygen vacancies, the knowledge about their stoichiometry is essential for understanding the fundamentals of a catalytic substrate often used as oxygen reservoir.

We showed that the ceria film surface can be prepared in a pyramidal wedding cake like morphology or in large terraces, both revealing a rich amount of TL height step edges which are important reactivity sites in catalytic reactions [8, 131]. Further, we can fully control the reduction state of the ceria film by annealing in UHV or by annealing in a controlled oxygen atmosphere as proven by LEED, XPS and NC-AFM measurements [19, 93, 94].

Beside regular atomic structures, surface vacancies, water molecules and hydroxyl species are frequently observed which we assign to the high reactivity of the film. Even under UHV conditions, our measurement showed that more water is located on the film surface than on a single crystal which is exposed to water with a pressure one magnitude higher. Also dislocations found on the surface of ceria crystals and films have been identified. The comparison reveals that the shape and amount of dislocations is similar on the ceria film and crystal. Screw dislocations connecting several different terrace levels on the surface are frequently found on the crystal and film. These dislocations are probably related to thermal stress during production and post-processing like annealing.

Another aspect of this work was the comparison of the ceria film samples to two different bulk ceria crystals (SCO, SCN). The thick film has similar but also different properties than the single crystal. This is most pronounced for the described reconstructions on the film surface that were never observed on the bulk crytstals in previous works but also in the different reactivity to residual gases in UHV. The comparison of the SCO and SCN crystals showed that much more irregularities are found on the SCN crystals and lead to the question whether the SCO crystals may have been contaminated with flour species as controversially discussed in actual literature [65, 108, 109] resulting in a less reactive surface.

For a short outlook, some research that could not be performed during this thesis but may be lead to further interesting results is summarized.
As mentioned in section 5.2.1, different types of step edges are observed on the ceria surface. KPFM imaging revealed also an opposite contrast for some step edges on the film compared to the crystal. First preliminary calculations by the cooperative partner Matthew J. Wolf (Department of Chemistry-Ångström Laboratory, Uppsala University, Box 538, S-751 21 Uppsala, Sweden) suggest that the contrast observed KPFM is related to two different step edges. Basically type I and type II step edges [85] produce long ranged electrostatic fields relative to the terrace with opposite electrostatic potential from one another. Therefore further measurements on step edges and a more precise theoretical calculation could help understanding this step edges in detail.
The annealing of the ceria films in an oxygen atmosphere was performed by a cooperative partner, as our UHV chamber was not sufficient for annealing in an oxygen atmosphere during the time of this thesis, due to the missing preparation chamber and a sorption pump that could not be separated by a valve and would unlikely pump inserted oxygen. To change this, a modification of the chamber is in progress. Two new turbo molecular pumps and a separable new sorption pump are already installed at the UHV chamber and a new Ion Getter pump will be installed soon increasing the general vacuum quality and allowing the preparation of samples in an oxygen atmosphere. In contrast to the NC-AFM system of our cooperative partner we could achieve atomic resolution in our NC-AFM systems on the film samples. As discussed, the annealing in an oxygen atmosphere installs a fully oxidized $CeO_2(111)$ surface and we expect a surface with less irregularities which can be a starting point for further research. First oxygen annealing preparation cycles have been successfully performed.
For catalytic reactivity often substrates deposited on the ceria surface are of great interest. Metals like gold or platinum are for example promising candidates for catalytic functionality on ceria substrates and especially the aggregation at step edge sites is not measured so far in detail.
The SCN crystals from the alternative source introduced in this work should replace the not any longer available SCO crystals. However, these crystals do not deliver the same high surface quality for NC-AFM experiments and have much more irregularities. As these crystals were one of the first ones produced and the growing process has since then been optimized, there is a potential for receiving better crystals in the future. Further, first measurements with LEEM by the cooperative partner Jan Ingo Flege (University of Bremen-Institute of Solid State Physics- Surface Physics, D-28359 Bremen) revealed that

the crystals have a 1×1 surface of CeO_2 as also observed by our NC-AFM measurements and have regions of different morphology as one may expect already from the optical appearance (figure 5.25). Additional measurements in more detail could be performed to characterize the different regions in the crystal and my help to understand and improve the growth process.

Bibliography

[1] H. C. Yao, Y. F. Y. Yao: Ceria in automotive exhaust catalysts : I. Oxygen storage.
Journal of Catalysis **86**, 254 (1984)

[2] R. Di Monte, J. Kaspar: On the Role of Oxygen Storage in Three-Way Catalysis.
Topics in Catalysis **28**, 47 (2004)

[3] T. Montini, M. Melchionna, M. Monai, P. Fornasiero: Fundamentals and Catalytic Applications of CeO_2-Based Materials.
Chem. Rev. (2016)

[4] A. Trovarelli, C. de Leitenburg, M. Boaro, G. Dolcetti: The utilization of ceria in industrial catalysis.
Catalysis Today **50**, 353 (1999)

[5] A. Trovarelli: Catalytic properties of ceria and CeO_2-containing materials.
Catalysis Reviews-Science and Engineering **38**, 439 (1996)

[6] G. Balducci, M. S. Islam, J. Kaspar, P. Fornasiero, M. Graziani: Bulk reduction and oxygen migration in the ceria-based oxides.
Chemistry of Materials **12**, 677 (2000)

[7] J. C. Conesa, A. Martìnez-Arias, M. Fernàndez-Garcìa, J. Soria: Surface structure and redox chemistry of ceria-containing automotive catalytic systems.
Research on Chemical Intermediates **26**, 103 (2000)

[8] A. Trovarelli, P. Fornasiero: Catalysis by Ceria and Related Materials 2^{nd} Edition . London : Imperial College Press, 2013

[9] S. Hilaire, X. Wang, T. Luo, R. Gorte, W. J.: A comparative study of water-gas-shift reaction over ceria-supported metallic catalysts.
Applied Catalysis A: General **215**, 271 (2004)

[10] M. Kovacevic, B. L. Mojet, J. G. van Ommen, L. Lefferts: Effects of Morphology of Cerium Oxide Catalysts for Reverse Water Gas Shift Reaction.
Catalysis Letters **146**, 770 (2016)

[11] H. S. Gandhi, G. W. Graham, R. W. McCabe: Automotive exhaust catalysis.
Journal of Catalysis **216**, 433 (2003)

[12] G. Adachi, N. Imanaka, Z. C. Kang: Binary Rare Earth Oxides. Dordrecht : Springer, 2004

[13] S. D. Park, J. M. Vohs, R. J. Gorte: Direct oxidation of hydrocarbons in a solid-oxide fuel cell.
Nature **404**, 265 (2000)

[14] E. Miranda, S. Kano, C. Dou, K. Kakushima, J. Sune, H. Iwai: Nonlinear conductance quantization effects in CeO_x/SiO_2-based resistive switching devices.
Applied Physic Letters **101** (2012)

[15] C. Xu, X. Qu: Cerium Oxide Nanoparticle: A Remarkably Versatile Rare Earth Nanomaterial for Biological Applications.
NPG Asia Mater. **6**, e90 (2014)

[16] U. Tumuluri, G. Rother, Z. L. Wu: Fundamental Understanding of the Interaction of Acid Gases with CeO_2: From Surface Science to Practical Catalysis.

Industrial & Engineering Chemistry Research **55**, 3909 (2016)

[17] C. T. Campbell, C. H. F. Peden: Oxygen vacancies and catalysis on ceria surfaces.
Science **309**, 713 (2005)

[18] R. Olbrich, H. H. Pieper, R. Oelke, H. Wilkens, J. Wollschläger, M. H. Zoellner, T. Schroeder, M. Reichling: A well-structured metastable ceria surface.
Applied Physics Letters **104**, 81910 (2014)

[19] C. Barth, C. Laffon, R. Olbrich, A. Ranguis, P. Parent, M. Reichling: A perfectly stoichiometric and flat $CeO_2(111)$ surface on a bulk-like ceria film.
Sci. Rep **6**, 6 (2016)

[20] R. Olbrich, G. E. Murgida, V. Ferrari, C. Barth, A. M. Llois, M. Reichling, M. V. Ganduglia-Pirovano: Surface Stabilizes Ceria in Unexpected Stoichiometry.
The Journal of Physical Chemistry C **121**, 6844 (2017)

[21] G. Binning, H. Rohrer, C. Gerber, E. Weibel: Surface studies by scanning tunneling microscopy.
Physical Review Letters **49**, 57 (1982)

[22] G. Binnig, H. Rohrer, C. Gerber, E. Weibel: TUNNELING THROUGH A CONTROLLABLE VACUUM GAP.
Applied Physics Letters **40**, 178 (1982)

[23] G. Binnig, H. Rohrer, C. Gerber, E. Weibel: (111) facets as the origin of reconstructed Au(110) surfaces.
Surface Science **131**, L379 (1983)

[24] G. Binnig, H. Rohrer, C. Gerber, E. Weibel: 7×7 Reconstruction on Si (111) Resolved in Real Space.
Physical Review Letters **50**, 120 (1983)

[25] G. Binnig, H. Rohrer: Scanning tunneling microscopy.
Surface Science **126**, 236 (1983)

[26] G. Binnig, H. Rohrer: Geburt und Kindheit der Rastertunnelmikroskopie (Nobel-Vortrag).
Angewandte Chemie **99**, 622 (1987)

[27] G. Binnig, C. F. Quate, C. Gerber: Atomic Force Microscope.
Physical Review Letters **56**, 930 (1986)

[28] F. J. Giessibl: Advances in atomic force microscopy.
Reviews of Modern Physics **75**, 949 (2003)

[29] F. J. Giessibl: Atomic Resolution of the Silicon (111)-(7×7) Surface by Atomic Force Microscopy.
Science (Washington, D. C.) **267**, 68 (1995)

[30] M. Bammerlin, R. Luthi, E. Meyer, A. Baratoff, J. Lu, M. Guggisberg, C. Gerber, L. Howald, H. J. Guntherodt: True atomic resolution on the surface of an insulator via ultrahigh vacuum dynamic force microscopy.
Probe Microscopy **1**, 3 (1997)

[31] C. Barth, M. Reichling: Imaging the atomic arrangements on the high-temperature reconstructed a-$Al_2O_3(0001)$ surface.
Nature **414**, 54 (2001)

[32] S. Morita, R. Wiesendanger, E. Meyer: Noncontact Atomic Force Microscopy. Berlin : Springer-Verlag, 2002. – 439 S.

[33] J. V. Lauritsen, M. Reichling: Atomic resolution non-contact atomic force microscopy of clean metal oxide surfaces.
Journal of Physics: Condensed Matter **22**, 263001 (2010)

[34] C. Barth, A. S. Foster, C. R. Henry, A. L. Shluger: Recent Trends in Surface Characterization and Chemistry with High-Resolution Scanning Force Methods.
Advanced Materials **23**, 477 (2011). ISBN 1521–4095

[35] F. J. Giessibl: Atomic resolution on Si(111)-(7×7) by noncontact atomic force microscopy with a force sensor based on a quartz tuning fork.
Applied Physics Letters **76**, 1470 (2000)

[36] F. J. Giessibl, F. Pielmeier, T. Eguchi, T. An, Y. Hasegawa: Comparison of force sensors for atomic force microscopy based on quartz tuning forks and length-extensional resonators.
Physical Review B **84**, 125409 (2011)

[37] L. Gross, F. Mohn, N. Moll, P. Liljeroth, G. Meyer: The Chemical Structure of a Molecule Resolved by Atomic Force Microscopy.
Science **325**, 1110 (2009)

[38] L. Gross, F. Mohn, N. Moll, G. Meyer, R. Ebel, W. M. Abdel-Mageed, M. Jaspars: Organic structure determination using atomic-resolution scanning probe microscopy.
Nature Chemistry **2**, 821 (2010)

[39] Z. Sun, M. P. Boneschanscher, I. Swart, D. Vanmaekelbergh, P. Liljeroth: Quantitative Atomic Force Microscopy with Carbon Monoxide Terminated Tips.
Physical Review Letters **106**, 46104 (2011)

[40] L. Gross, F. Mohn, N. Moll, B. Schuler, A. Criado, E. Guitián, D. Peña, A. Gourdon, G. Meyer: Bond-Order Discrimination by Atomic Force Microscopy.
Science **337**, 1326 (2012)

[41] T. Fukuma, M. Kimura, K. Kobayashi, K. Matsushige, H. Yamada: Development of low noise cantilever deflection sensor for multienvironment frequency-modulation atomic force microscopy.
Review of Scientific Instruments **76**, 53704 (2005)

[42] S. Rode, N. Oyabu, K. Kobayashi, H. Yamada, A. Kühnle: True Atomic-Resolution Imaging of (1014) Calcite in Aqueous Solution by Frequency Modulation Atomic Force Microscopy.
Langmuir **25**, 2850 (2009)

[43] A. Foster, W. Hofer: Scanning Probe Microscopy: Atomic Scale Engineering by Forcesand Currents. Springer Series in NanoScience and Technology, 2006

[44] S. Kalinin, A. Gruverman: SCANNING PROBE MICROSCOPY: ELECTRICAL AND ELECTROMECHANICAL PHENOMENA AT THE NANOSCALE. Springer Series in NanoScience and Technology, 2007

[45] B. Bhushan: Scanning Probe Microscopyin Nanoscienceand Nanotechnology. Springer Series in NanoScience and Technology, 2010

[46] B. Voigtländer: Scanning Probe Microscopy. Springer-Verlag, 2015

[47] S. Silvan, L. G. Villanueva, M. L. Roukes: Fundamentals of Nanomechanical Resonators. Springer, 2016

[48] S. Porthun: PI Controllers, Lock-ins and PLLs. RHK Technology, Inc. http://www.rhk-tech.com/wp-content/uploads/2016/01/RHK_Seminar_Osnabrueck2016.pdf, retrieved on October 2017

[49] C. Barth, A. S. Foster, M. Reichling, A. L. Shluger: Contrast formation in atomic resolution scanning force microscopy on CaF2(111): experiment and theory.
Journal of Physics-Condensed Matter **13**, 2061 (2001)

[50] C. Barth, O. H. Pakarinen, A. S. Foster, C. R. Henry: Imaging nanoclusters in the constant height mode of the dynamic SFM.
Nanotechnology **17**, 128 (2006)

[51] M. Temmen, J. Lübbe, M. Reichling: NC-AFM Amplitude Calibration with RHK R9 and a MATLAB Script.
RHKTechnology Application Note (RHK Technology, Inc) (2015)

[52] J. Lübbe, M. Temmen, S. Rode, P. Rahe, A. Kühnle, M. Reichling: Thermal noise limit for ultra-high vacuum noncontact atomic force microscopy.
Beilstein Journal of Nanotechnology **4**, 32 (2013)

[53] G. H. Simon, M. Heyde, H.-P. Rust: Recipes for cantilever parameter determination in dynamic force spectroscopy: spring constant and amplitude.
Nanotechnology **18**, 255503 (2007)

[54] M. Temmen: Abbildung von Graphen und CaF_2 (111) mittels hochauflösender Nicht-Kontakt-Rasterkraftmikroskopie, Universität Osnabrück, Diss., 2016

[55] E. Meyer, H. J. Hug, R. Lüthi, B. Stiefel, H.-J. Güntherodt: Forces in scanning probe microscopy. 1998, 23

[56] H.-J. Butt, B. Cappella, M. Kappl: Force measurements with the atomic force microscope: Technique, interpretation and applications.
Surface Science Reports **59**, 1 (2005)

[57] J. N. Israelachvili: Intermolecular and Surface Forces. second. London, UK : Academic Press, 1992. – 450 S.

[58] F. London: The general theory of molecular forces.
Transactions of Faraday Society **332**, 8 (1936)

[59] P. J. W. Debye, P. J. W. Debye: Polar molecules. Bd. 172. Dover New York, 1929

[60] W. Keesom: The second viral coefficient for rigid spherical molecules, whose mutual attraction is equivalent to that of a quadruplet placed at their centre.
KNAW, Proceedings **18**, 636 (1915)

[61] L. Bergström: Hamaker constants of inorganic materials.
Advances in Colloid and Interface Science **70**, 125 (1997). ISBN 0001–8686

[62] S. Sadewasser, T. Glatzel: Kelvin Probe Force Microscopy Measuring and Compensating Electrostatic Forces. Springer Series in Surface Sciences, 2012

[63] M. Nonnenmacher, M. P. O'Boyle, H. K. Wickramasinghe: Kelvin probe force microscopy.
Applied Physics Letters **58**, 2921 (1991)

[64] L. Kelvin: Contact electricity of metals.
Philosophical Magazine **46**, 82 (1898)

[65] H.-H. Pieper: Morphology and electric potential of pristine and gold covered surfaces with the flourite structure, Universität Osnabrück, Diss., 2012

[66] B. D. Terris, J. E. Stern, D. Rugar, H. J. Mamin: Contact Electrification Using Force Microscopy.
Physical Review Letters **63**, 2669 (1989)

[67] P. Milde, S. Porthun: Kelvin Probe Force Microscopy with the RHK R9.
RHKTechnology Application Note (RHK Technology, Inc.) (2016)

[68] D. Neučas, P. Klapetek: Gwyddion: an open-source software for SPM data analysis.
Central European Journal of Physics **10**, 181 (2012)

[69] I. Horcas, R. Fernández, J. M. Gómez-Rodriguez, J. Colchero, J. Gómez-Herrero, A. M. Baro: WSXM: a software for scanning probe microscopy and a tool for nanotechnology.
Review of Scientific Instruments **78**, 13705 (2007)

[70] Gwyddion Documentation. http://gwyddion.net, 2017

[71] C. Barth: Atomar aufgelöste Kraftmikroskopie auf ionischen Oberflächen: Fluoride, Calcit und Saphir, Ludwig-Maximilians-Universität München, Diss., 2001

[72] S. Gritschneder: Untersuchung von Strukturen undchemischen Reaktionen auf Oxidoberflächen mit dem dynamischen Rasterkraftmikroskop, Universität Osnabrück, Diss., 2007

[73] S. Torbrügge: Structure and reactivity of the oxidesurfaces CeO_2(111) and ZnO(0001)studied by dynamic scanningforce microscopy, Universität Osnabrück, Diss., 2008

[74] H. H. Pieper, C. Lammers, L. Tröger, S. Bahr, M. Reichling: Versatile system for the temperature-controlled preparation of oxide crystal surfaces.
Review of Scientific Instruments **83**, 55110 (2012)

[75] L. Howald, E. Meyer, R. Lüthi, H. Haefke, R. Overney, H. Rudin, H. J. Güntherodt: Multifunctional probe microscope for facile operation in ultrahigh vacuum.
Applied Physics Letters **63**, 117 (1993)

[76] S. Torbrügge, J. Lübbe, L. Tröger, M. Cranney, T. Eguchi, Y. Hasegawa, M. Reichling: Improvement of a dynamic scanning force microscope for highest resolution imaging in ultrahigh vacuum.
Review of Scientific Instruments **79**, 83701 (2008)

[77] HAMAMATSU PHOTONICS K.K. :Si PIN photodiode S5980, S5981, S5870 Multi-element photodiodes for surface mounting.
Datasheed https://www.hamamatsu.com/resources/pdf/ssd/s5980_etc_kpin1012e.pdf retrieved on 02.2017

[78] J. L. Hutter, J. Bechhoefer: Calibration of atomic-force microscope tips.
Review of Scientific Instruments **64**, 1868 (1993)

[79] J. Lübbe, M. Temmen, P. Rahe, A. Kühnle, M. Reichling: Determining cantilever stiffness from thermal noise.
Beilstein Journal of Nanotechnology **4**, 227 (2013)

[80] L. Gerward, J. S. Olsen, L. Petit, G. Vaitheeswaran, V. Kanchana, A. Svane: Bulk modulus of CeO_2 and PrO2 - An experimental and theoretical study.
Journal of Alloys and Compounds **400**, 56 (2005)

[81] P. W. Tasker: Stability of Ionic-Crystal Surfaces.
Journal of Physics C: Solid State Physics **12**, 4977 (1979)

[82] J. Jupille, G. Thornton: Defects at Oxide Surfaces. Springer, 2015

[83] S. Torbrügge, M. Cranney, M. Reichling: Morphology of step structures on CeO_2(111).
Applied Physics Letters **93**, 73112 (2008)

[84] H. H. Pieper, C. Barth, M. Reichling: Characterization of atomic step structures on CaF_2(111) by their electric potential.
Applied Physics Letters **101**, 51601 (2012)

[85] S. M. Kozlov, F. Viñes, N. Nilius, S. Shaikhutdinov, K. M. Neyman: Absolute Surface Step Energies: Accurate Theoretical Methods Applied to Ceria Nanoislands.
Journal of Physical Chemistry Letters **3**, 1956 (2012)

[86] T. Duchoň, F. Dvořák, M. Aulická, V. Stetsovych, M. Vorokhta, D. Mazur, K. Veltruská, T. Skála, J. Mysliveček, I. Matolínovaá, V. Matolín: Ordered Phases of Reduced Ceria As Epitaxial Films on Cu(111).
Journal of Physical Chemistry C **118**, 357 (2014)

[87] J. Höcker, T. O. Mentes, A. Sala, A. Locatelli, T. Schmidt, J. Falta, S. D. Senanayake, J. I. Flege: Unraveling the Dynamic Nanoscale Reducibility (Ce^{4+} -> Ce^{3+}) of CeO_X-Ru in Hydrogen Activation.
Advanced Materials Interfaces **2**, 1500314 (2015)

[88] E. A. Kümmerle, G. Heger: The structures of C-Ce_2O_3+d, Ce_7O_{12}, and $Ce_{11}O_{20}$.
Journal of Solid State Chemistry **147**, 485 (1999)

[89] M. Zinkevich, D. Djurovic, F. Aldinger: Thermodynamic modelling of the cerium-oxygen system.
Solid State Ionics, Diffusion & Reactions **177**, 989 (2006)

[90] V. Perrichon, A. Laachir, G. Bergeret, R. Frety, L. Tournayan, O. Touret: Reduction of Cerias with Different Textures by Hydrogen and Their Reoxidation by Oxygen.
Journal of the Chemical Society-Faraday Transactions **90**, 773 (1994)

[91] B. Eck, R. Dronskowski: Atomistic simulations of solid-state materials based on crystal-chemical potential concepts: basic ideas and implementation.
Journal of Alloys and Compounds **338**, 136 (2002)

[92] J. L. F. Da Silva: Stability of the Ce2O3 phases: A DFT+U investigation.
Physical Review B **76**, 4 (2007)

[93] H. Wilkens, O. Schuckmann, R. Oelke, S. Gevers, M. Reichling, A. Schaefer, M. Bäumer, M. H. Zoellner, G. Niu, T. Schroeder, J. Wollschläger: Structural transitions of epitaxial ceria films on Si(111).
Physical Chemistry Chemical Physics **15**, 18589 (2013)

[94] H. Wilkens, O. Schuckmann, R. Oelke, S. Gevers, A. Schaefer, M. Bäumer, M. H. Zoellner, T. Schroeder, J. Wollschläger: Stabilization of the ceria iota-phase (Ce_7O_{12}) surface on Si(111).
Applied Physics Letters **102**, 111602 (2013)

[95] J. Mysliveček, V. Matolín, I. Matolínová: Heteroepitaxy of Cerium Oxide Thin Films on Cu(111).
Materials **8**, 6346 (2015)

[96] T. Duchoň, F. Dvořák, M. Aulická, V. Stetsovych, M. Vorokhta, D. Mazur, K. Veltruská, T. Skála, J. Mysliveček, I. Matolínová, V. Matolín: Comment on "Ordered Phases of Reduced Ceria as Epitaxial Films on Cu(111)".
Journal of Physical Chemistry C **118**, 5058 (2014)

[97] P. Luches, S. Valeri: Structure, Morphology and Reducibility of Epitaxial Cerium Oxide Ultrathin Films and Nanostructures.
Materials **8**, 5818 (2015)

[98] P. Luches, F. Pagliuca, S. Valeri: Structural and morphological modifications of thermally reduced cerium oxide ultrathin epitaxial films on Pt(111).
Physical Chemistry Chemical Physics **16**, 18848 (2014)

[99] T. Hasegawa, S. M. F. Shahed, Y. Sainoo, A. Beniya, N. Isomura, Y. Watanabe, T. Komeda: Epitaxial growth of CeO_2(111) film on Ru(0001): Scanning tunneling microscopy (STM) and x-ray photoemission spectroscopy (XPS) study.
J. Chem. Phys **140**, 044711 (2014)

[100] E. I. Altman, M. Z. Baykara, U. D. Schwarz: Noncontact Atomic Force Microscopy: An Emerging Tool for Fundamental Catalysis Research.
Accounts of chemical research **48**, 2640 (2015)

[101] H. Nörenberg, G. A. D. Briggs: Defect structure of nonstoichiometric CeO_2(111) surfaces studied by scanning tunneling microscopy.
Physical Review Letters **79**, 4222 (1997)

[102] H. Nörenberg, G. A. D. Briggs: Defect formation on CeO_2(111) surfaces after annealing studied by STM.
Surface Science **424**, L352 (1999)

[103] H. Nörenberg: Scanning tunnelling microscopy investigations of nanostructures on single crystalline TiO_2 and CeO_2.
Materials Science and Technology **18**, 755 (2002)

[104] S. Gritschneder, Y. Namai, Y. Iwasawa, M. Reichling: Structural features of CeO_2(111) revealed by dynamic SFM.
Nanotechnology **16**, S41 (2005)

[105] S. Gritschneder, M. Reichling: Structural elements of CeO_2(111) surfaces.
Nanotechnology **18**, 44024 (2007)

[106] F. Esch, S. Fabris, L. Zhou, T. Montini, C. Africh, P. Fornasiero, G. Comelli, R. Rosei: Electron Localization Determines Defect Formation on Ceria Substrates.
Science (Washington, DC, United States) **309**, 752 (2005)

[107] D. C. Grinter, R. Ithnin, C. L. Pang, G. Thornton: Defect structure of ultrathin ceria films on Pt(111): Atomic views from scanning tunnelling microscopy.
Journal of Physical Chemistry C **114**, 17036 (2010)

[108] H. H. Pieper, C. Derks, M. H. Zoellner, R. Olbrich, L. Tröger, T. Schroeder, M. Neumann, M. Reichling: Morphology and nanostructure of CeO_2(111) surfaces of single crystals and Si(111) supported ceria films.
Physical Chemistry Chemical Physics **14**, 15361 (2012)

[109] J. Kullgren, M. J. Wolf, C. W. M. Castleton, P. Mitev, W. J. Briels, K. Hermansson: Oxygen Vacancies versus Fluorine at CeO_2(111): A Case of Mistaken Identity?
Physical Review Letters **112**, 156102 (2014)

[110] S. Torbrügge, M. Reichling, A. Ishiyama, S. Morita, O. Custance: Evidence of Subsurface Oxygen Vacancy Ordering on Reduced CeO_2(111).
Physical Review Letters **99**, 56101 (2007)

[111] X.-P. Wu, X.-Q. Gong: Clustering of Oxygen Vacancies at CeO_2(111): Critical Role of Hydroxyls.
Physical Review Letters **116**, 86102 (2016)

[112] M. B. Watkins, A. S. Foster, A. L. Shluger: Hydrogen Cycle on CeO_2 (111) Surfaces: Density Functional Theory Calculations.
J. Phys. Chem. C **111**, 15337 (2007)

[113] M. Fronzi, S. Piccinin, B. Delley, E. Traversa, C. Stampfl: Water adsorption on the stoichiometric and reduced CeO_2(111) surface: a first-principles investigation.
Physical Chemistry Chemical Physics **11**, 9188 (2009)

[114] D. R. Mullins, P. M. Albrecht, T.-L. Chen, F. C. Calaza, M. D. Biegalski, H. M. Christen, S. H. Overbury: Water Dissociation on CeO_2 (100) and CeO_2 (111) Thin Films.
J. Phys. Chem. C **116**, 19419 (2012)

[115] D. Fernández-Torre, K. Kośmider, J. Carrasco, M. V. Ganduglia-Pirovano, R. Pérez: Insight into the Adsorption of Water on the Clean CeO_2(111) Surface with van der Waals and Hybrid Density Functionals.
Journal of Physical Chemistry C **116**, 13584 (2012)

[116] Y. G. Wang, D. H. Mei, J. Li, R. Rousseau: DFT+U Study on the Localized Electronic States and Their Potential Role During H2O Dissociation and CO Oxidation Processes on CeO_2(111) Surface.
Journal of Physical Chemistry C **117**, 23082 (2013)

[117] D. Fernández-Torre, J. Carrasco, M. V. Ganduglia-Pirovano, R. Pérez: Hydrogen activation, diffusion, and clustering on CeO_2(111): A DFT+U study.
Journal of Chemical Physics **141**, 14703 (2014)

[118] T. Kropp, J. Paier: Reactions of Methanol with Pristine and Defective Ceria (111) Surfaces: A Comparison of Density Functionals.
Journal of Physical Chemistry C **118**, 23690 (2014)

[119] S. Torbrügge: Structure and reactivity of the oxide surfaces CeO_2 (111) and ZnO(0001) studied by dynamic scanning force microscopy at various temperatures , Universität Osnabrück, Diss., 2008

[120] M. H. Zoellner, J. Dabrowski, P. Zaumseil, A. Giussani, M. A. Schubert, G. Lupina, H. Wilkens, J. Wollschläger, M. Reichling, M. Bäumer, T. Schroeder: Stacking behavior of twin-free type-B oriented CeO_2(111) films on hexagonal Pr_2O_3(0001)/Si(111) systems.
Physical Review B **85**, 35302 (2012)

[121] M. S. Paun: Single Crystal Growth of High Melting Oxide Materials by Means of Induction Skull-Melting, Technische Universität Berlin, Diss., 2015

[122] S. Sadewasser, P. Jelinek, C. K. Fang, O. Custance, Y. Yamada, Y. Sugimoto, M. Abe, S. Morita: New Insights on Atomic-Resolution Frequency-Modulation Kelvin-Probe Force-Microscopy Imaging of Semiconductors.
Physical Review Letters **103**, 266103 (2009)

[123] A. Foster, A. Shluger, C. Barth, M. Reichling: Contrast mechanisms on insulating surfaces. In: Morita, S, (Hrsg.) , Wiesendanger, R, (Hrsg.) , Meyer, E, (Hrsg.): *Noncontact Atomic Force Microscopy*. Berlin : Springer, 2002, 305

[124] C. Barth, T. Hynninen, M. Bieletzki, C. R. Henry, A. S. Foster, F. Esch, U. Heiz: AFM tip characterization by Kelvin probe force microscopy.
New Journal of Physics **12**, 93024 (2010)

[125] J. P. Holgado, R. Alvarez, G. Munuera: Study of CeO_2 XPS spectra by factor analysis: reduction of CeO_2.
Applied Surface Science **161**, 301 (2000)

[126] S. Gritschneder, M. Reichling: Atomic Resolution Imaging on CeO_2(111) with Hydroxylated Probes.
Journal of Physical Chemistry C **112**, 2045 (2008)

[127] S. Gritschneder, Y. Iwasawa, M. Reichling: Strong adhesion of water to CeO_2(111).
Nanotechnology **18**, 44025 (2007)

[128] S. Torbrügge, O. Custance, S. Morita, M. Reichling: Manipulation of individual water molecules on CeO_2(111).
Journal of Physics: Condensed Matter **24**, 84010 (2012)

[129] G. E. Murgida, M. V. Ganduglia-Pirovano: Evidence for subsurface ordering of oxygen vacancies on the reduced CeO_2(111) surface using density-functional and statistical calculations.
Physical Review Letters **110**, 246101 (2013)

[130] S. Gritschneder, S. Degen, C. Becker, K. Wandelt, M. Reichling: Atomic structure of a stripe phase on Al2O3/Ni3Al(111) revealed by scanning force microscopy.
Physical Review B **76**, 14123 (2007)

[131] F. Dvořák, M. F. Camellone, A. Tovt, N. D. Tran, F. R. Negreiros, M. Vorokhta, T. Skála, I. Matolínová, J. Mysliveček, V. Matolín, S. Fabris: Creating single-atom Pt-ceria catalysts by surface step decoration.
Nature Communications **7**, 10801 (2016)

Danksagung

An dieser stelle bedanke ich mich bei allen, die mich bei der dieser Arbeit unterstützt haben. Besonderer Dank gilt:

Prof. Dr. Michael Reichling für die Betreuung und Möglichkeit in seiner Arbeitsgruppe diese Dissertation anzufertigen und für die vielen wertvollen Diskussionen.

Dr. Clemens Barth, für die Unterstützung als Zweitgutachter, sowie die erfolgreiche Zusammenarbeit und vielen wertvollen Diskussionen.

Dr. M. Verónica Ganduglia-Pirovano und **Dr. Gustavo E. Murgida** für die erfolgreiche Zusammenarbeit und vielen wertvollen Diskussionen.

Allen beteiligten Authoren bei den Journal Veröffentlichungen.

Prof. Dr. Jochen Gemmer und **Dr. Rainer Pankrath** für ihre Zustimmung zur Teilnahme an der Promotionskommission.

Der gesamten **Arbeitsgruppe** für das nette Arbeitsklima und insbesondere **Dr. M. Temmen** für die Unterstützung bei der Inbetriebnahme der RHK Steuerelektroniken mit dem Omicron AFM und **Dr. J. Lübbe** für die Unterstützung beim Einbau der neuen Glasfaser und dem Tausch der Fotodiode im Omicron AFM.

6.1 Appendix

6.1.1 Journal publications

1 **Olbrich R**, Pieper HH, Oelke R, Wilkens H, Wollschläger J, Zoellner MH, Schroeder T, Reichling M , *A well-structured metastable ceria surface*, Applied Physics Letters 104:081910, (2014).

2 **Olbrich, R.**; Murgida, G. E.; Ferrari, V.; Barth, C.; Llois, A. M.; Reichling, M.; Ganduglia-Pirovano, M. V., *Surface Stabilises Ceria In Unexpected Stoichiometry*, The Journal of Physical Chemistry C 121:6844-6851, (2017).

3 Barth C, Laffon C, **Olbrich R**, Ranguis A, Parent P, Reichling M , *A perfectly stoichiometric and flat $CeO_2(111)$ surface on a bulk-like ceria film*, Scientific Reports 6:21165, (2016).

4 Niu G, Zoellner MH, Schroeder T, Schaefer A, Jhang JH, Zielasek V, Bäumer M, Wilkens H, Wollschläger J, **Olbrich R**, Lammers C, Reichling M , *Controlling the physics and chemistry of binary and ternary praseodymium and cerium oxide systems*, Physical Chemistry Chemical Physics 17 (38):24513-24540, (2015).

5 Pieper HH, Derks C, Zoellner MH, **Olbrich R**, Tröger L, Schroeder T, Neumann M, Reichling M (2012), *Morphology and nanostructure of $CeO_2(111)$ surfaces of single crystals and Si(111) supported ceria films*, Physical Chemistry Chemical Physics 14 (44):15361-15368, (2012).

6.1.2 Conferences presentations

DPG-Frühjahrstagung der Sektion Kondensierte Materie (SKM); Berlin Germany 2012: talk

Cost Action CM1104 Reducible oxides chemistry, structure and functions; Modena Italy 2013: talk

Cost Action CM1104 Joint WG1 + WG3 Meeting, Vienna Austria 2013: poster

1^{st} German-French Summer School on noncontact AFM; Porquerolles France 2013: poster

Cost Action CM1104 WG1+WG2 Meeting ; Osnabrück Germany 2015: attendance

Workshop on Ceria- based Materials in Catalysis and Electrochemistry (MCE), Schloss Rauischholzhausen Germany 2015: talk

Cost Action CM1104 Reducible oxides chemistry, structure and functions 4^{th} and Final General meeting Osnabrück Germany 2016: poster

2^{nd} German-French Summer School on noncontact AFM; Osnabrück Germany 2016: attendance

33rd European Conference on Surface Science (ECOSS-33); Szeged Hungary 2017: talk + poster

Erklärung über die Eigenständigkeit der erbrachten wissenschaftlichen Leistung

Ich erkläre hiermit, dass ich die vorliegende Arbeit ohne unzulässige Hilfe Dritter und ohne Benutzung anderer als der angegebenen Hilfsmittel angefertigt habe. Die aus anderen Quellen direkt oder indirekt übernommenen Daten und Konzepte sind unter Angabe der Quelle gekennzeichnet

Bei der Auswahl und Auswertung folgenden Materials haben mir die nachstehend aufgeführten Personen in der jeweils beschriebenen Weise unentgeltlich geholfen.

1. H. Wilkens and J. Wollschläger contributed the LEED measurements in chapter 5.2.4.

2. Dr. Clemens Barth, A. Ranguis , Ph. Parent, C. Laffon contributed the NC-AFM and XPS measurements in chapter 5.2.2.

3. Dr. H.H. Pieper and Dr. S. Torbrügge contribute the NC-AFM measurements on the ceria crystal in chapter 5.2.3

4. M. Verónica Ganduglia-Pirovano, Gustavo E.Murgida, Valeria Ferrari, Ana M. Llois contributed the DFT-calculations for reduced ceria surface phases in chapter 5.2.1.

Weitere Personen waren an der inhaltlichen materiellen Erstellung der vorliegenden Arbeit nicht beteiligt. Insbesondere habe ich hierfür nicht die entgeltliche Hilfe von Vermittlungs- bzw. Beratungsdiensten (Promotionsberater oder andere Personen) in Anspruch genommen. Niemand hat von mir unmittelbar oder mittelbar geldwerte Leistungen für Arbeiten erhalten, die im Zusammenhang mit dem Inhalt der vorgelegten Dissertation stehen. Die Arbeit wurde bisher weder im In- noch im Ausland in gleicher oder ähnlicher Form einer anderen Prüfungsbehörde vorgelegt.

Osnabrück, _____ _____